MICROSTRUCTURAL CHANGES IN ALUMINUM UNDER REVERSING STRAINS

BALAKRISHNAN ANANDAPADMANABAN

A Thesis in

The Department of Mechanical and Industrial Engineering

Presented in Partial Fulfillment of Requirements
For the Degree of Master of Applied Science (Mechanical Engineering) at
Concordia University
Montreal, Quebec, Canada.

April, 2007

Library and
Archives Canada

Published Heritage
Branch

395 Wellington Street
Ottawa ON K1A 0N4
Canada

Bibliothèque et
Archives Canada

Direction du
Patrimoine de l'édition

395, rue Wellington
Ottawa ON K1A 0N4
Canada

Your file Votre référence
ISBN: 978-0-494-34613-6
Our file Notre référence
ISBN: 978-0-494-34613-6

NOTICE:
The author has granted a non-exclusive license allowing Library and Archives Canada to reproduce, publish, archive, preserve, conserve, communicate to the public by telecommunication or on the Internet, loan, distribute and sell theses worldwide, for commercial or non-commercial purposes, in microform, paper, electronic and/or any other formats.

The author retains copyright ownership and moral rights in this thesis. Neither the thesis nor substantial extracts from it may be printed or otherwise reproduced without the author's permission.

AVIS:
L'auteur a accordé une licence non exclusive permettant à la Bibliothèque et Archives Canada de reproduire, publier, archiver, sauvegarder, conserver, transmettre au public par télécommunication ou par l'Internet, prêter, distribuer et vendre des thèses partout dans le monde, à des fins commerciales ou autres, sur support microforme, papier, électronique et/ou autres formats.

L'auteur conserve la propriété du droit d'auteur et des droits moraux qui protège cette thèse. Ni la thèse ni des extraits substantiels de celle-ci ne doivent être imprimés ou autrement reproduits sans son autorisation.

In compliance with the Canadian Privacy Act some supporting forms may have been removed from this thesis.

While these forms may be included in the document page count, their removal does not represent any loss of content from the thesis.

Conformément à la loi canadienne sur la protection de la vie privée, quelques formulaires secondaires ont été enlevés de cette thèse.

Bien que ces formulaires aient inclus dans la pagination, il n'y aura aucun contenu manquant.

Canada

ABSTRACT

MicroStructural Changes in Aluminum under Reversing Strains

Balakrishnan Anandapadmanaban

99.9 Aluminum- hot worked at 400°C-500°C and strain rates ($\dot{\varepsilon}$) of 0.004-0.1s^{-1}, under reversing strains (ε) of 0.5 to 0.2 or 0.5 to 0 and also advancing from 0.5 to 1 or 0.5 to 5. Under similar test conditions for different parts of the strain paths, the average measured flow stresses are found to agree with each other. In the forward and backward strain path tests, the almost identical steady state plateaus affirm the occurrence of dynamic recovery (DRV). On reversal of strain direction at constant $\dot{\varepsilon}$, there was generally neglible Bauschinger effect. Features such as elongated grains with serrations and deformation bands confirmed DRV in forward path specimens by optical microscopy. In reverse path specimens, equiaxed grains were seen. In forward path specimens by low magnification polarized optical microscopy, grain alignment increased with strain whereas it decreased in reverse path specimens. Orientation imaging microscopy revealed during the forward path, elongated grains are broken up as deformation bands rotate and on backward straining grains return to equiaxed appearance. The subgrains remain equiaxed and constant in size and character during the forward and backward paths. During forward straining, the fraction of high angle boundaries increased with respect to low angle boundaries and with backward straining it was vice versa. In as-worked specimens annealed at 400°C, static recrystallisation (SRX) was confirmed by microstructual evidence such as fine recrystallized grains in forward path specimens. The progress of

SRX in many specimens was seen as a mixture of recrystallized grains and grains with serrated boundaries.

ACKNOWLEDGEMENTS

I would like personally express my gratitude and appreciation to my supervisor Prof H J McQueen for his invaluable guidance, support, patience and encouragement throughout this research project.

Special words of appreciation would go to Dr E V Konopleva for her advice on metallographic sample preparation and etching. In addition, I am grateful to Dr Avramovic Cingara who willingly gave POM and OIM micrographs. I also thank Concordia and McGill who made the technical equipment available needed for this work. I also acknowledge for the financial support rendered by the Natural sciences and engineering council of Canada during the course of this project.

Finally I wish to thank my grand parents, parents and my sister for all their inspiration and encouragement.

TABLE OF CONTENTS

Page

LIST OF FIGURES x

LIST OF TABLES xv

LIST OF SYMBOLS xvi

CHAPTER ONE 1

INTRODUCTION 1

CHAPTER TWO 4

REVIEW OF PAST WORK 4

2-1. Restoration Mechanisms 4

2-2. Dynamic Recovery 4

2-3. Bauschinger Effect 9

2-4. Hall-Petch Equation and Product Properties 11

2-5. Constitutive Equations 13

2-6) Effect of DRV and Hot Ductility 14

2-7. Hot Ductility on Low SFE Metals 19

2-8. Cold Working 23

2-9. Utility of Annealing 28

2-10. Static Restorations after Cold Working 31

2-11. Static Restorations after Hot Working 35

2-12. Grain Growth 42

CHAPTER THREE **44**

EXPERIMENTAL PROCEDURE AND ANALYSIS OF DATA 44

3-1. Introduction 44

3-2. Test Material 45

3-3. Heat Treatment, Thermal Cycles and Testing Procedure 47

3-4. Torsion Machine 48

3-5. Stress and Strain Conversion 53

3-6. Microscopic Examination 55

CHAPTER FOUR **56**

EXPERIMENTAL RESULTS 56

Overview 56

4-1. ANALYSIS OF FLOW CURVES WITH METALLOGRAPHY 60

4-1.1. Group I 60

4-1.2. Group II 66

4-1.3. Group III 71

4-1.4. Group IV 75

4-1.5. Group V 78

4-2. ORIENTATION IMAGING AND POLARIZED OPTICAL MICROSOPY 84

4-3. EXAMINATION OF ANNEALED SPECIMENS 98

4-3.1. Optical Micrographs of Annealed specimens 98

CHAPTER FIVE **114**

DISCUSSION 114

CHAPTER SIX **119**

CONCLUSION 119

REFERENCES **121**

LIST OF FIGURES

Figure 1: Flow curves of Al compressed at 45, 8.1 and $2.7s^{-1}$ [1,14]. 7

Figure 2: Hot Worked Substructures of Al compressed to strain of 0.7, 400°C, $0.1s^{-1}$ observed by Transmission electron microscopy [1]. 8

Figure 3: Bauschinger effect [5]. 10

Figure 4: Dependence of room temperature yield stress of Al on subgrain sizes [1, 9-14]. 12

Figure 5: Torsional ductility of 99.99% Al with temperatures 16

Figure 6: Torsional Ductilities of Al and Al-Mg alloys at 0.0013, 0.1, 1 and $10s^{-1}$ [23]. 17

Figure 7: Comparison of ductilities in tension between Al and Al-Mg alloys [23, 24]. 18

Figure 8: Cracks occurred in Waspaloy a) 25°C, $1s^{-1}$ to $\varepsilon = 0.6$ b) 954°C, $1s^{-1}$ to $\varepsilon = 1$[24]. 21

Figure 9: Flow curves of 0.14% C-Steel at 1 and $1x10^{-1}s^{-1}$ [24]. 21

Figure 10: Torsional ductilites of Al alloys, Fe-25%Cr and Ni alloys [20, 30]. 22

Figure 11: Stress-Strain response in single crystals [40]. 25

Figure 12: Dislocation density of cold worked metal [31]. 26

Figure 13: Substructure of 50% C.W Al at $1.4s^{-1}$, 20°C [2]. 26

Figure 14: Mechanical properties of metal or alloy up to 50% C.W [34]. 27

Figure 15: Effect of annealing on cold worked metal [34, 42]. 30

Figure 16: 50% Cold worked Al-0.8Mg annealed at a) 302°C b) 316°C [34]. 31

Figure 17: Recrystallization rates of Al under various annealing times and temperatures[34,43] 32

Figure 18: Effect of annealing temperature on yield strength of Al [31]. 33

Figure 19: Plot showing earlier drop in hardness values for greater % C.W [31]............ 33

Figure 20: Drop in Hardness values and increase in subgrain size with increase in annealing temperature and time for 80% C.W Al crystal [2]. 34

Figure 21: Stress Strain Curves at moderate temperatures for Al 99.9997 and Al-0.5Mg at $0.41s^{-1}$ unloaded for intervals of 30 to 15s [51]. 38

Figure 22: Micrographs of Al 99.997 exhibiting deformed grains ($\varepsilon = 2.45$) 450°C,2.2s $X_R = 0.95$ [51]...38

Figure 23: Micrographs of Al-0.5Mg exhibiting (deformed grains ($\varepsilon = 2.45$) 450°C, 16s $X_R = 0.95$ [51]...39

Figure 24: Micrographs of Al-0.96Mg exhibiting (deformed grains ($\varepsilon = 2.45$) 450°C, 15s $X_R = 0.95$ [51]... 40

Figure 25: Relation between subgrain size and steady state flow stress for Al and Al-Mg alloys [51] 41

Figure 26: Relation between grain boundary area and hardness of Brass [31]. 43

Figure 27: Grain Growth of Brass at 700°C in 10 min [31].. 43

Figure 28: Test specimen geometry [2]. 46

Figure 29: Layout of Hot torsion machine [61]. 50

Figure 30: Strain control and measurement subsystem [61]... 50

Figure 31: Torque Cell Assembly [61]. 51

Figure 32: Diagram of Radiant Furnace [61]. 51

Figure 33: Schematic Diagram of test Specimens [61]. 52

Figure 34: Flow curves of Al at 400°C, $0.1s^{-1}$ up to strains of 0.2, 0.5, 1 and 5.............. 61

Figure 35: Optical micrographs of as-worked specimen 1 at 400-0.1-0.2 with deformation bands (Flow curve, Fig 34). 62

Figure 36: Optical micrographs of as-worked specimen 2 at 400-0.1-0.5 (Flow curve, Fig 34) 63

Figure 37: Optical micrographs of as-worked specimen 5 at 400-0.1-0.5-400-0.1-1 (Flow curve, Fig 34) 64

Figure 38: Optical micrographs of as-worked specimen 6 at 400-0.1-0.5-400-0.1-5 with deformation bands and serrated boundaries (Flow curve, Fig 34) 65

Figure 39 : Flow curve of Al at 400 - 0.1 - 0.5 - 400 - 0.1 - 0.2. 67

Figure 40: Flow curve of Al at 400 - 0.1 - 0.5 - 400 - 0.1 – 0. 68

Figure 41: Optical micrographs of as-worked specimen 3 at 400-0.1-0.5-400-0.1-0.2 (Flow curve, Fig 39). 69

Figure 42: Optical micrographs of as-worked specimen 4 at 400-0.1-0.5-400-0.1-0 with serrated grain boundaries (Flow curve, Fig 40). 70

Figure 43: Flow curves of Al deformed at 400-0.1-0.5-400-0.004-1. 72

Figure 44: Flow curve of Al deformed at 400 – 0.1 – 0.5 - 400 – 0.004 - 0.2 73

Figure 45: Flow curve of Al deformed at 400 - 0.1 - 0.5 - 400 - 0.004 – 0. 74

Figure 46: Flow curves of Al under 400 – 0.004 – 0.5. 76

Figure 47: Flow curve of Al under 500 -0.1-0.5. 77

Figure 48: Flow curves of specimens 11, 12 and 13 79

Figure 49: Flow curve of Al deformed at 400-0.1-0.5-500-0.1-0. 80

Figure 50: Flow curves of specimens 7, 9 and 10 82

Figure 51: Flow curves of specimens 7, 10 and 11 83

Figure 52: Polarized optical macrographs of as-worked specimens 1D,2D and 5D in forward path: a) 400-0.1-0.2, b) 400-0.1-0.5 and c)400-0.1-0.5 – 400-0.1-1, same magnification (courtesy of Dr G.A Cingara) (optical micrographs of specimens 1,2..... 86

Figure 53: Polarized optical macrographs of as-worked specimens 3 and 4 in reverse path: a) 400-0.1-0.5 - 400-0.1-0.2 and b) 400-0.1-0.5 – 400-0.1-0, same magnification. 87

Figure 54: Polarized optical micrographs of specimens: a) 1D hot worked at 400-0.1-0.2 b) 2D hot worked at 400-0.1-0.5 88

Figure 55: Polarized optical micrographs of specimen 5D hot worked at 400-0.1-0.5-400-0.1-1 (The microstructure of this specimen is more clearly presented in OIM micrograph Fig 58) (courtesy of Dr G.A Cingara) [62] 89

Figure 56: Polarized optical micrographs of specimens: a) 3D hot worked at 400-0.1-0.5-400-0.1-0.2 b) 4D hot worked at 400-0.1-0.5-400-0.1-0 (macrographs given in Fig 53) (courtesy of Dr G.A Cingara) [62] 90

Figure 57: Orientation imaging microscopy of specimen 2D deformed at 400-0.1-0.5... 93

Figure 58: Orientation imaging microscopy of specimen 5D deformed at 400-0.1-0.5 – 400-0.1-1 a) lower magnification b) higher magnification (Fig 55) (courtesy of Dr G.A Cingara) [62] 94

Figure 59: Orientation imaging microscopy of specimen 6D deformed at 400-0.1-0.5 – 400-0.1-5(courtesy of Dr G.A Cingara) [62]. 95

Figure 60: Orientation imaging microscopy of specimen 3D deformed at 400-0.1-0.5 – 400-0.1-0.2 (Fig 56) (courtesy of Dr G.A Cingara) [62]. 96

Figure 61: Orientation imaging microscopy of specimen 4D deformed at 400-0.1-0.5 – 400-0.1-0 (Fig 56) (courtesy of Dr G.A Cingara) [62]. 97

Figure 62: Optical micrographs of specimen 1 (400-0.1-0.2) annealed for 450s a) higher magnification b) lower magnification (as-worked, Fig 35). 99

Figure 63: Optical micrographs of specimen 1 (400-0.1-0.2) annealed for 600s (as-worked,Fig35) 100

Figure 64: Optical micrographs of specimen 2 (400-0.1-0.5) annealed for 300s a) lower magnification b) higher magnification (as-worked, Fig 36). 101

Figure 65: Optical micrographs of specimen 2 (400-0.1-0.5) annealed for 500s (as-worked, Fig 36) 102

Figure 66: Optical micrograph of specimen 5 (400-0.1-0.5-400-0.1-1) annealed for 125s (as-worked, Fig 37). 105

Figure 67:Optical micrograph of specimen 5 (400-0.1-0.5-400-0.1-1) annealed for 450s (as-worked, Fig 37). 106

Figure 68: Optical micrograph of specimen 6 (400-0.1-0.5-400-0.1-5) annealed for 125s (as-worked, Fig 38) 107

Figure 69: Optical micrograph of specimen 6 (400-0.1-0.5-400-0.1-5) annealed for 450s (as-worked, Fig 38) 108

Figure 70: Optical micrograph of specimen 3 (400-0.1-0.5-400-0.1-0.2) annealed for 250s (as-worked, Fig 41). 109

Figure 71: Optical micrograph of specimen 3 (400-0.1-0.5-400-0.1-0.2) annealed for 450s (as-worked, Fig 41). 110

Figure 72: Optical micrograph of specimen 4 (400-0.1-0.5-400-0.1-0) annealed for 250s (as-worked, Fig 42). 111

Figure 73: Optical micrographs of specimen 4 (400-0.1-0.5-400-0.1-0) annealed for 450s (as-worked, Fig 42). 112

Figure 74: Plot showing annealing times with indication of degree of SRX (Specimens 1, 2, 5 and 6 were strained in forward direction to 0.2, 0.5,1 and 5 respectively. Specimens 3 and 4 were strained backwards from 0.5 to 0.2 and 0) 113

LIST OF TABLES

Table 1: Chemical composition of Al 99.9% 45

Table 2: Test conditions of 99.9%Al samples (Flow stress, σ). 58

Table 3: Measured average plateau stresses for test conditions. 59

Table 4: Calculated flow stresses and logZ values for the given conditions. 59

Table 5: Misorientation statistics for OIM boundaries in % after straining at 400°C, $0.1s^{-1}$ (courtesy of Dr G.A Cingara) [62] 92

LIST OF SYMBOLS

A	experimental constant
$A^{'}$	experimental constant
$A^{''}$	experimental constant
A_o	area of original specimen
A_f	area of final specimen
Al	aluminum
BCC	body centered cubic
BHN	brinells hardness number
BW	block walls
Cr	chromium
CW	cold work
D	grain boundary diffusivity
DRV	dynamic recovery
DRX	dynamic recrystallization
F_n	function
FCC	face centered cubic
FS	fractional softening
G	cavity growth rate
GB	grain boundary
HAB	high angle boundaries
LAB	low angle boundaries
L_o	original length of gauge section (mm)

MB	micro-bands
MAB	medium angle boundaries
MPa	mega pascals
N	no of revolutions in torsion test
Ni	nickel
OIM	orientation imaging microscopy
POM	polarized optical microscopy
Q	activation energy [kJ/mol]
Q_{HW}	activation energy for hot working [kJ/mol]
R	universal gas constant [8.314 J/mol-K]
SiC	silicon carbide
SFE	stacking fault energy
SGB	subgrain boundaries
SRV	static recovery
SRX	static recrystallization
T	temperature (^{o}C)
T_A	annealing temperature
T_H	holding temperature
T_M	melting temperature
TEM	transmission electron microscopy
Ti	titanium
X_R	fraction recrystallised
Z	Zener-Hollomon parameter

a	constant
b	constant
d_s	subgrain size
i	number of stages
k	experimental constant
k_s	coefficient of sub-boundary strength
m	strain rate sensitivity
n	experimental constant
n'	experimental constant
n''	strain hardening exponent
p	constant
r	gauge radius (mm)
r'	cavity radius
t_R	time for complete recrystallization

α	constant
β	bauschinger strain
β'	constant
ε	strain
$\dot{\varepsilon}$	strain rate
ε_{eq}	equivalent strain
τ	torsional surface shear stress
Γ	torsional moment
γ	torsional shear strain
μ	microns
σ_s	flow Stress (MPa)
σ_{eq}	equivalent stress
σ_{mi}	maximum stress in multi stage
σ_o	yield strength of annealed metal
$\sigma_{r\,(i+1)}$	strength on reloading after the interval
σ_s	flow Stress (MPa)
σ_y	original yield strength
θ	misorientation

CHAPTER ONE

INTRODUCTION

Aluminum possesses a unique combination of price, mechanical properties and light weight to serve as fabricated products for aerospace, automobile and general applications. Due to its malleable nature, it can be cast, rolled or extruded into a wide variety of shapes. It is also environmentally friendly as it is recyclable. Its light weight and non reactive nature helps in reducing fuel consumption and preventing corrosion. In the present complex and competitive industrial activity, there has been a need for products with superior properties tailored for specific applications. As 80% of metal manufacturing involves high temperature mechanical working, product and quality improvement is essential for the survival of the metals industry which faces competition from ceramics and plastics [1]. The product quality should be ensured by production of suitable microstructures through a process which is controlled at every step by macroscopic parameters through large machines. Hot working has proved to be effective in providing strengthened and malleable products through microstructural refinement. It also aims in reducing hot strength and raising ductility. Metals are generally hot worked at a range of temperatures ($>0.5T_M$, melting K) and strain rates (10^{-3} to $10^{2}s^{-1}$) to achieve large strains without much strain hardening [1]. This results in: energy decrease for forming, reduction in machine size, minimization of rejects, decreasing chemical inhomogenities of the cast metal and production of suitable microstructure with improved service properties such as high ductility [2]. Hot worked substructures are retained to promote product strengthening in thermomechanical processing through parameters such as holding temperature and cooling time. These properties are usually brought about by microstructural features such as change in dislocation density and subgrain size.

The objective of this research project is to delve into the effects of temperature and strain rate on flow stress and microstructural development of aluminum under reversed strains. The main focus is to study the influence of the Bauschinger effect on the substructure development of aluminum, identify the possible restoration mechanisms and to correlate with other aluminum alloys. The torsion test was suitable for hot workability testing, as working strains of any industrial process can be closely matched. In order to correlate substructural evolution with modeling and processing strategies, there is a need for repeatable and reproducible test data which are provided by torsion tests. Torsion testing was done at temperatures of 400-500°C, strain rates of 0.004-0.1s^{-1} with strain reversing from 0.5 to 0.2 or 0.5 to 0 and advancing 0.5 to1 or 0.5 to 5. The variously as-worked specimens are annealed to detect the occurrence of static recrystallization. The effect of strain path on the restoration mechanism after hot working is investigated through the evolution of the substructure.

A literature review will discuss the variation of flow stress, microstructure and deformation mechanisms with strain rate and temperature. An overview of the testing procedure and analysis will be provided indicating flow curve dependence on various parameters. In a detailed investigation microstructures will be related to the flow curves which could play a role in controlling power requirement and deformation rate. Critical points in flow curves are discussed in association with micrography indicating the progress of restoration mechanism and influence of solutes and precipitates. Future scope of research will be discussed based on the results. A detailed emphasis will be focused on the restoration mechanisms after hot working.

CHAPTER TWO

REVIEW OF PAST WORK

2-1. Restoration Mechanisms

As hot working processing involves single or multiple steps, it is imperative to understand the mechanisms that occur in the worked metal during industrial hot processing. In the hot working domain, restoration mechanisms influence metal behavior. This can be understood by establishing links between deformation parameters, strain hardening behavior and subgrain structure. The restoration which happens during the deformation is called dynamic and that after it is known as static. In high stacking fault energy (SFE) metals like Al, recovery is the principal restoration mechanism resulting in low dislocation density and equiaxed subgrains. In contrast, recrystallization is associated with a high dislocation density in low SFE metals (Cu, Ni) that gives rise to nucleation and growth of new grains.

2-2. Dynamic Recovery

When a metal is strained, countless dislocations are emitted from Frank-Read sources which give rise to strain hardening. In the domain of creep and hot working, Al develops highly polygonized substructures that indicate dynamic recovery (DRV). By comparing the flow curves at 330°C, 410°C and 480°C (Fig 1) under various strain rates of 45, 8.1 and 2.7s^{-1}, it is seen that the rate of strain hardening decreases with temperature rise as DRV counteracts strain hardening [1,2]. At high T and low $\dot{\varepsilon}$, the steady state plateau is established after a strain of 0.5 in most of the curves because of the equilibrium existing between generation and annihilation of dislocations (Fig 1) [1]. The flow stress values observed for $2.7s^{-1}$ at 330, 410 and 480°C were 73, 48 and 35MPa, respectively. This drop in flow stress can be attributed to rise in temperature. As Al is a face centered cubic (FCC) metal with high SFE, the dislocations can easily cross slip and climb. In high SFE metals, entanglement of dislocations happens during strain hardening and as T is increased into the hot working range, there is subgrain formation with low interior dislocation densities. Constant dislocation density and equiaxed subgrains of stable size and low misorientation characterize the steady state as seen in Fig 2 [2]. In the elongating grains, equiaxed subgrains of constant average size are maintained through continuous unraveling and knitting of dislocations at cell walls [3, 4]. With increasing $\dot{\varepsilon}$ to $45s^{-1}$, the observed flow stress values were 55, 75 and 85MPa in the decreasing order of temperature.

The dependence of flow stress on T and $\dot{\varepsilon}$ at the steady state is represented as function (F_n) of the steady state stress (σ_s) (Eqn 1) [2]. The DRV subgrain size (d_s) is related to Z (Zener-Holomon parameter) and σ_s (steady state or flow stress) as follows (Eqn 2, 3). The amount of recovery per unit strain is defined by the control variables T and $\dot{\varepsilon}$: [1]

$$F_n(\sigma_s) = \dot{\varepsilon} \exp(Q/RT) = Z \qquad (1)$$

$$d_s^{-1} = G + H \log Z \qquad (2)$$

$$\sigma_s = a + b\, d_s^{-1} \qquad (3)$$

where a, b, G, H are experimental constants and $Z = \dot{\varepsilon} \exp(-Q/RT)$ [2], Q is activation energy, T is absolute temperature and R is universal gas constant. Under steady state conditions at higher Z, smaller d_s is established at higher σ_s. The retention of hot worked substructures can offer excellent strengthening opportunities. It is observed that a recovered substructure is more ductile, corrosion resistant and more stable for high temperature service than a cold worked metal of equal strength at 20°C [2].

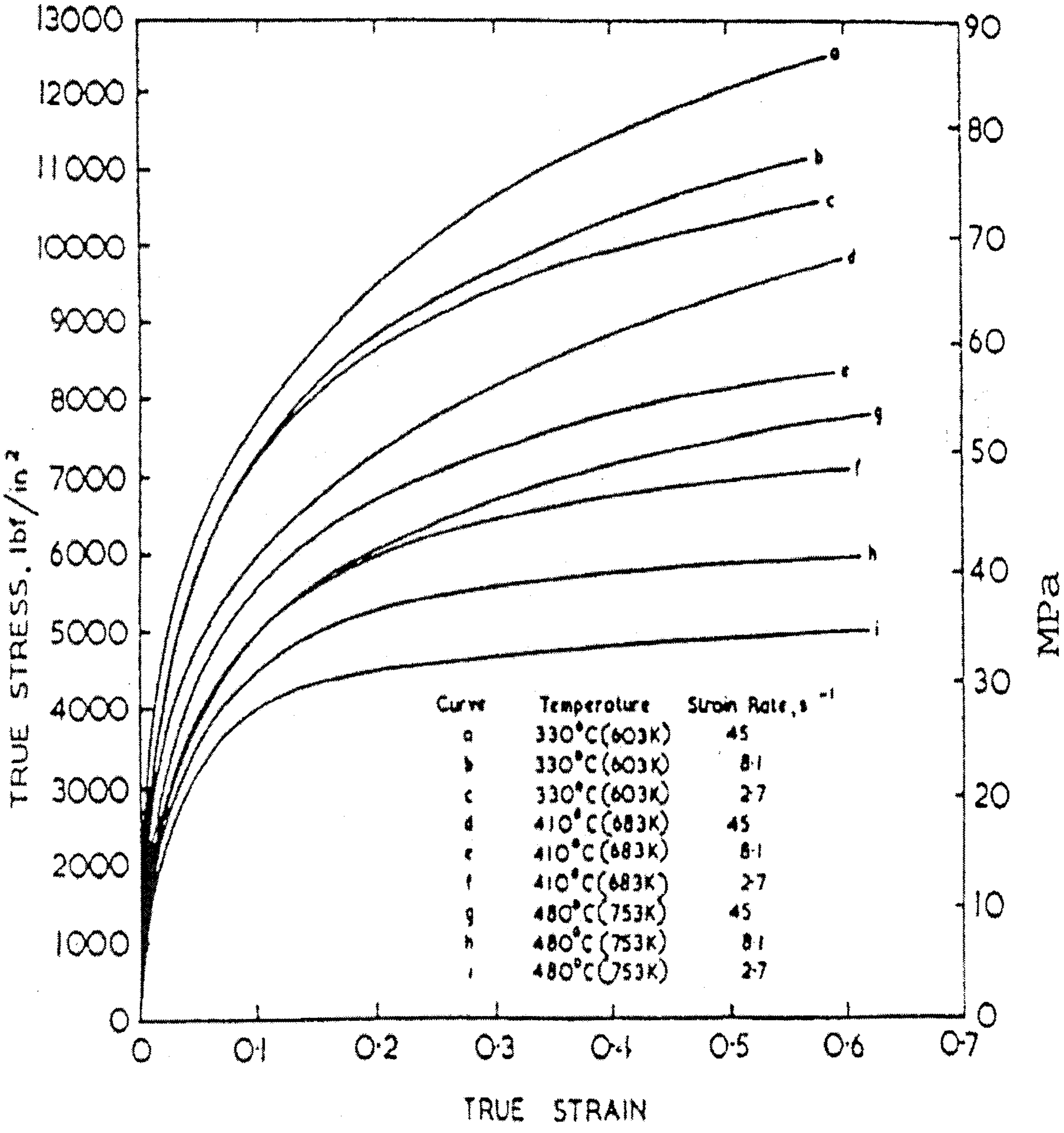

Figure 1: Flow curves of Al compressed at 45, 8.1 and 2.7s^{-1} [1,14].

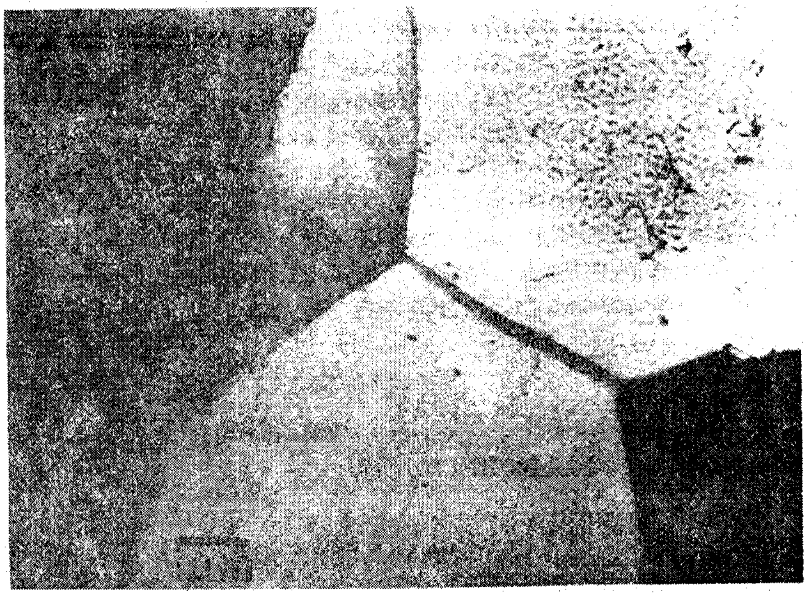

Figure 2: Hot Worked Substructures of Al compressed to strain of 0.7, 400°C, $0.1s^{-1}$ observed by Transmission electron microscopy [1].

2-3. Bauschinger Effect

In industrial cold forming operations, the deformed product may be subjected to stresses that are the opposite of the forming ones; the yield stress may be lower than that expected from strain hardening. Hence, it is important to discuss the influence of Bauschinger effect on hot working operations. From Fig 3, when a metal is tension tested, its initial yield stress is A. If different specimen is tested in compression, its yield strength would have the same value B (=A) on the dashed line. Now when another specimen is loaded in tension, the stress-strain curve follows the path OAC. If the specimen is unloaded the curve will follow CD path; when immediately followed by applying compressive stress, it is concluded that compressive yield stress (E) which would be less than the original yield stress (A or B). The reduction of yield stress on reverse loading is called the Bauschinger Effect. The amount of Bauschinger effect may be expressed by the difference in strain (β) between the tension and compression at a projected service stress [5].

When the metal is deformed plastically, the dislocations start accumulating at barriers and form cells. When the loading is reversed the dislocation lines will move to a small distance at lower shear stress because the resistance to such dislocation motion is not strong. This phenomenon leads to lower yield stress on reversed loading [5].

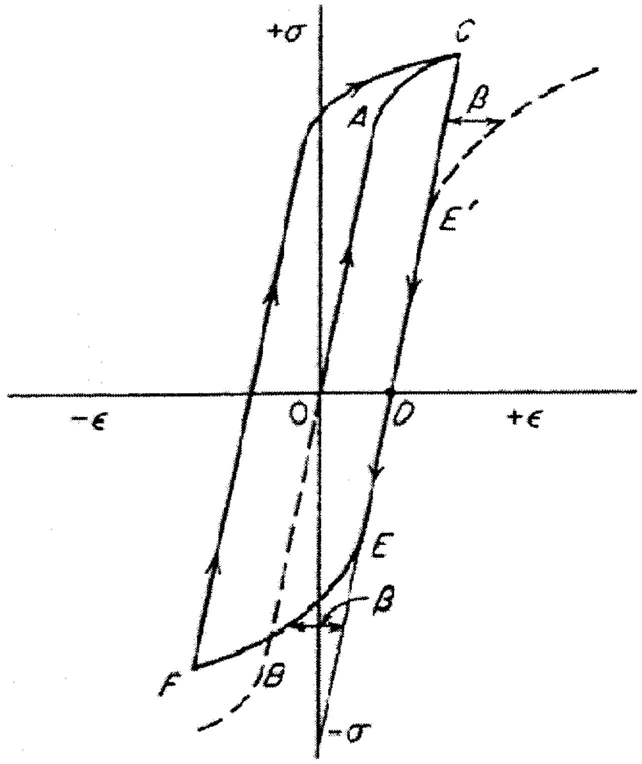

Figure 3: Bauschinger effect [5].

2-4. Hall-Petch Equation and Product Properties

The Hall-Petch equation gives a relationship in which the yield strength of the material increases as grain size decreases. Mc-Elroy and Szopiak [6] collected subgrain data from hot working and annealing experiments and fitted them into the Hall-Petch type Eqn. 4 as follows [7] :

$$\sigma_y = \sigma_0 + k_s d_s^{-p} \tag{4}$$

where σ_y is the yield strength of material, σ_0 is yield stress of annealed material and k_s is the coefficient of subboundary strength and power p equals 1/2. Since the subgrains are more recovered, and larger at decreasing values of Z, some researchers have suggested that subboundaries produced at high temperatures and low strain rates have reduced ability to stop the motion of dislocations. Hot work data gathered from sample plots have indicated that the power in the Eqn.4 should be higher ($p \approx 1$) as suggested by McQueen, Abson and Jonas [8-10] and McQueen and Hockett [1, 11] as seen in Eqn.5 [10]. Hot-work data gathered from sample plots have indicated that power in the Hall-Petch type equation should be higher (Fig 4) [8, 9, 11-14].

$$\sigma_y = \sigma_0 + k_s' d_s^{-q} d_s^{-1//2} \tag{5}$$

It is seen from Eqn.5 that coefficient $k_s = k_s' \, d_s^{-q}$ increases as subgrain size decreases, thus indicating that the strength of the subboundaries increases [1]. For Al and α-Fe the values of ($q \approx 1/2$) and this p has been observed near unity. The coefficient k_s becomes larger for finer and denser dispersion of particles [2].

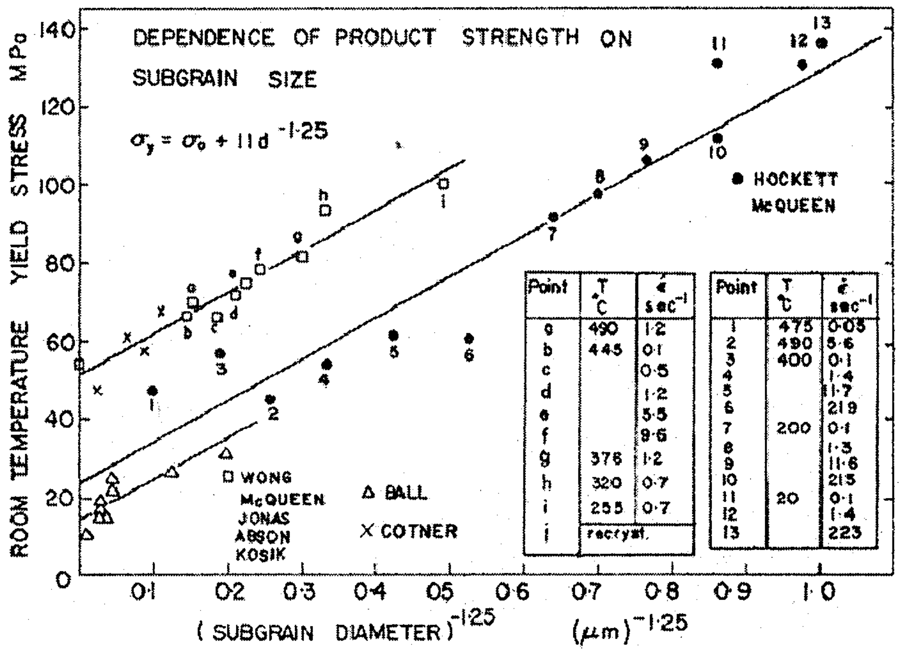

Point	T °C	$\dot{\epsilon}$ sec^{-1}
a	490	1·2
b	445	0·1
c		0·5
d		1·2
e		5·5
f		9·6
g	376	1·2
h	320	0·7
i	255	0·7
j	recryst.	

Point	T °C	$\dot{\epsilon}$ sec^{-1}
1	475	0·05
2	490	5·6
3	400	0·1
4		1·4
5		11·7
6		219
7	200	0·1
8		1·3
9		11·6
10		215
11	20	0·1
12		1·4
13		223

Figure 4: Dependence of room temperature yield stress of Al on subgrain sizes [1, 9-14].

2-5. Constitutive Equations

In hot working, the dependence of stress σ on strain rate $\dot{\varepsilon}$ and temperature T, may be described by one of the following equations [2].

$$\dot{\varepsilon} = A'' \sigma^{n} \exp(-Q_{HW}/RT) \qquad (6)$$

$$\dot{\varepsilon} = A' \exp \beta\sigma \exp(-Q_{HW}/RT) \qquad (7)$$

$$\dot{\varepsilon} = A (\sinh\alpha\sigma)^{n'} \exp(-Q_{HW}/RT) \qquad (8)$$

Where A'', A', A, n, n', β, and α are experimental constants and Q_{HW} the activation energy, T absolute temperature and R universal gas constant [1-4, 16]. Eqn. 6 is called the power law and is used to represent the results of creep and hot working at low stress (<10MPa) [2]. For higher stress levels, Eqn.7 known as the exponential law is employed. Eqn. 8 is used to compare data from hot working and creep testing and is known as the hyperbolic sine law. The value of n is drawn from creep studies of commercial Al, where the power law exponent is related to dislocation climb [15, 17-19]. In creep and hot working of commercial Al, the activation energy is similar to that of self diffusion indicating dislocation climb. For Al, the activation energy is about 150-156 kJ/mol, whereas for alloys with rising alloy content it may be higher.

2-6. Effect of DRV and Hot Ductility

The torsional ductility of Al alloys varies. At $\dot{\varepsilon}$ of $1.3 \times 10^{-2} s^{-1}$, the values of equivalent strain to fracture (ε_f) observed at 270,350 and 400°C were 20, 75 and 90 respectively (Fig 5) [20, 21]. This was indicative of DRV because ε_f increased monotonically from 15 at 220°C to 90 at 400°C. With decreasing hot flow stress as T rises, ductility rises to a peak value and then falls (Fig 5). Below this peak value, there is nucleation of W cracks resulting from differential grain boundary (GB) sliding which is mitigated by enhanced DRV (Fig 5) [20]. There is enhanced intragranular flow that relieves the stress concentrations from differential sliding at grain boundary triple junctions [22]. With rise in $\dot{\varepsilon}$, the DRV is curtailed so that the grain boundary sliding gives rise to W cracks (Fig 5). However as T rises above the peak value, there is increased pore formation that contributes to decline of ductility (Fig 5) [20]. The pores begin to nucleate on GB by vacancy condensation which is facilitated by slip or GB sliding. The growth rate of pores is described by the equation as function (F_n) of grain boundary diffusivity (D) (Eqn 9) [20, 22].

$$G = F_n (D\sigma_n) \qquad (9)$$

where G is cavity growth rate, D= dr'/dt where r' is cavity radius, σ is stress. As solute content increases, the ability to recover diminishes thereby lower end of hot workability range is curtailed due to increasing stress concentration from GB sliding at triple junctions.

When Al, Al-0.8Mg-0.2Mn (5005), Al-1Mn-1Mg (3004) and Al-4.5Mg-0.7Mn (5083) [23] were compared in Fig 6 Al, 5005 and 3004 show much increased ductility due to DRV. In contrast the 5083 alloy shows a low increase in ductility because of the low level of DRV due to solute and presence of Al_6Mn particles. The ductility of Al rises rapidly and attains a peak ε_f at 430°C and afterwards it decreases due to formation of pores at 470°C. A similar kind of behavior with declining effectiveness is seen in 5005 and 3004 alloys. However, in the case of 5083 alloy, ductility continually increases to 510°C because it is much more prone to W cracking. Pore formation is not a problem in 5083 as it is in the softer alloys as shown in Fig 6 [23].

In the case of tension, the solute alloys with Mg exhibit enhanced ductility when compared to Al. This is due to the influence of strain rate sensitivity (m). In tension tests on Al-Mg alloys between 25°C and 400°C, the ductility and strain rate sensitivity rose as temperature and Mg content increase as given by Fig 7 [24, 25]. This occurred due to the phenomenon of solute drag where impurity atoms migrate with dislocations controlling their glide dependence on $\dot{\varepsilon}$. Solute drag gives n =3 in the power law, so that strain rate sensitivity becomes 0.33 [25-29]. Such viscous glide still provides sufficient level of DRV to produce subgrains with neat boundaries. At higher strain rates, the ductility decreases with Mg concentration because of grain boundary cracking. Because strain rate sensitivity is a critical factor in tension, the order of ductility in Al and Al-Mg are reversed from tension to torsion.

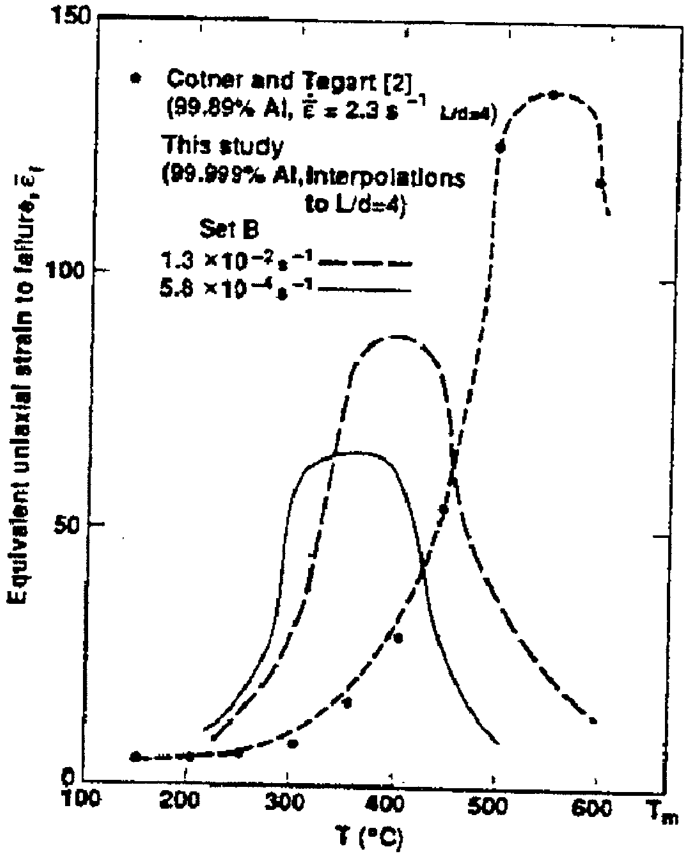

Figure 5: Torsional ductility of 99.99% Al with temperatures at various strain rates [20, 21].

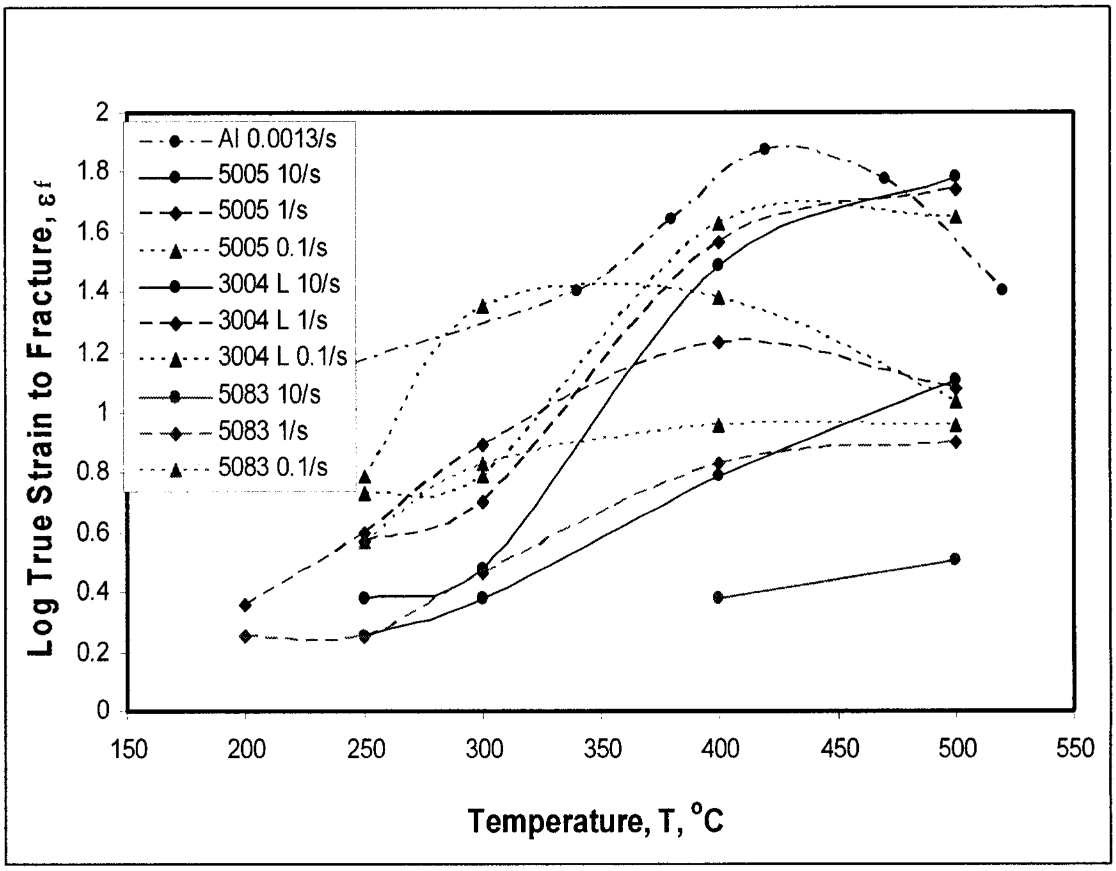

Figure 6: Torsional Ductilities of Al and Al-Mg alloys at 0.0013, 0.1, 1 and $10s^{-1}$ [23].

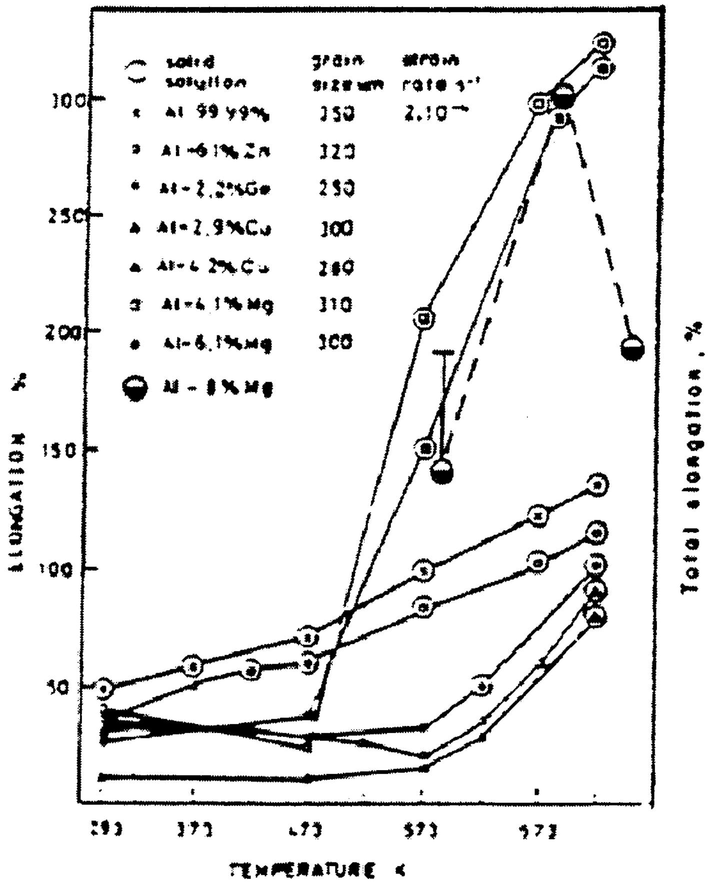

Figure 7: Comparison of ductilities in tension between Al and Al-Mg alloys [23, 24].

2-7. Hot Ductility on Low SFE Metals

At low temperature in Waspaloy (Ni based alloy, 19.5%Cr-13.5%Co) at $1s^{-1}$, there is initiation of transgranular fracture at the intersection of deformation bands with twin or grain boundaries. Furthermore, it is observed in Waspaloy that the mode of fracture changes from transgranular at low temperatures to intergranular at high temperatures (Fig 8). When low SFE metals like carbon, niobium steels, austenitic stainless steels and Waspaloy and Cu alloys are worked in the hot working range (>800°C, $0.07\text{-}23s^{-1}$), there are peaks in flow curves followed by softening to steady state plateaus that were attributed to dynamic recrystallization (DRX) (Fig 9) [30]. Just before the flow curve peak, DRX starts and leads to work softening followed by establishment of a steady state plateau, which is characterized by appearance of recrystallized grains of lower dislocation densities. In Waspaloy, as T rises above $0.5T_M$, there is differential GB sliding at triple junctions which leads to W cracking because intragrain flow stress is high due to little DRV as shown in Fig 10. As T rises above 1038°C, DRX occurs more rapidly and ductility rises to 35. Formation of these new grains move the GB away from the cracks and spherodize them. A similar kind of behavior is seen in Al-Mg-Mn alloys because of partial DRX at large particles. With further rise in T, ductility of Waspaloy rises less steeply but then falls due to melting of precipitates (Ni_3Al) resulting from alloy and impurity contents [30].

Under the effects of solutes and precipitates, GB migration is hindered thereby causing much greater decreases in hot ductility in low SFE metals in comparison to aluminum alloys. This indicates that solute content delays the onset of DRX more seriously than it reduces DRV. It is observed that particles increase the critical strain for DRX thereby permitting fissures to grow rapidly. Carbides and $Ni_3(Al,Ti)$ seem to inhibit nucleation and promote increased cracking in Ni superalloys [30].

Inclusions also promote grain boundary cracking and become more influential at higher strain rates, thereby reducing ductility [23]. Inclusions are usually impurity particles that are retained or formed in liquid metal during the solidification. They consist of simple or complex oxides and their size, shape and distribution influence the mechanical properties. As-cast structures exhibit poor ductility when compared with the wrought microstructures due to larger grain size, grain boundary directionality and presence of second phase particles.

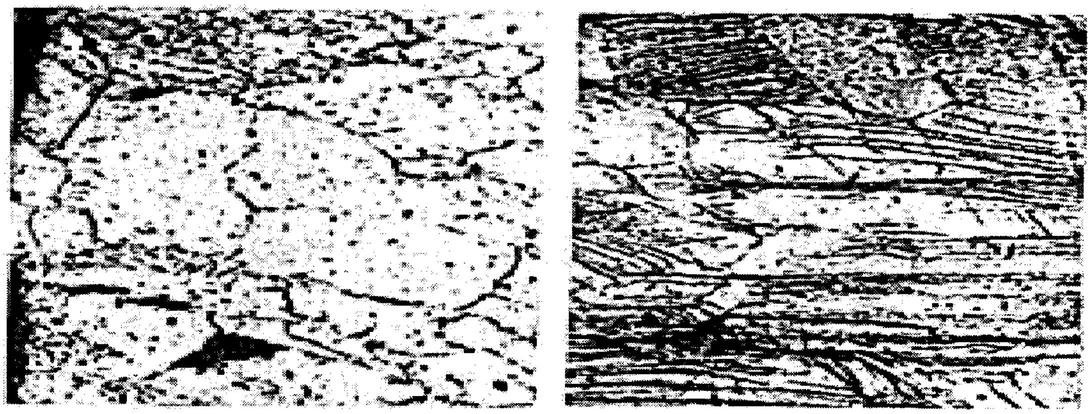

a

b

Figure 8: Cracks occurred in Waspaloy a) 25°C, $1s^{-1}$ to $\varepsilon = 0.6$ b) 954°C, $1s^{-1}$ to $\varepsilon = 1$[24].

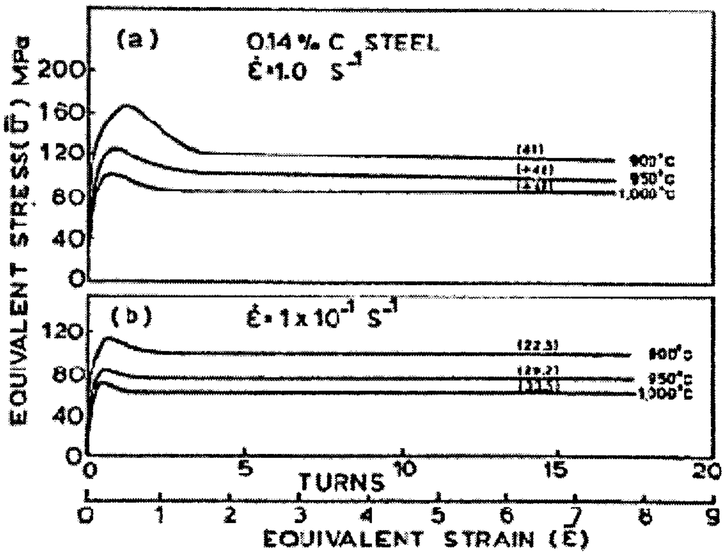

Figure 9: Flow curves of 0.14% C-Steel at 1 and $1x10^{-1}s^{-1}$ [24].

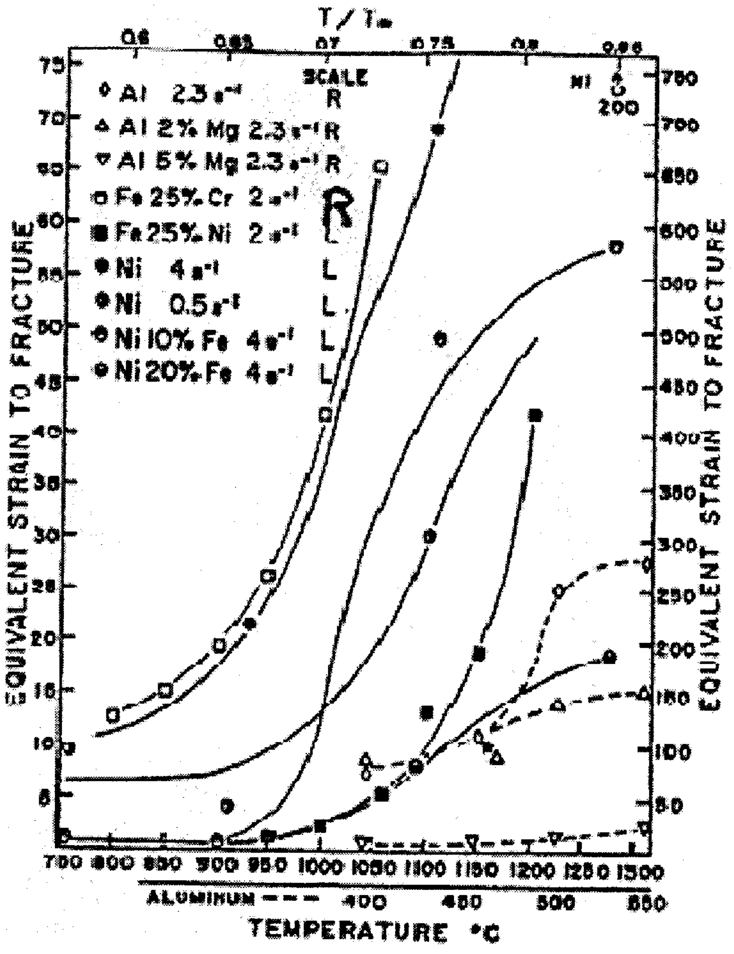

Figure 10: Torsional ductilites of Al alloys, Fe-25%Cr and Ni alloys [20, 30].

2-8. Cold Working

Cold working is an industrial process that is used to deform metals at room temperature. It not only increases the strength of a metal after it has been hot worked but provides better surface finish, closer dimensional tolerances and thinner material. The amount of cold work (CW) in the case of tension is expressed as follows [31] where A_0, A_f is area of the original and final specimens

$$\% \text{ C.W} = [(A_o - A_f)/ A_o]\ 100 \qquad (10)$$

Cold working at 20°C can be best understood by interpreting the stress-strain response of single crystals (Fig 11) [31]. This plot has three stages; Stage I, called the region of easy glide or laminar flow results from operation of Frank-Read sources in the crystals [5]. During this stage, in which slip occurs on 1 slip system, dislocations are able to move over large distances without encountering barriers. Emitted dislocations cause planar pile ups at grain boundaries (GB). The curve shows little increase in strain hardening rate, as a fairly uniform dislocation density is developed in this stage. With increasing strain, Stage II is attained which is known as region of linear hardening. Slip occurs on 2 slip systems with strain hardening at a constant rate and due to a proportional rate of increase in dislocation density. At higher strains, tangles are formed in Al whereas in γ stainless steels and brass pile ups are formed. With rising ε, the dislocation density rises rapidly from 10^4 to 10^{10}mm^{-2} of dislocations [5] (Fig 12).

In high SFE metals notably in polycrystals at strains of 0.2, dislocations start collecting into tangles that form cell walls of increasing density as ε rises above 1 (Fig 13) . With rising strain, the cellular substructure soon reaches a lower saturation size (~0.5μm) and the aspect ratio declines to 1.2. Moreover with increased strain, the cells become separated into blocks by micro bands (MB) or block walls (BW) that arise from new slip systems coming into operation due to lattice rotations. The BW's increase in misrorientation (θ) with strain. It is seen in Fig 14 far up to 50% C.W, there is increased tensile strength and yield strength [32]. The cold worked substructure has a high state of internal energy of 0.04 to $4 kJkg^{-1}$ due to the stored energy of the dislocations. Several factors such as deformation processes, solute additions and SFE play a role in determining the stored lattice energy [5]. In polycrystals, as cold working progresses to higher strains of 4, the GB and persistent BW start to rotate into the direction of rolling creating layer bands with low internal misorientation [33].

At high strains in cold working, Stage III is approached. Stage III known as region of dynamic recovery or parabolic hardening in the range of $0.4T_M$ and $0.5T_M$ at $10^3 s^{-1}$. As seen in Fig 11, there is decrease in the slope of the strain hardening curve. It is a transition phase from cold to hot working called as Warm Working which offers the combined properties of cold and hot working such as improved dimensional control, higher quality surface and low energy costs in α-Fe and austenitic stainless steels. As T rises, cellular substructure of medium size (3-1μm) and low θ are formed (200°C, θ is 4-8°) [33-37]. There is no attainment of steady state regime because the dislocation annihilation does not attain equilibrium with generation [4]. A cellular dislocation substructure is established but the strain induced boundaries have higher misorientation than in hot working. These features show evidence of low T DRV. In the case of low SFE alloys, the substructures are finer and more ragged but in BCC metals like α Fe, substructural developments are similar to Al [33, 38, 39]. Warm DRV is lower as dislocations recovery occurs mainly by cross-slip and very little by climb.

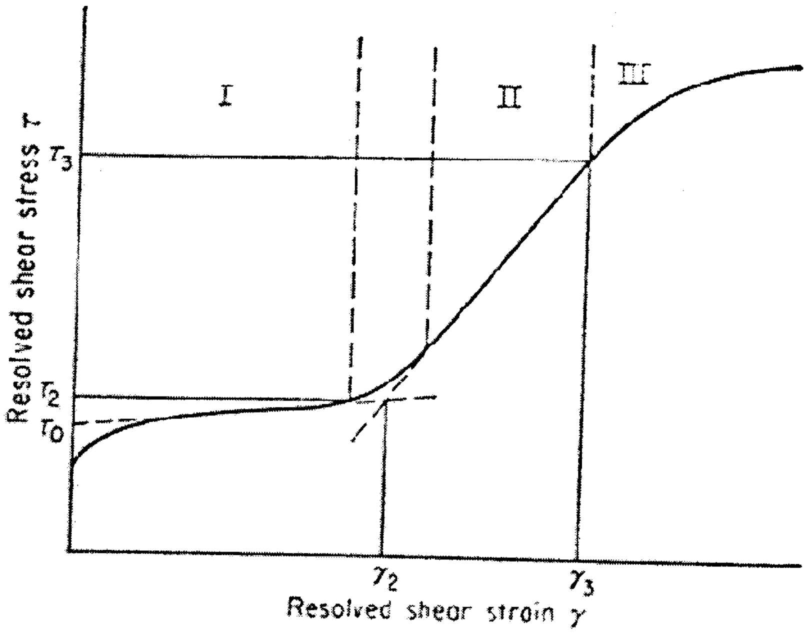

Figure 11: Stress-Strain response in single crystals [40].

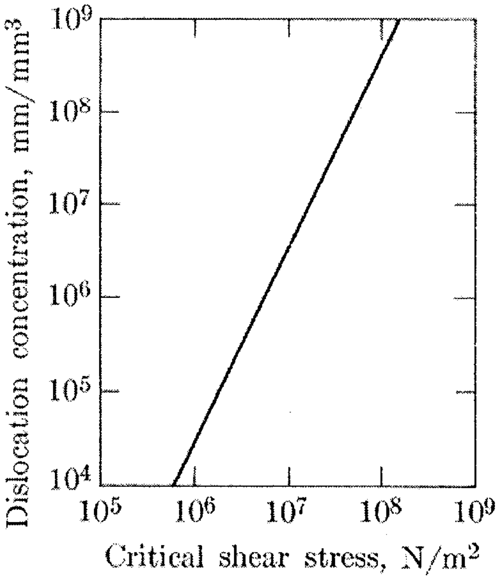

Figure 12: Dislocation density of cold worked metal [31].

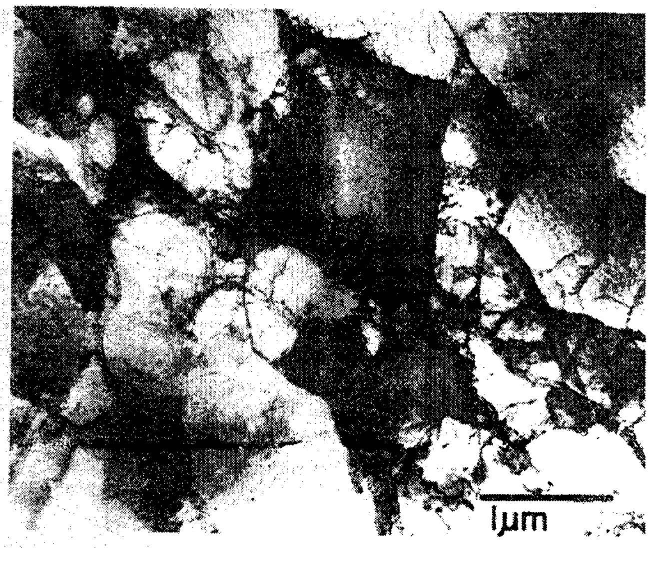

Figure 13: Substructure of 50% C.W Al at $1.4s^{-1}$, 20°C [2].

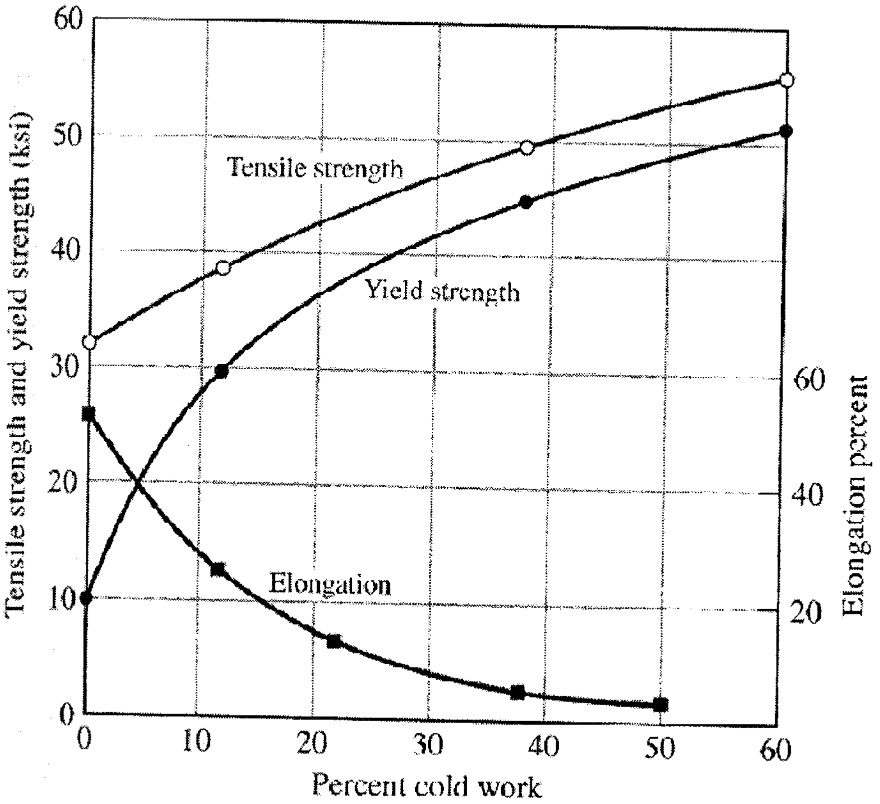

Figure 14: Mechanical properties of metal or alloy up to 50% C.W [34].

2-9. Utility of Annealing

The severely worked substructure produced by cold working, develops increased yield strength as seen in Fig 14, but ductility is considerably diminished. The higher internal energy in the form of tangled dislocations and vacancies can be restored to that of a strain free condition by heating the metal at a high temperature, a process known as annealing [5]. Annealing can be divided into three mechanisms: static recovery (SRV), recrystallization (SRX) and grain growth. In annealing, the stored energy of the cold worked substructure drives SRV and SRX. In SRV, strength is slightly reduced and ductility is improved as a result of decrease in dislocation density due to cross-slip and climb without any observable change in optical microstructure. In contrast, recrystallization is the replacement of cold worked substructure by strain free grains [31]. The nuclei start to form at regions of high dislocation density, primarily at grain boundaries and large second phase particles. The recrystallization rate is influenced by six main factors: amount of prior deformation, temperature, initial grain size, alloy composition, purity of metal and amount of recovery prior to start of recrystallization. It is seen that recrystallization rate increases when there is higher annealing temperature and greater degree of deformation [5]. Also different metal working processes such as rolling and forging can influence rate of recrystallization. In case of SRV, the heavily cold worked microstructure undergoes substructural and property changes like increased formability and lower flow stress whereas grain structure changes are associated with SRX.

2-10. Static Restorations after Cold Working

Researchers [33] have propounded that in Al, two levels of recovery occur after CW. In type 1 SRV, dislocations in the cell interiors are attracted to subgrain boundaries (SGB). This is called polygonization. As annealing temperature increases, the hardness drops more rapidly (Fig 15, 19, 20) [1]. In type II SRV, as annealing temperature and time increases, subgrains grow larger by disintegration of some walls as dislocations are emitted and knitted into neighboring SGB. From Fig 20, it is seen with increase in annealing temperature and time, the subgrains grow from 2 to 10μ and become sharper and regular to rearrange into neat and low energy arrays [33]. Some high angle GB's are formed from medium misorientation boundaries, which form a base for the SRX nuclei [33]. This type II SRV is not recognized in low SFE metals.

When heavily CW metal is annealed, it is observed that tensile strength of the metal show a decline whereas ductility rises steadily (Fig 15) [32,42]. The effect of annealing is compared between Al and Al-0.8Mg. In 75% C.W Al it is observed that, SRX occurred after 1 hr annealing at 350°C (Fig 17) [34]. Whereas in the case of Al-0.8Mg which was 85% CW and annealed at 302°C for 1 hr, there was almost no SRX. Instead there was considerable softening in the substructure due to SRV [32]. With increased T to 316°C, the elongated grains are completely replaced by recrystallized grains (Fig 16) [32, 41-43]. SRX was confirmed by decreased yield strength after cold working from 150MPa to 25MPa in Al at 400°C (Fig 18) [31]. From Fig 18, it can be concluded that rate of drop is less rapid in the initial stages of annealing due to SRV followed by rapid drop due to SRX.

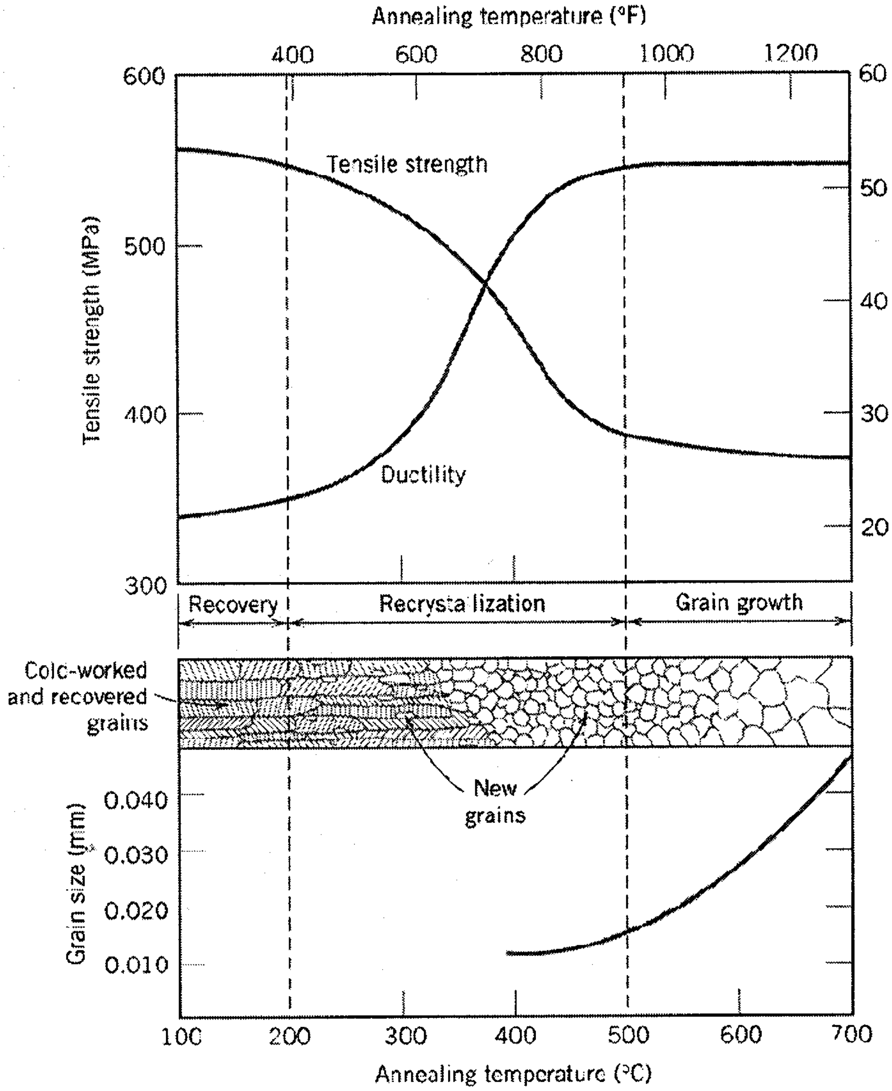

Figure 15: Effect of annealing on cold worked metal [34, 42].

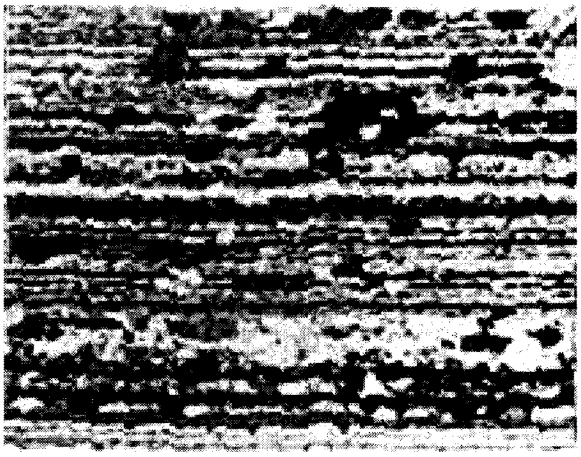

a

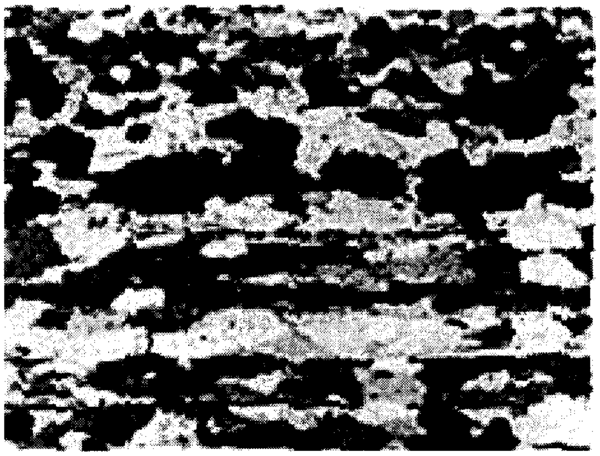

b

Figure 16: 50% Cold worked Al-0.8Mg annealed at a) 302°C b) 316°C [34].

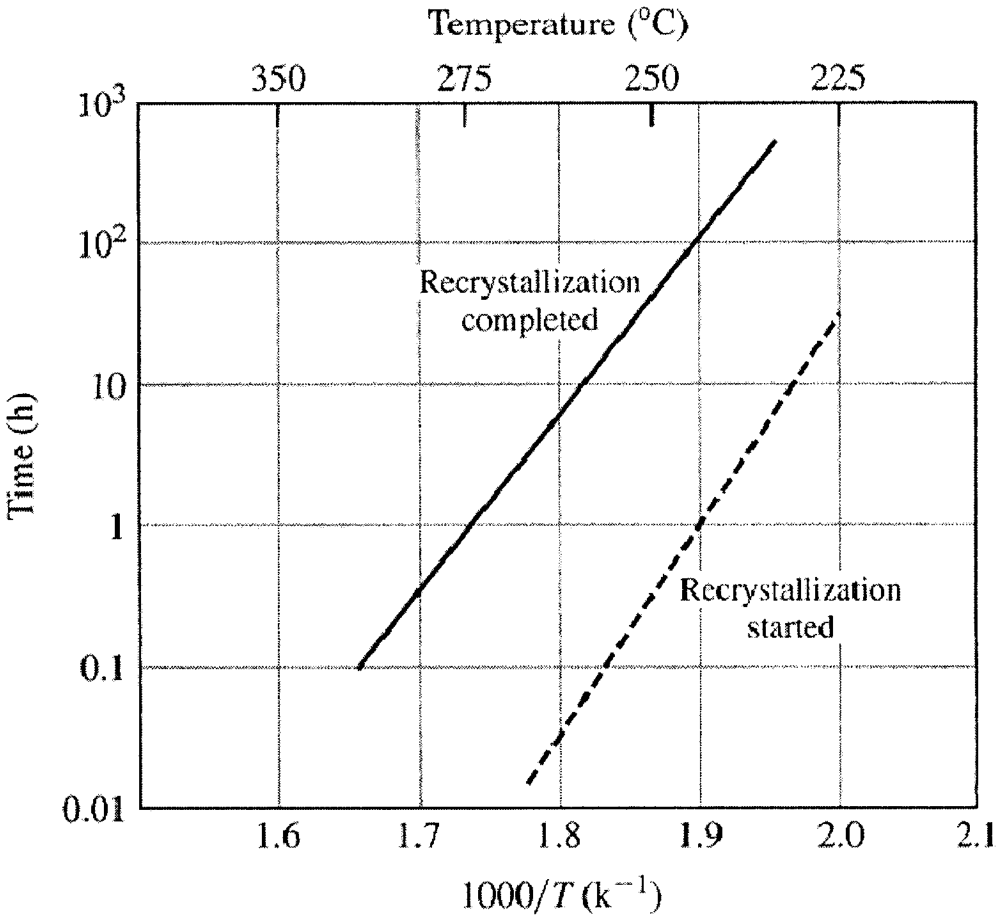

Figure 17: Recrystallization rates of Al under various annealing times and temperatures [34,43].

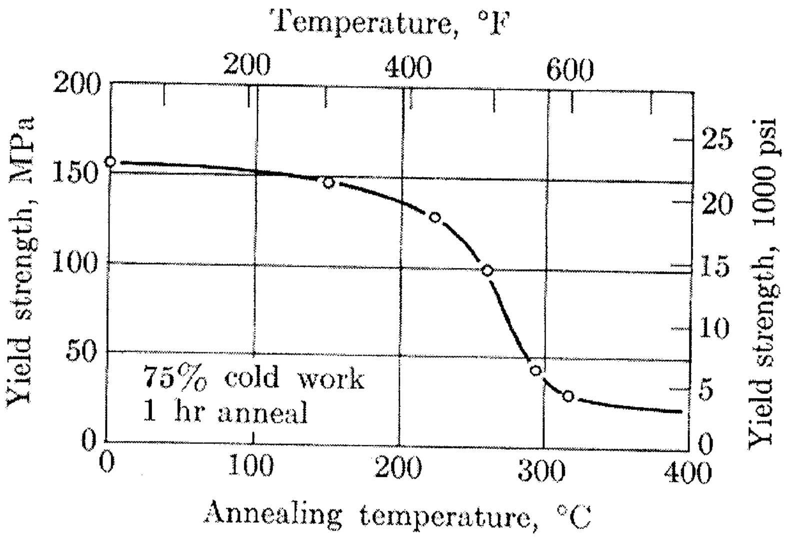

Figure 18: Effect of annealing temperature on yield strength of Al [31].

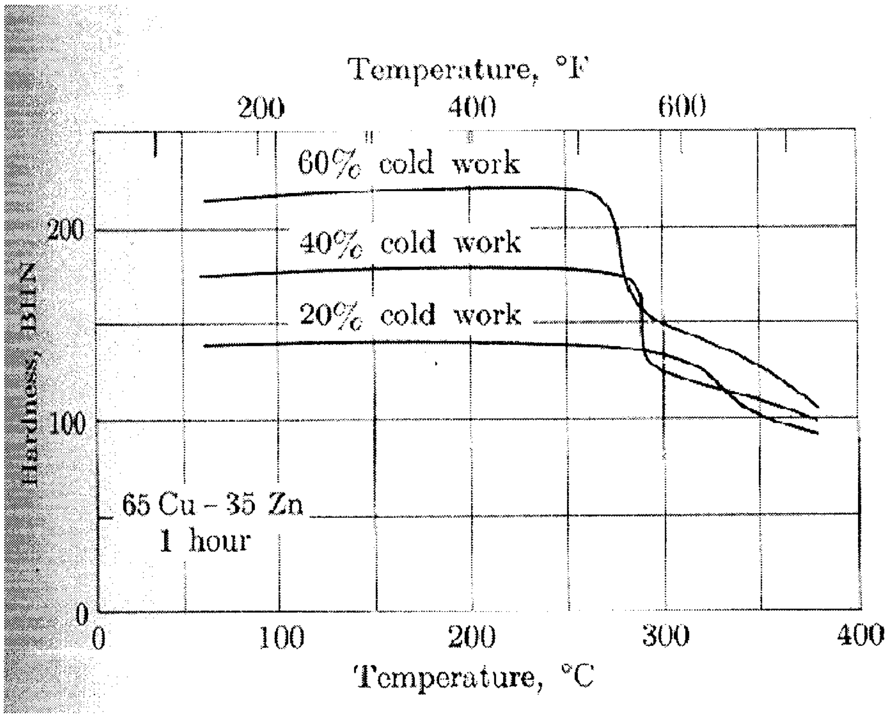

Figure 19: Plot showing earlier drop in hardness values for greater % C.W [31].

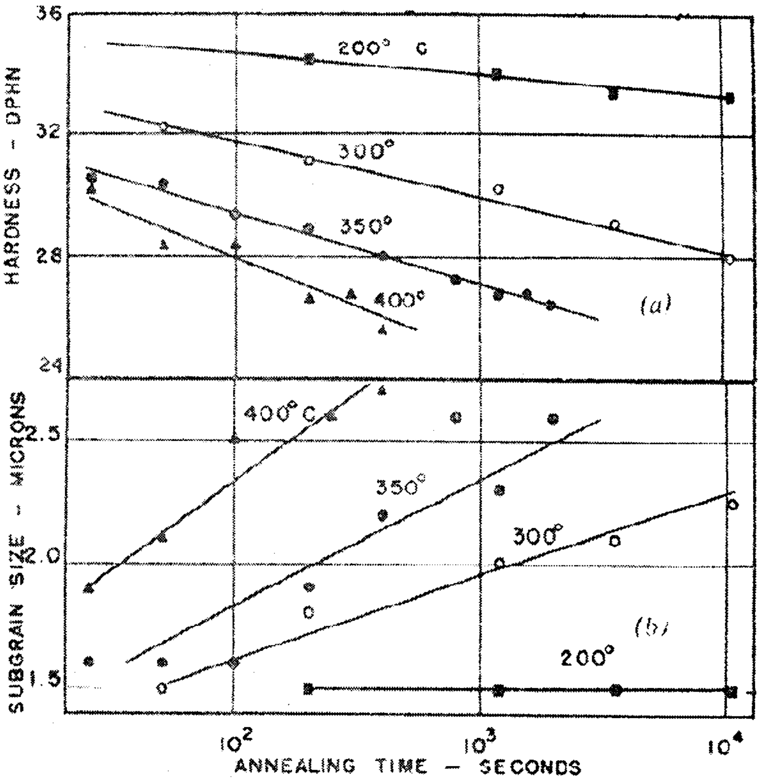

Figure 20: Drop in Hardness values and increase in subgrain size with increase in annealing temperature and time for 80% C.W Al crystal [2].

2-11. Static Restorations after Hot Working

At the end of deformation, the hot worked substructures may be subjected to two different conditions known as holding temperature (T_H) where each specimen is held at the deformation temperature and annealing temperature (T_A) where all are annealed at a specific temperature. In multi stage processing, the static restoration between passes has an influence on the hot worked metal's properties for the subsequent pass. It is therefore important to simulate such a schedule where the progress of SRV and SRX ($T_H = T_D$) at various holding times can be found by microscopic examination and by strength and hardness measurements [44, 45]. A technique to find out the fractional softening (FS) during the holding after a certain deformation stage relative to the strain hardening from the original strength σ_o at the start of the deformation is as follows (Eqn 11) [44-50]

$$FS_i = (\sigma_{mi} - \sigma_{r\,(i+1)}) / (\sigma_{mi} - \sigma_o) \qquad (11)$$

Where i is the number of the stage, σ_{mi} is maximum stress in the stage and $\sigma_{r\,(i+1)}$ is the strength on reloading after the interval (Fig 21). This isothermal method indicates a rapid rate of SRX because there is no SRV during cooling or reheating. The progress of SRX can be studied from the sequences of accelerated softening and plateau in the FS versus time curves [46]. "If there are multiple stages and FS_i is found to be less than unity then there is partial SRX and strain accumulation" [49, 50]. The FS values for Al 99.997 and Al-0.5Mg at various working temperatures and different times were reported by McQueen et al. [51]. It is seen that FS values at 100°C for Al 99.997 was 9% for 30s compared to 7.7% for Al-0.5Mg for 15s. With increasing ε values of 0.4 and 0.8

corresponding with temperature rise, the FS values increased proportionally for both alloys (Fig 21). Restoration increases with both duration of interval and prestrain [52].

When held at different $T_H = T_D$ for particular holding times, SRX is observed for Al 99.997, Al-0.5Mg and Al-0.96Mg. In Al 99.997, the dislocations inside the subgrains start rearranging followed by subgrain growth. This leads to reduced flow stress on further forming [17]. On further holding, SRV drives the subgrains towards nucleation and SRX. At a ε of 2.45 and 375°C, SRX was complete in 15.9s. Whereas as $T_H = T_D$ increased to 450°C, the specimen underwent completely SRX in 2.2s. The increased thermal activation during the holding speeds up the recrystallization. The time for complete recrystallization (t_R) of Al 99.997 is only 2.2s compared to 16s for Al-0.5Mg and Al-0.96Mg at 450°C (Fig 22, 23,24). Therefore it is concluded that t_R is higher for alloys with solute content. This may be attributed to higher activation energy and decrease in grain boundary mobility due segregation of Mg atoms to GB in Al-Mg alloys [51].

Cotner and Tegart [53] showed that under constant deformation conditions as Mg content rises above 2%, t_R is only 42s compared to 200s for Al 99.95;. the possible cause is that Mg greatly increases the energy driving force. This can be confirmed by increased flow stress values of 70MPa for Al-Mg alloys compared to 35MPa in Al 99.997 [51] (Fig 25). Subgrain size decreases as Mg content rises.

When Al is annealed at 400°C, there is higher degree of SRV over a period of time than cold worked Al due to high degree of DRV. There is 50% softening of Al in contrast to Cu and Ni [55-60]. The dislocations inside the subgrains start rearranging followed by subgrain growth. This leads to reduced flow stress on further forming. On further holding, SRV allows some subgrains to develop nucleation and SRX. SRX takes place but slowly when compared to FCC metals of lower SFE [55]. This happens due to reduced strain energy resulting from high DRV. In the case of solid solution alloys like Al-2Mg, SRX is slowed down due to segregation of Mg on grain boundaries.

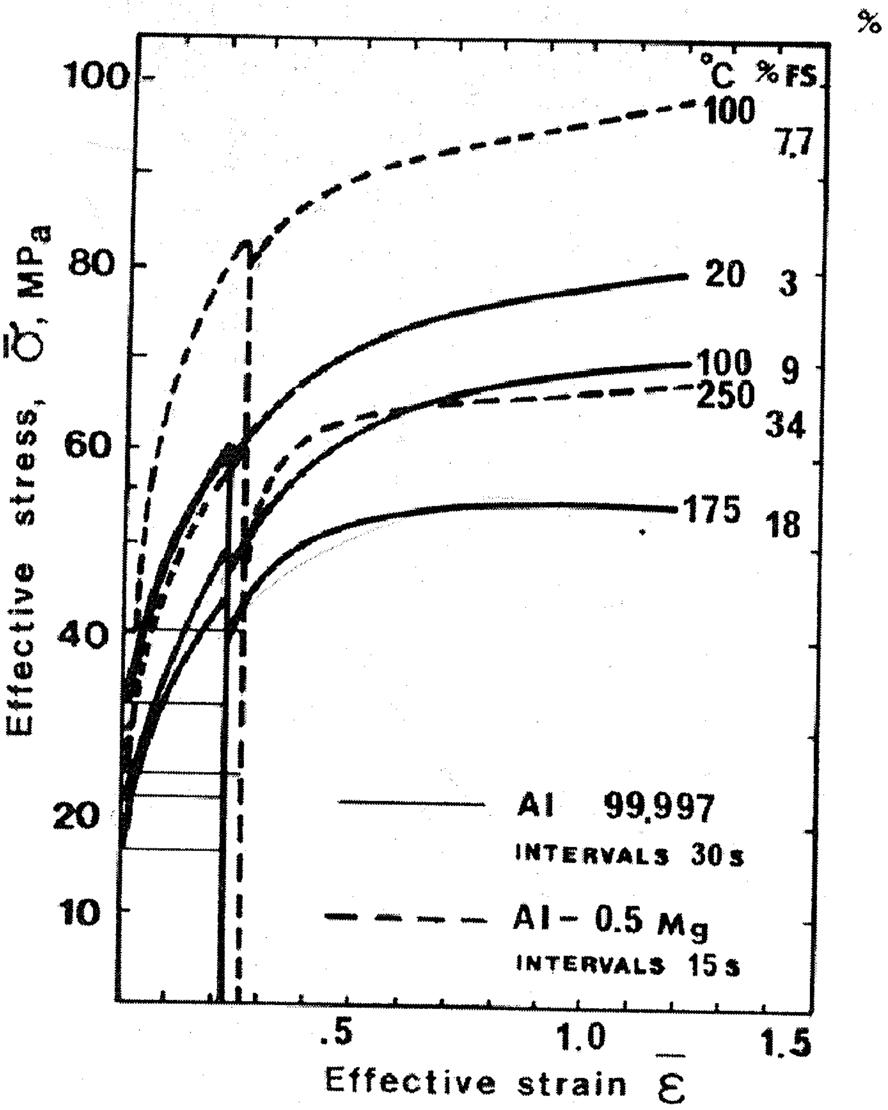

Figure 21: Stress Strain Curves at moderate temperatures for Al 99.9997 and Al-0.5Mg at $0.41s^{-1}$ unloaded for intervals of 30 to 15s [51].

Figure 22: Micrographs of Al 99.997 exhibiting deformed grains ($\varepsilon = 2.45$)

450°C, 2.2s $X_R = 0.95$ [51].

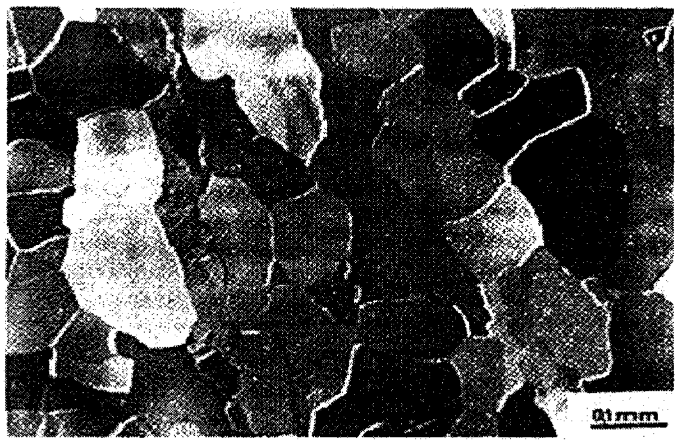

Figure 23: Micrographs of Al-0.5Mg exhibiting

deformed grains ($\varepsilon = 2.45$) 450°C, 16s $X_R = 0.95$[51].

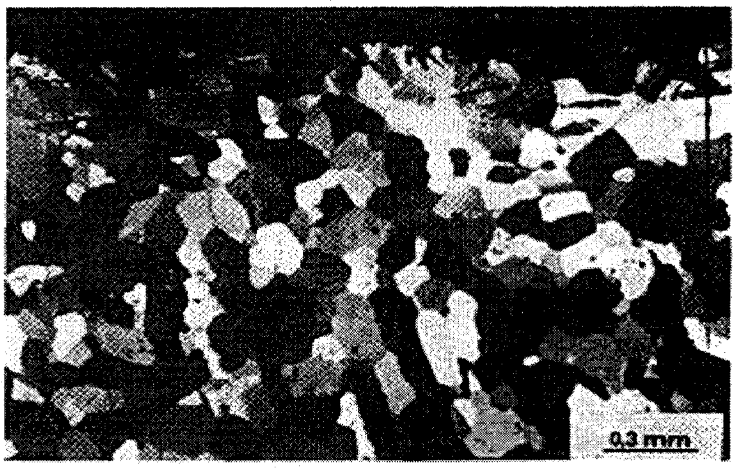

Figure 24: Micrographs of Al-0.96Mg exhibiting deformed grains ($\varepsilon = 2.45$) 450°C, 15s $X_R = 0.95$ [51].

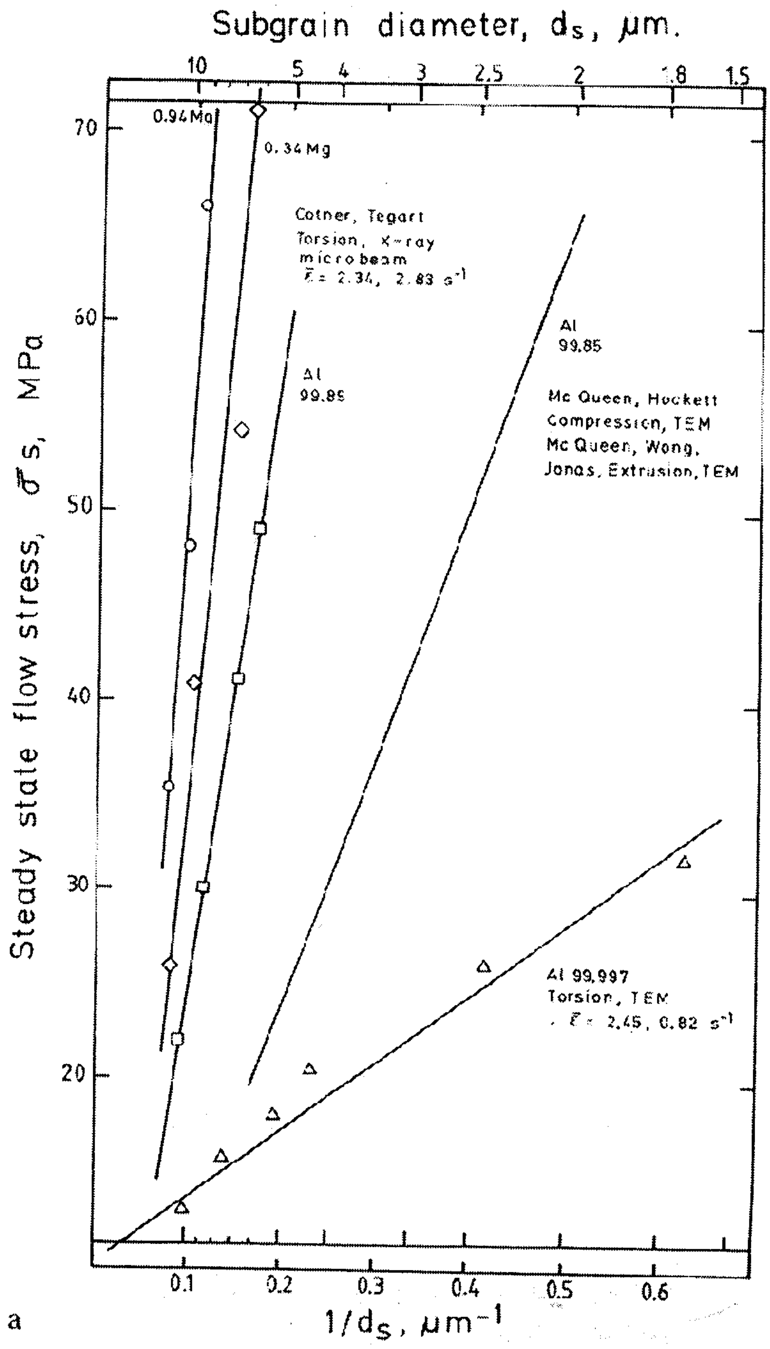

Figure 25: Relation between subgrain size and steady state flow stress for Al and Al–Mg alloys [51]

2-12. Grain Growth

Grain growth occurs when strain free grains are heated for prolonged time at or above the recrystallization temperature. When brass (70% Cu -30% Zn) was heated for 10 min at 700°C, there was a decrease in grain boundary area (mm^2/mm^3) due to extensive grain growth (Fig 26, 27) [31]. It caused a big drop in hardness value from 60BHN to 33BHN due to increased grain size associated with decrease in grain boundary area and is also related to Hall-Petch effect. Grain growth is strongly dependent on T and can be inhibited by the presence of second phase particles [7]. Grain growth can be reduced by having a single phase and plastically deforming it followed by recrystallization.

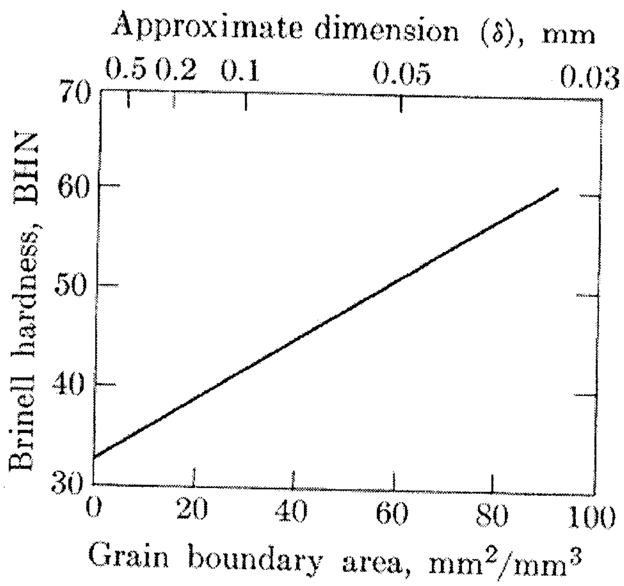

Figure 26: Relation between grain boundary area and hardness of Brass [31].

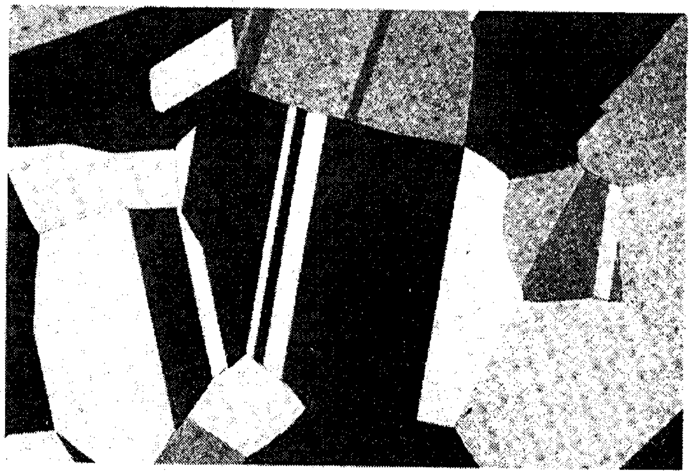

Figure 27: Grain Growth of Brass at 700°C in 10 min [31].

CHAPTER THREE

EXPERIMENTAL PROCEDURE AND ANALYSIS OF DATA

3-1. Introduction

In order to simulate conditions of hot working at high temperature and strain rate, torsion testing has been employed by metallurgical engineers for many years. It is useful in determining many mechanical properties and evaluating forgeability of materials. It basically comprises twisting a cylindrical bar specimen with a reduced diameter gage section between a fixed grip and a rotating grip. Large amounts of strain and constant strain rates can be achieved in torsion without plastic instabilities such as necking and barreling [61].

Minor factors playing a role in torsion testing mode must be taken into consideration and are as follows. In torsion, the strain and strain rate increase from zero on the axis to the surface. This has to be taken into account when stress and strain curves are calculated. Due to high temperature damage mechanisms, there may be possibility of fracture at high strains [61].

3-2. Test Material

Aluminum samples were supplied in a single batch and their alloy chemistry is given in Table 1. Torsion specimens were machined with one end having rectangular cross section while the other end had a threaded portion. This was done for easy insertion and removal without straining the test piece. When the specimens are heated they expand lengthwise by 0.2-1mm, buckling is prevented by slip in the slot grip [61].A diagram of the test specimen with gauge and shoulder section is shown in Fig 28.

Table 1: Chemical composition of Al 99.9%

Alloy Composition %	Al	Fe	Si	Mn
	99.9	0.03	0.02	0.01

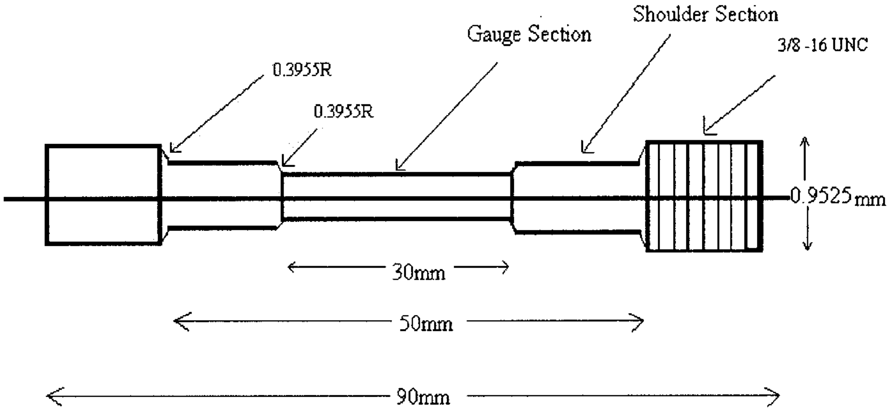

Figure 28: Test specimen geometry [2].

3-3. Heat Treatment, Thermal Cycles and Testing Procedure

Before the actual testing, the Al specimens were heat treated in a Lindberg Hevi-Duty high temperature resistance furnace at 500°C for three hours. Heat treatment was necessary to provide grain size uniformity. The furnace temperatures were controlled by a thermocouple which was pressed against the centre of the gauge section. Argon gas was used to prevent oxidation of Al specimens [2].

The specimens were then subjected to series of strain path tests either in the forward or reverse direction (Table 2). The average flow stresses for each stage were calculated for the given test conditions in accordance with the flow stress values of the flow curves. The standard values of Q, α, n and A were taken from various papers [6,13]. The as-worked specimens were then microscopically examined using optical microscopy. Annealing operations were performed on the as-worked specimens at 400°C to detect possible changes in microstructure. Micrographs were taken for the as-worked and annealed specimens with torsion axis in the horizontal direction.

3-4. Torsion Machine

The torsion machine was constructed and designed by Fulop et al [61]. The lathe bed 2.5m long provides longitudinal alignment for the motor and supports the furnace system. The machine is equipped at one end by a dual valve hydraulic motor and at the other end by the 113 Nm torque cell (Fig 29) [2]. The motor twists the specimens while the torque cell measures the resulting torques. The hydraulic motor has low flow and high flow servovalves which provide twist rates of 0.02 rev/sec to 10 rev/sec. The motor can provide a maximum torque of 120Nm and has pumping capacity of 750cm^3/sec (Fig 30) [2, 61]. The torque cell output is directed to a transducer conditioner circuit. To obtain accurate output, the load cell's range is set to 100%, 50% or 10% full scale (Fig 31) [2, 61].

A closed loop system is used for the machine control. Using conventional feedback control, comparison is made between the command value and feedback signal from the rotary transducer. An IBM-PC compatible 1 GHz was used to record the twist and torque values at fixed intervals of time.

The specimens are gripped by two nickel based (INCONEL 713C) [2] loading bars which are connected to the hydraulic motor and torque cell by self aligning chucks. These loading bars are 1" in diameter with 309 stainless steel end adapters. In order to facilitate specimen insertion and removal for manual quenching, the torque bar, bearing assemblies and torque cell which are on the lathe bed can be moved axially. The lathe carriage can be locked in its position during the test by bolting it down to the lathe bed.

Manual quenching is done by removing the specimen from the furnace shell longitudinally by displacing the entire torque cell assembly and showering it with water in about 3s (Fig 32).

An electrically heated 4 tube radiant furnace is used for test specimen heating (Fig 33) [2,61]. It has a water cooled aluminum shell which reflects and focuses the thermal energy to the centre line. The furnace is capable of maintaining a maximum temperature of 1100°C. The specimen is enclosed in a quartz tube within which argon atmosphere is maintained . The quartz tube ends are sealed by water cooled sleeves.

Temperature control is done by an external programming device known as process programmer along with proportioning controller. The test temperature is set by the process programmer. A K-type (chromel-alumel) thermocouple supplies the feedback signal back to the controller. It is placed against the gauge section approximately 1/4" from the stationary shoulder by tying it to the specimen by INCONEL wire. Test temperatures used in the furnace ranged from 400-500°C.

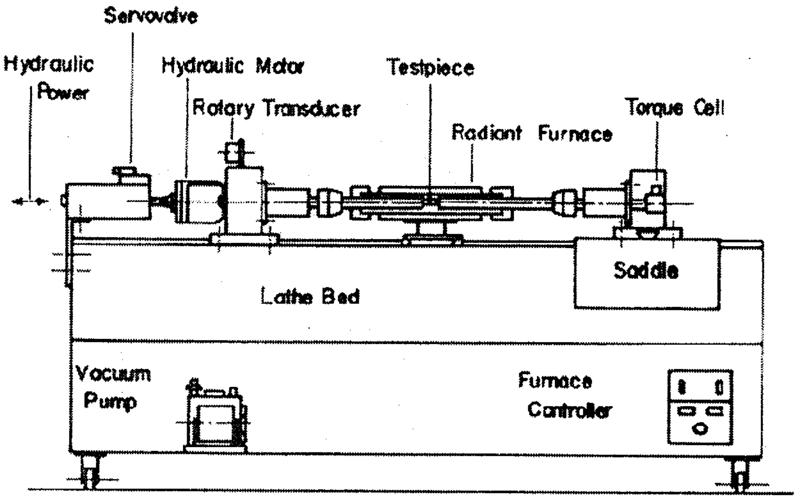

Figure 29: Layout of Hot torsion machine [61].

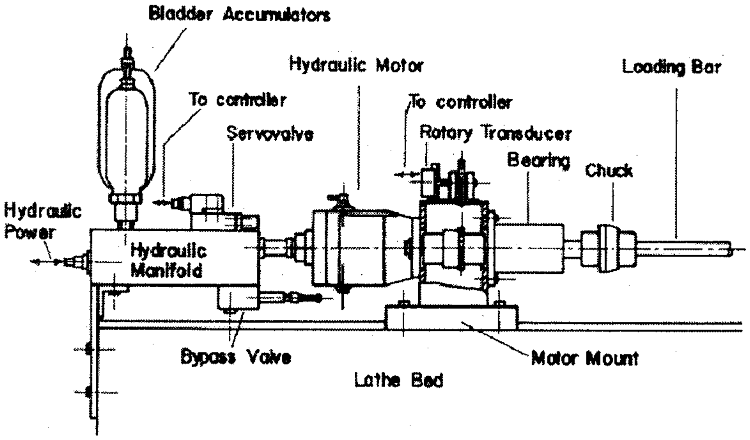

Figure 30: Strain control and measurement subsystem [61].

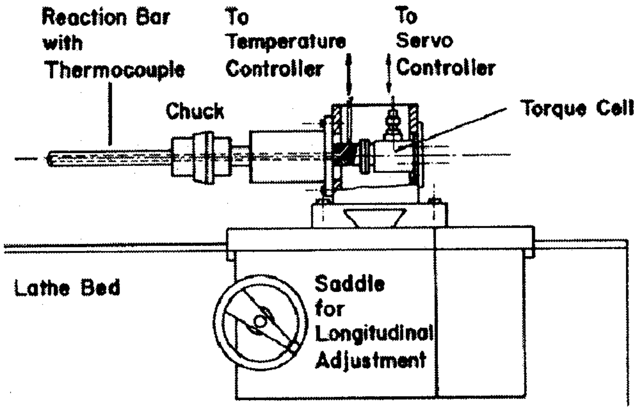

Figure 31: Torque Cell Assembly [61].

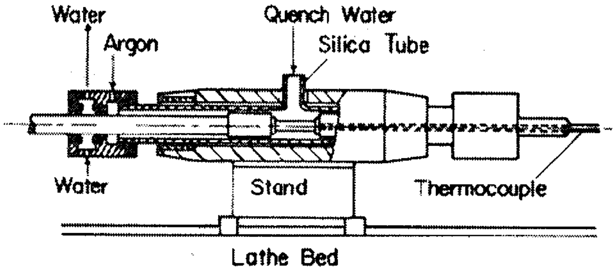

Figure 32: Diagram of Radiant Furnace [61].

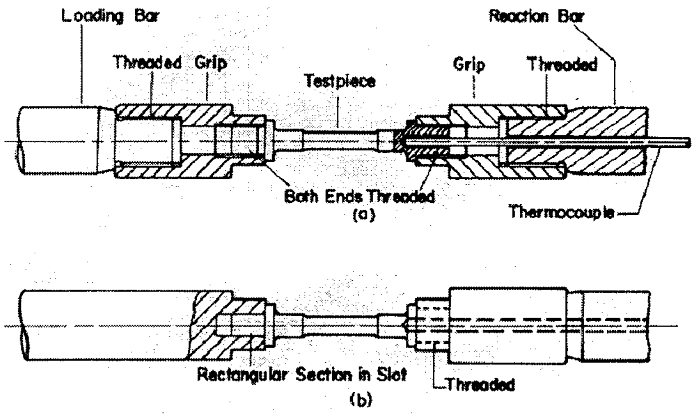

Figure 33: Schematic Diagram of test Specimens [61].

3-5. Stress and Strain Conversion

In metals, determination of strain rate and stress is essential for analyzing deformation behavior. In the case of solid specimens, the stress at a point is expressed by calculating the normal and shear stresses acting on three mutually perpendicular oriented planes passing through the point [2,7]. The stress tensor can be reduced to 3 normal stresses acting on mutually orthogonal planes; the plane of normal stress and zero shear stress are known as principal planes. Similarly there are principal strains associated with these stresses. As in the case of torsion test, it is observed that there is a radial distribution of stress and strain rate from zero at the axis to a maximum at the surface.

Recorded data from the torsion is in the form of torque versus angle of twist. Hence torque (Γ) must be converted to torsional surface shear stress (τ) using the Fields-Backofen equation [61]

$$\tau = (3 + m + n'') \Gamma / 2\pi r^3 \qquad (12)$$

where Γ = Torsional moment

m = strain rate sensitivity

n''= strain hardening exponent

r = specimen gauge radius

The torsional strain on the surface (γ) of the specimen [2] is calculated using

$$\gamma = 2\pi rN/L_o \qquad (13)$$

where N = number of turns

L_o = Original gauge length

The calculated torsional shear stress and strains must be converted into equivalent stresses (σ_{eq}) and strains (ε_{eq}) using von Mises yield criterion [61]

$$\sigma_{eq} = \sqrt{3}\,\tau \qquad (14)$$

$$\varepsilon_{eq} = \gamma/\sqrt{3} \qquad (15)$$

3-6. Microscopic Examination

All the samples went through a series of grinding and polishing steps before they were etched. Rough grinding was done on the samples using silicon carbide (SiC) grit paper of sizes 240,320, 400 and 600 respectively. This was done to produce even surface with scratches in one direction. Then fine grinding was done using SiC grit paper of sizes 800 and 1200. Liquid hand-soap was used for easy removal of dirt during the process and facilitate elimination of scratches. After each step of the grinding, the samples were washed with distilled water to remove grit particles sticking to the sample. Once the samples were almost free of scratches and dirt marks, they were rough polished on pellon I polishing cloth using diamond extender (oil base) as the lubricant. Now, the sample was washed with ethanol to remove traces of oil sticking onto the specimens. After that, fine polishing is done to produce a shining surface using colloidal silica suspension (0.05μ). The specimens were thoroughly washed with distilled water to remove particles. Now the samples are ready for etching. The etchant used in this experiment was a solution of hydrofluoric acid (10%) and distilled water (90%). The etching time was roughly 7 mins.

The samples were microscopically examined using an Olympus BX 51M optical microscope and photographs were taken using Q-Imaging camera which was connected to the microscope.

CHAPTER FOUR

EXPERIMENTAL RESULTS

Overview

99.9% Aluminum specimens were subjected to strain path change tests during high temperature deformation and were classified into five groups such as I, II, III, IV and V respectively (Table 2). In group I, hot torsion tests were performed for five specimens of 99.9Al at 400°C, $0.1s^{-1}$. These specimens were strained up to strains of 0.2, 0.5, 1 and 5 respectively. Group II were also done at same temperatures and strain rate but followed by change in strain path by reversing strains from 0.5 to 0.2 or 0.5 to 0. In group III series, three specimens were tested at 400°C and strain rates of 0.004 or $0.1s^{-1}$, under reversing strains of 0.5 to 0.2 or 0.5 to 0 and also advancing 0.5-1. Group IV tests were done at constant Z values under 400°C, $0.004s^{-1}$ or 500°C, $0.1s^{-1}$ to advancing strains of 0.5. In the last series specimens were subjected to change in temperature from 400 to 500°C at $0.1s^{-1}$ with advancing strain of 0.5 followed by reversing strains of 0.2 and 0. The as-worked specimens in group I and group II were also annealed at 400°C at equal logarithmic intervals to detect the occurrence of SRX.

Flow curves of σ versus ε were plotted so that the critical points could be discussed in relation to deformation parameters and subgrain sizes. The measured flow stresses were compared with values calculated from the literature (Tables 2, 3, 4). Optical microscopy was conducted on as-worked group I and group II specimens to detect the occurrence of restoration mechanisms by observing characteristics such as grain elongation, subgrains and deformation bands. Annealed specimens are then discussed in comparison with each other to detect partial and complete SRX.

For test conditions 400-0.1, 400-0.004 and 500-0.1 either in the forward or backward path, the average plateau flow stresses are calculated (Table 3). Values from specimens 1 and 2 are omitted from the average as they seem to be too low; this may be due to large grain size.

The flow stresses (σ_s) are also calculated for conditions 400-0.1, 400-0.004 and 500-0.1 using the following equation

$$Z = \dot{\varepsilon} \exp(Q/RT) = A(\sinh \alpha\sigma_s)^n \qquad (16)$$

where Z: Zener-Hollomon parameter (s^{-1}), $\dot{\varepsilon}$: strain rate (s^{-1}), Q: activation energy (150kJ/mol), R: universal gas constant (8.314J/mol K), T: temperature (K), α: constant ($0.0054 MPa^{-1}$), A: constant (s^{-1}) (LogA=8), n: constant (7) [6].

The calculated values for the flow stresses are found to be 29.26MPa (400-0.1), 22.18MPa (400-0.004), 21.64MPa (500-0.1) (Table 4). The logZ values for 400-0.1,400-0.004 and 500-0.1 are found to be as 10.64, 9.24 and 9.13 (Table 4).

Table 2: Test conditions of 99.9%Al samples (Flow stress, σ).

Test No	First Stage			Second Stage				Figure No
	T, $\dot{\varepsilon}$ °C, s^{-1}	Strain ε	Final σ MPa	T, $\dot{\varepsilon}$ °C, s^{-1}	Strain ε	Initial σ MPa	Final σ MPa	
	Group I							
1	400-0.1	0.2	23					34
2	400-0.1	0.5	23.5					34
5	400-0.1	0.5	26	400-0.1	→1	26	26.5	34
6	400-0.1	0.5	27.5	400-0.1	→5	27	27.5	34
	Group II							
3	400-0.1	0.5	27.5	400-0.1	0.2←	27.5	27.5	39
4	400-0.1	0.5	27.5	400-0.1	0←	27.5	27.5	40
	Group III							
7	400-0.1	0.5	27.5	400-0.004	→1	22.5	22.5	43,50,51
8	400-0.1	0.5	27.5	400-0.004	0.2←	20.5	22.5	44
9	400-0.1	0.5	27.5	400-0.004	0←	20.5	22.5	45,50
	Group IV							
10	400-0.004	0.5	22.5					46,50,51
11	500-0.1	0.5	25					47,48,51
	Group V							
12	400-0.1	0.5	27.5	500-0.1	→1	22	25	48
13	400-0.1	0.5	27.5	500-0.1	0.2←	20	25	48
14	400-0.1	0.5	27.5	500-0.1	0←	21	25	49

Table 3: Measured average plateau stresses for test conditions.

Test conditions $T - \dot{\varepsilon}$ $^{o}C - s^{-1}$	Average measured plateau stresses MPa	
	Forward path	Reverse path
400-0.1	27.5	27.5
400-0.004	22.5	22.5
500-0.1	25	25

Table 4: Calculated flow stresses and logZ values for the given conditions.

Test conditions $T - \dot{\varepsilon}$ $^{o}C - s^{-1}$	Calculated Flow stresses (σ_s) MPa	logZ	Subgrain size d μm
400-0.1	29.26	10.64	4.5
400-0.004	22.18	9.24	6.5
500-0.1	21.64	9.13	7.5

4-1. ANALYSIS OF FLOW CURVES WITH METALLOGRAPHY

4-1.1. Group I

Four specimens were torsion tested to various strains of 0.2, 0.5, 1 and 5 respectively (Table 2). The flow curves indicate that there is initial strain hardening. The curves then settle into a steady state plateau at strain of 0.2. In specimen 1, a flow stress of 20MPa is achieved at a strain of 0.2, but in specimens 2, 5 and 6 flow stresses reaches 23, 26 and 27MPa at strains of 0.5 (Fig 34). In the second stage, in the forward path flow curves of specimens 5 and 6 reach 26.5 and 27.5MPa up to strains of 1 and 5, thus remaining unchanged. Under 400-0.1, the average measured flow stresses (Table 3) almost agree with the calculated flow stress values (Table 4). Specimen 1 and 2 have slightly lower values than the calculated flow stresses which may be due to initial larger grains in the specimens. The constant flow stress values at high strains without a prior peak indicate the occurrence of DRV in the specimens.

The as-worked specimens were microscopically examined. Specimen 1 revealed the evidence of deformation bands and large grains of somewhat equiaxed character along the surface (Fig 35). Specimen 2 showed elongated grains and medium grains of equiaxed character with deformation bands (Fig 36). In specimens which had second stage up to strains of 1 and 5, there was strong presence of deformation bands near the surface which was evidence of high straining in the surfaces. Elongated grains of medium size with strain markings were noticed. As effect of strain in the centre is minimum, there were large grains with little or no strain markings (Fig 37, 38).

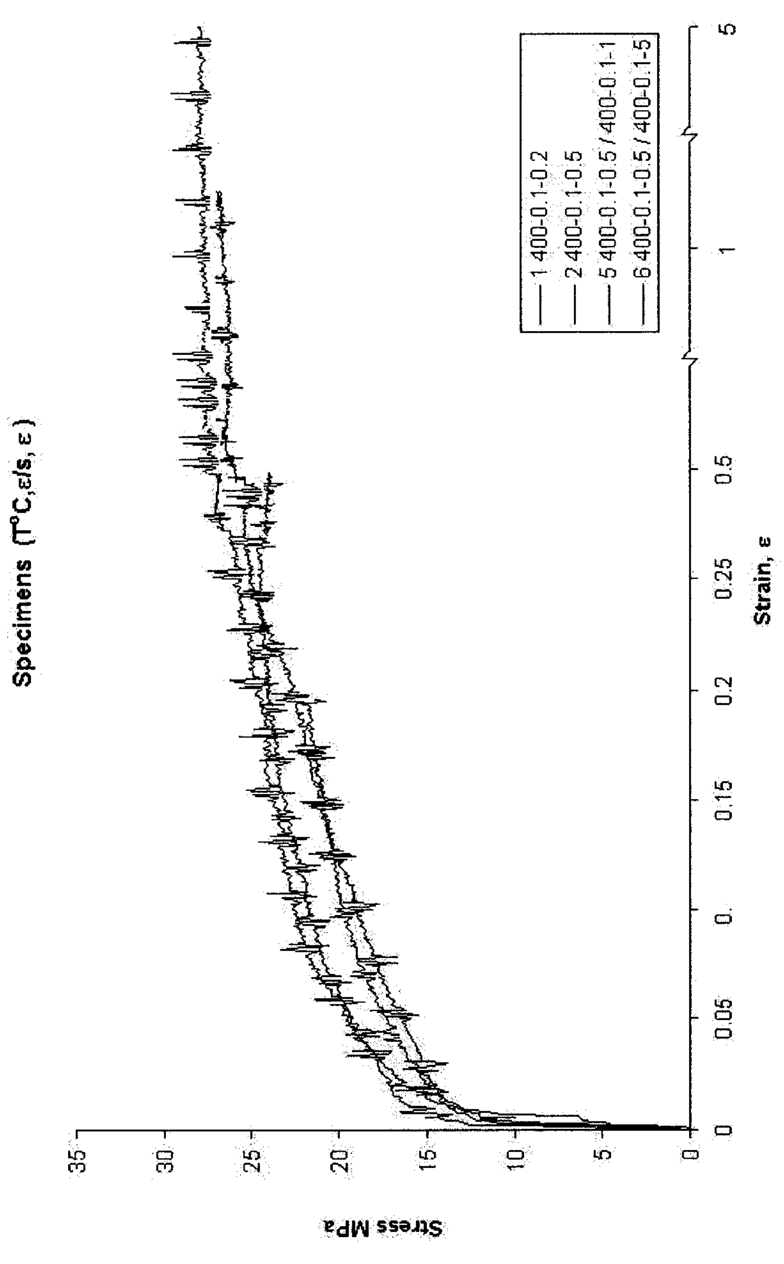

Figure 34: Flow curves of Al at 400°C, $0.1s^{-1}$ up to strains of 0.2, 0.5, 1 and 5.

Figure 35: Optical micrographs of as-worked specimen 1 at 400-0.1-0.2 with deformation bands (Flow curve, Fig 34).

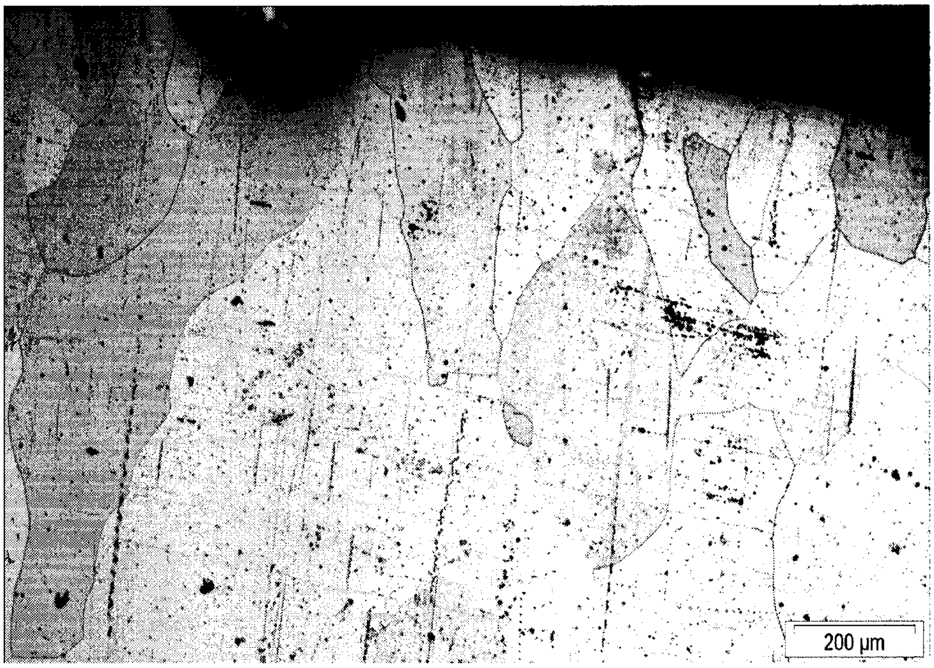

Figure 36: Optical micrographs of as-worked specimen 2 at 400-0.1-0.5

(Flow curve, Fig 34).

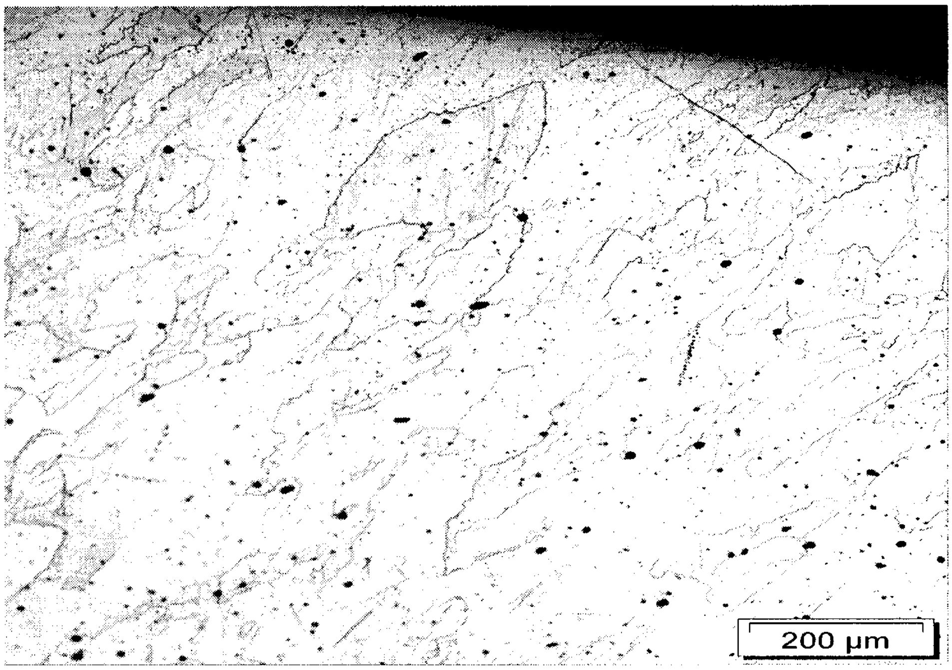

Figure 37: Optical micrographs of as-worked specimen 5 at 400-0.1-0.5-400-0.1-1

(Flow curve, Fig 34).

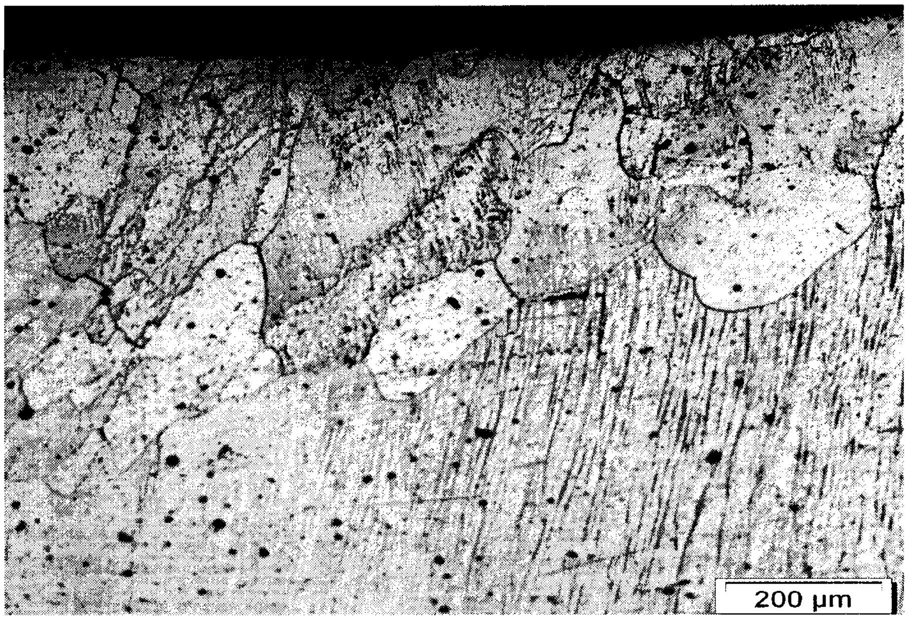

Figure 38: Optical micrographs of as-worked specimen 6 at 400-0.1-0.5-400-0.1-5 with deformation bands and serrated boundaries (Flow curve, Fig 34).

4-1.2. Group II

In this group, there was a strain path change test at 400°C, where specimens 3 and 4 were deformed up to the strain of 0.5 and subsequently deformed backwards to strains of 0.2 and 0 (Table 2). When the flow curves are compared with one another, it is seen both of them have initial strain hardening. In these specimens, the steady state plateau is reached at 27.5MPa at a strain of 0.3 (Fig 39, 40). In the second stage, when deformed in the backward direction to strains of 0.2 and 0. The steady state is established at the same value of 27.5MPa as in the forward direction. The same flow stress values in both directions indicate that there was neglible Bauschinger effect. The occurrence of the same steady state in both directions reveals the occurrence of DRV. The average measured flow stresses from the curves fit with the calculated flow stresses (Tables 3, 4).

In the as-worked condition, specimen 3 revealed elongated grains with serrated GB and presence of deformation bands near the surface (Fig 41). There was considerable presence of equiaxed grains of medium sized in the centre of the specimen. In specimen 4, near some grooves, there were fine grains of smaller size. In the surface, elongated grains of medium size with serrated boundaries were observed (Fig 42). At the centre of the specimen, equiaxed grains of similar size were seen. Hence it can be concluded that during the forward path, grains become elongated with increase in strain. But when strained backwards, the elongated grains mainly become equiaxed in character and appearance.

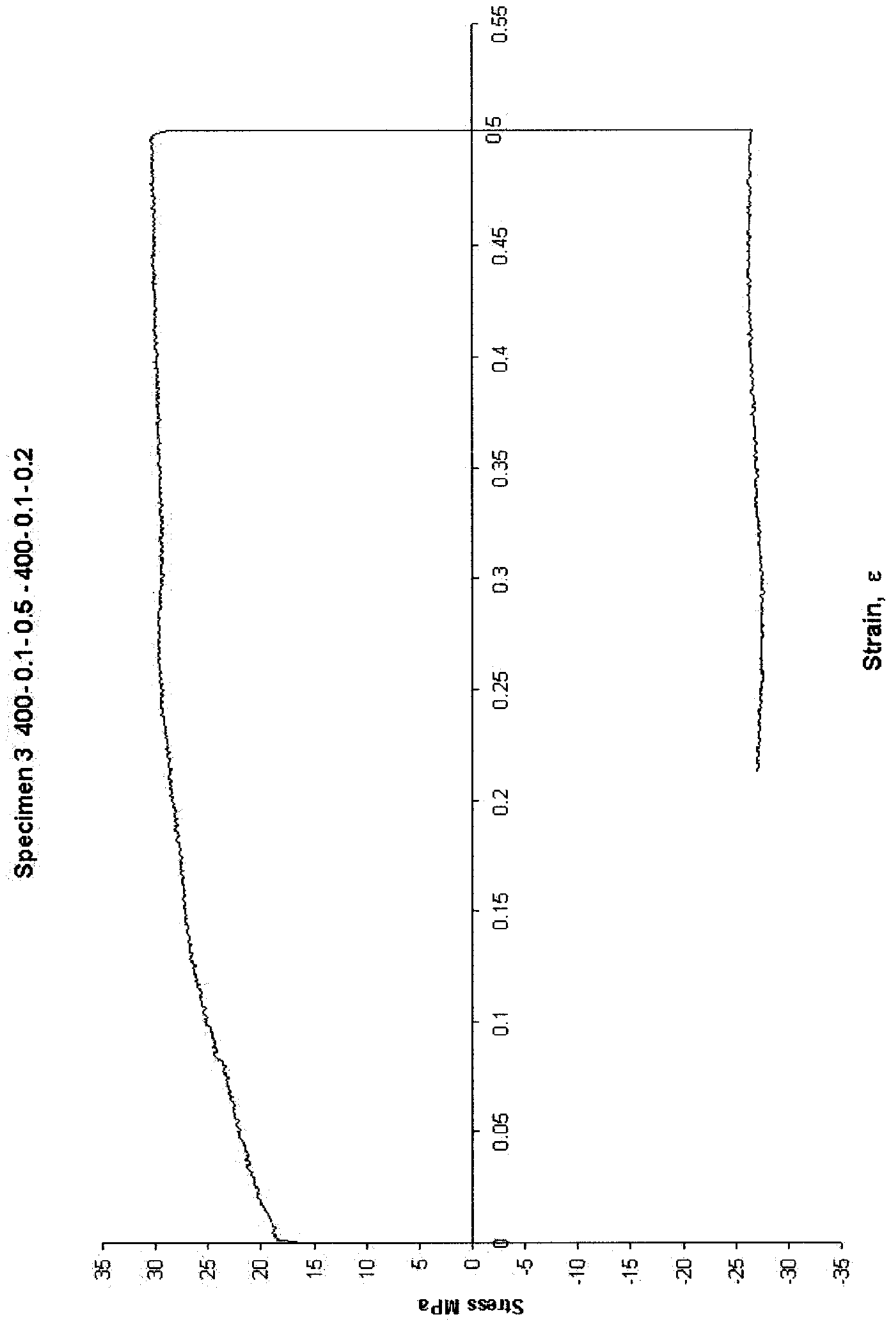

Figure 39 : Flow curve of Al at 400 - 0.1 - 0.5 - 400 - 0.1 - 0.2.

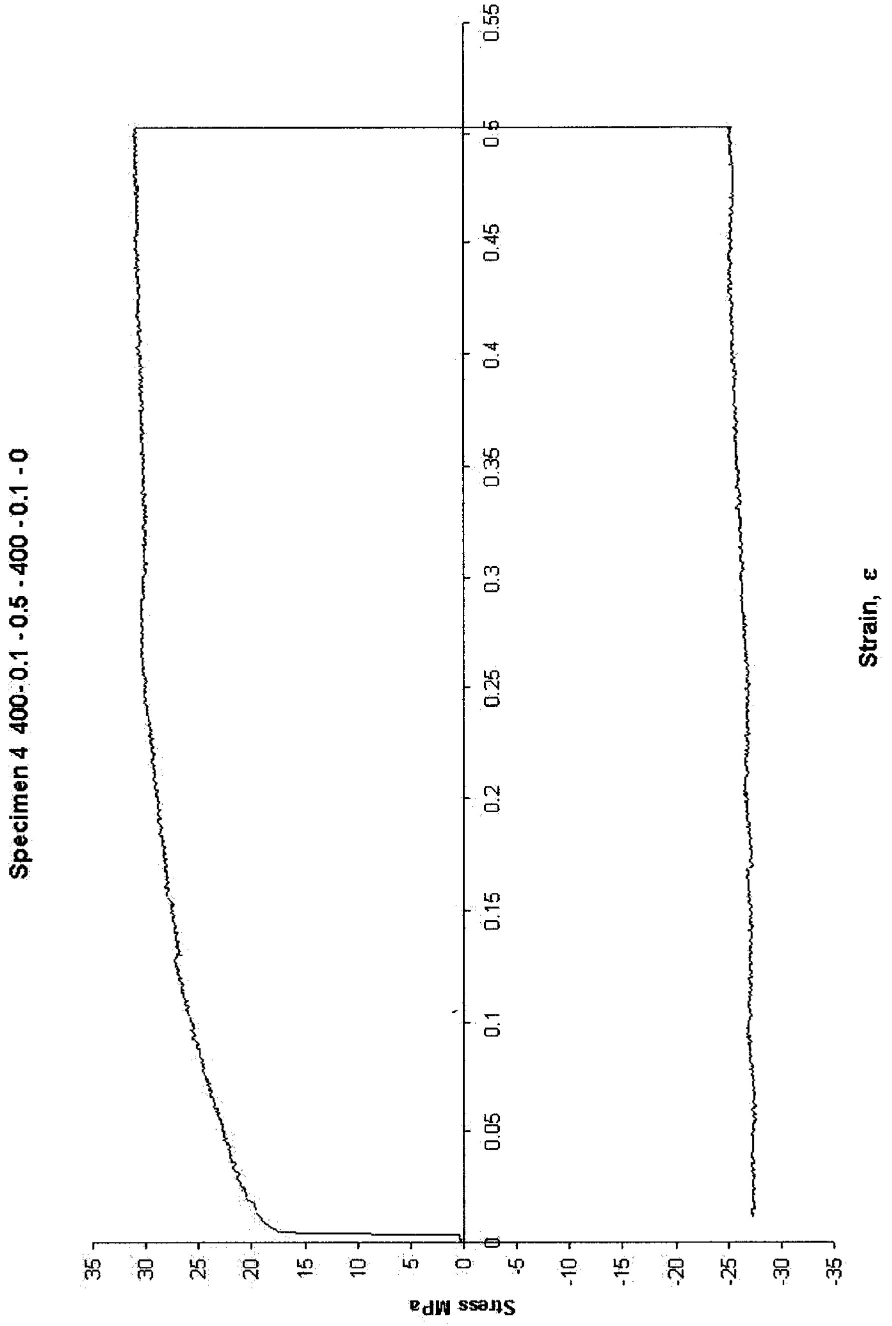

Figure 40: Flow curve of Al at 400 - 0.1 - 0.5 - 400 - 0.1 – 0.

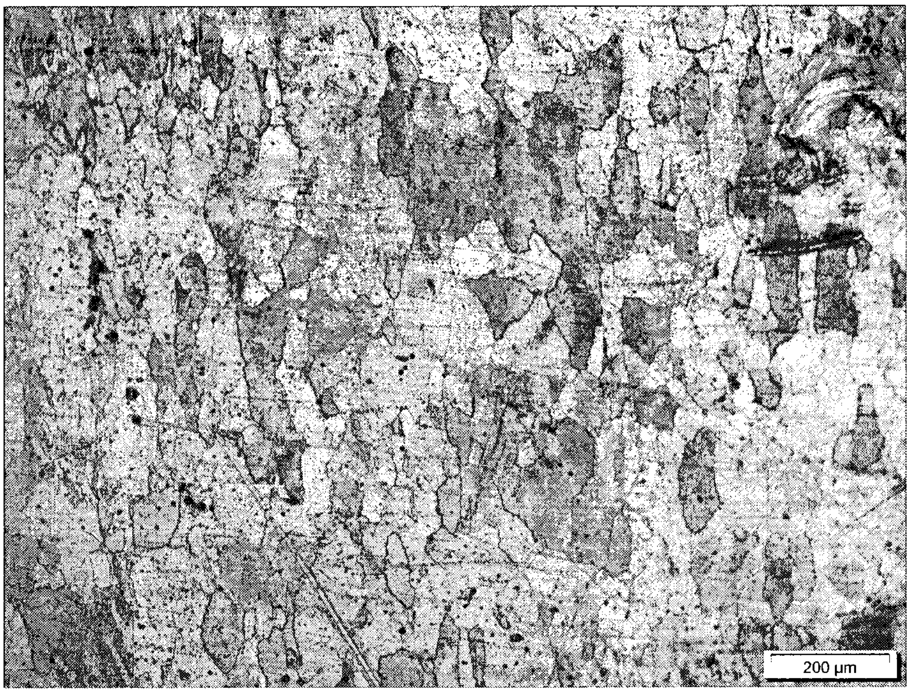

Figure 41: Optical micrographs of as-worked specimen 3 at 400-0.1-0.5-400-0.1-0.2

(Flow curve, Fig 39).

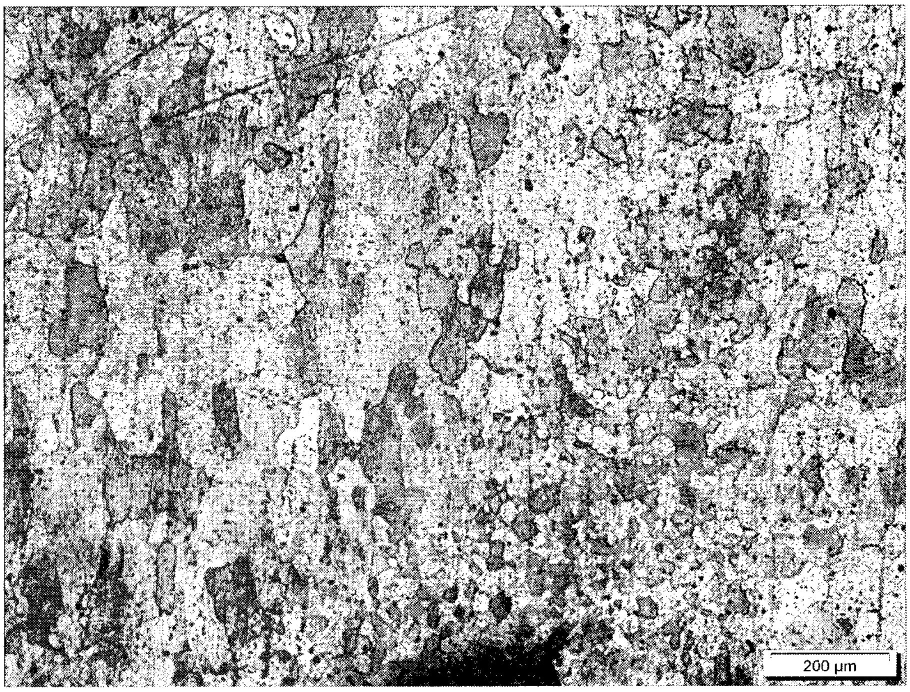

Figure 42: Optical micrographs of as-worked specimen 4 at 400-0.1-0.5-400-0.1-0 with serrated grain boundaries (Flow curve, Fig 40).

4-1.3. Group III

This group consists of strain and strain rate path change test where in the first stage specimens are strained to 0.5 at $0.1s^{-1}$ followed by change in straining to 1, 0.2 and 0 at $0.004s^{-1}$ (Table 2). Initial strain hardening is seen in specimens 7 (Fig 43), 8 (Fig 44) and 9 (Fig 45) to strains of 0.2. Under continued straining, the steady state stress is attained at 27.5MPa at strain of 0.5. In the second stage, specimen 7 is forward strained under $0.004s^{-1}$. A drop in flow stress value was observed from 27.5MPa to 22.5MPa in the forward direction to strain of 1. In the case of specimens 8 and 9 which underwent backward path tests at strain rate of $0.004s^{-1}$, there was slight flow stress decrease before it rises to the steady state value of 22.5MPa was noticed. This drop in steady state flow stress values in the forward and backward paths may be attributed to lower strain rate. All the flow stress values remain the same during the second stage of deformation. The flow stress values gathered from the curves agree with calculated flow stress values (Tables 3, 4). Subgrain sizes increased in size with change to a lower $\dot{\varepsilon}$ (Table 4). This confirms presence of increased DRV in these specimens and neglible Bauschinger effect in the reverse path.

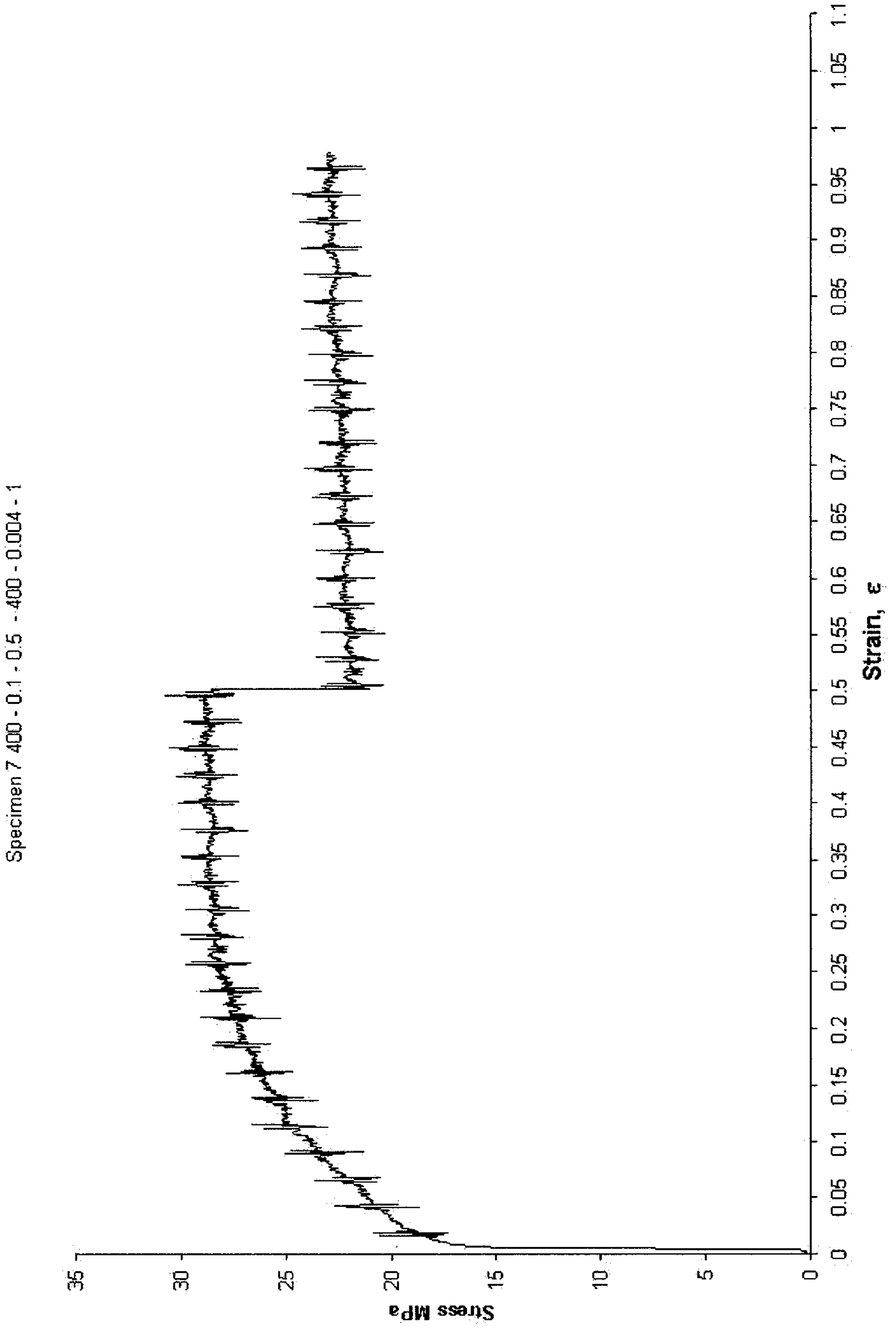

Figure 43: Flow curves of Al deformed at 400-0.1-0.5-400-0.004-1.

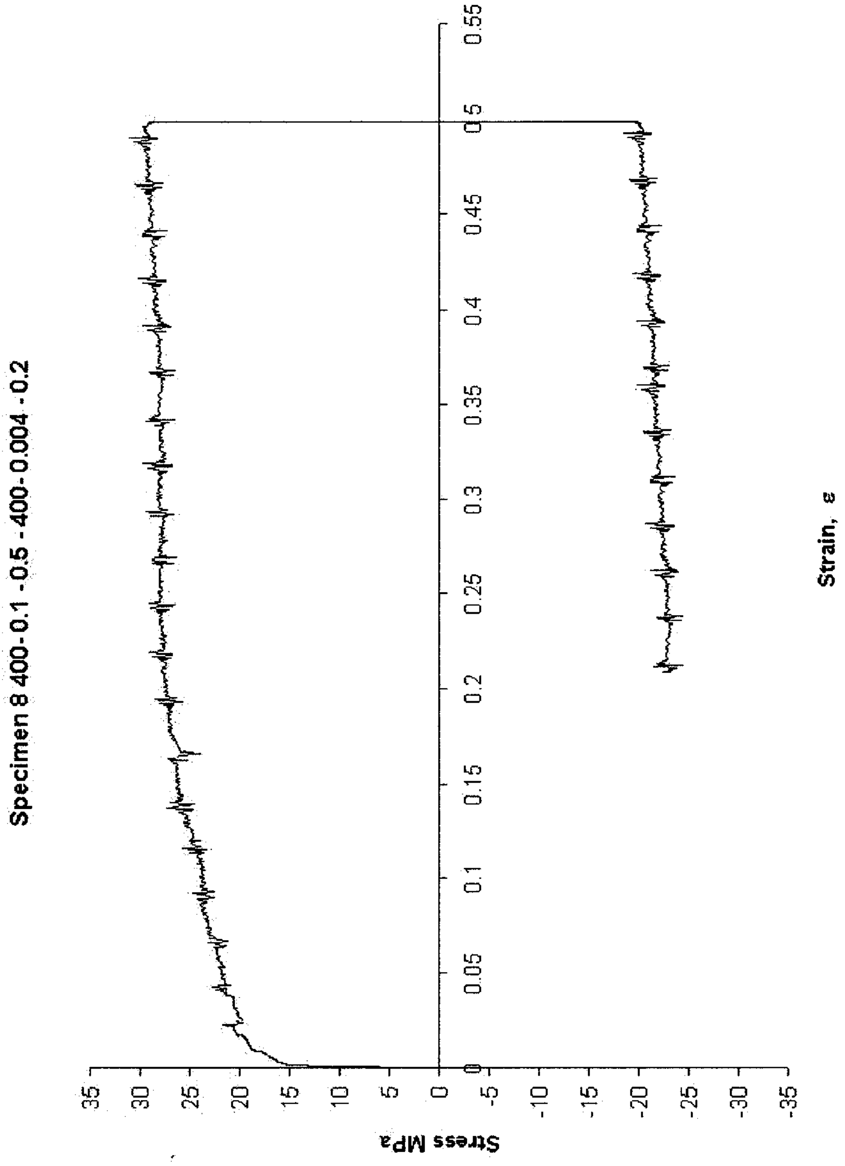

Figure 44: Flow curve of Al deformed at 400 – 0.1 – 0.5 - 400 – 0.004 - 0.2.

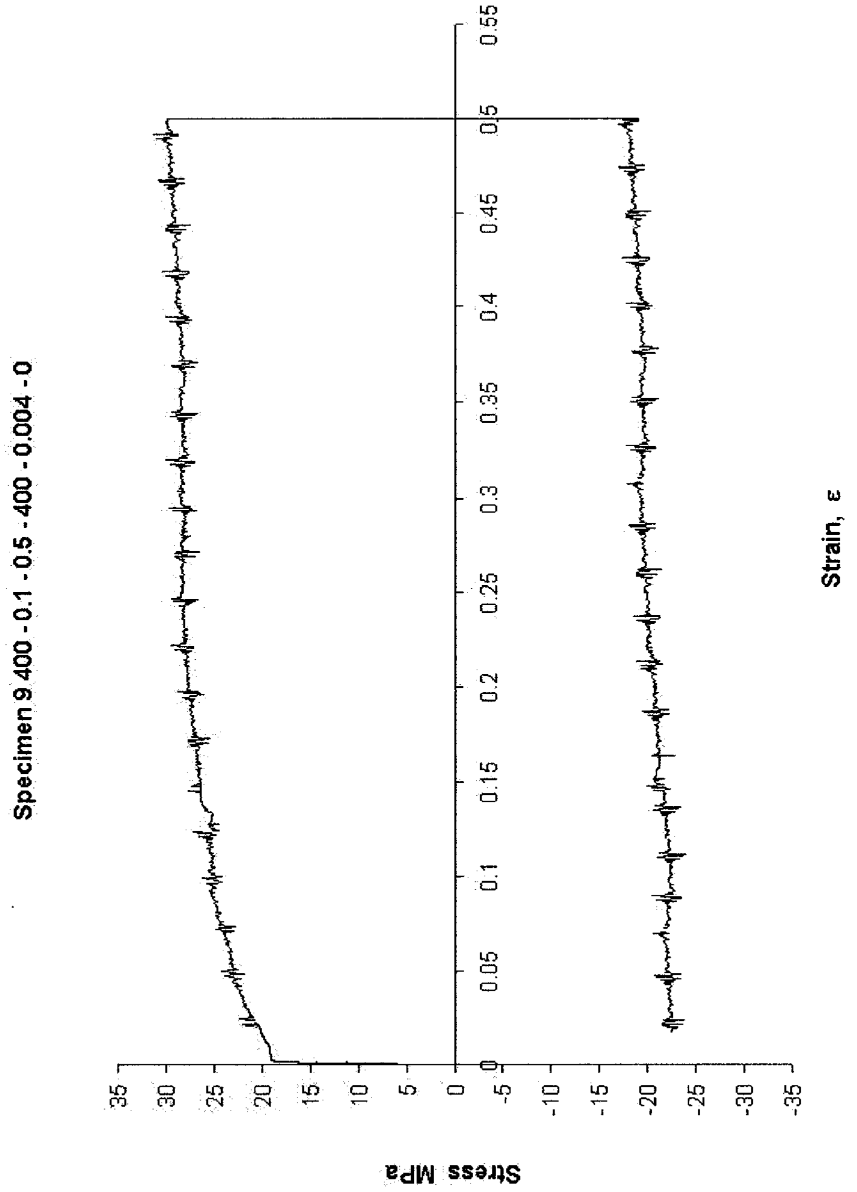

Figure 45: Flow curve of Al deformed at 400 - 0.1 - 0.5 - 400 - 0.004 – 0.

4-1.4. Group IV

Hot working was done on specimens 10 (Fig 46) and 11 (Fig 47) at 400^o- $0.004s^{-1}$ and 500^o- $0.1s^{-1}$ to final strains of 0.5. In specimen 10, the flow curves strain hardens and reach steady state at strain of 0.2. The flow stress observed as this strain is 22.5MPa (Table 2). The flow stress remains the same up to strain of 0.5. In specimen 11, steady state is attained at strain of 0.2 and flow stress value remains at 25MPa, up to a strain of 0.5. The constant flow stress in the respective specimens can be attributed to DRV. A lower flow stress is noticed in specimen 10 which can be attributed to a low strain rate. The average measured flow stress values (Table 3) seem to conform with the calculated flow stress values (Table 4). The calculated logZ values for these specimens are 9.13 and 9.24. The low flow stress values from these specimens indicate the dependence on Z (Eqn 16). It is seen as flow stress reduces, sub grain size increases (Eqn 2, 3, 16) (Tables 3, 4).

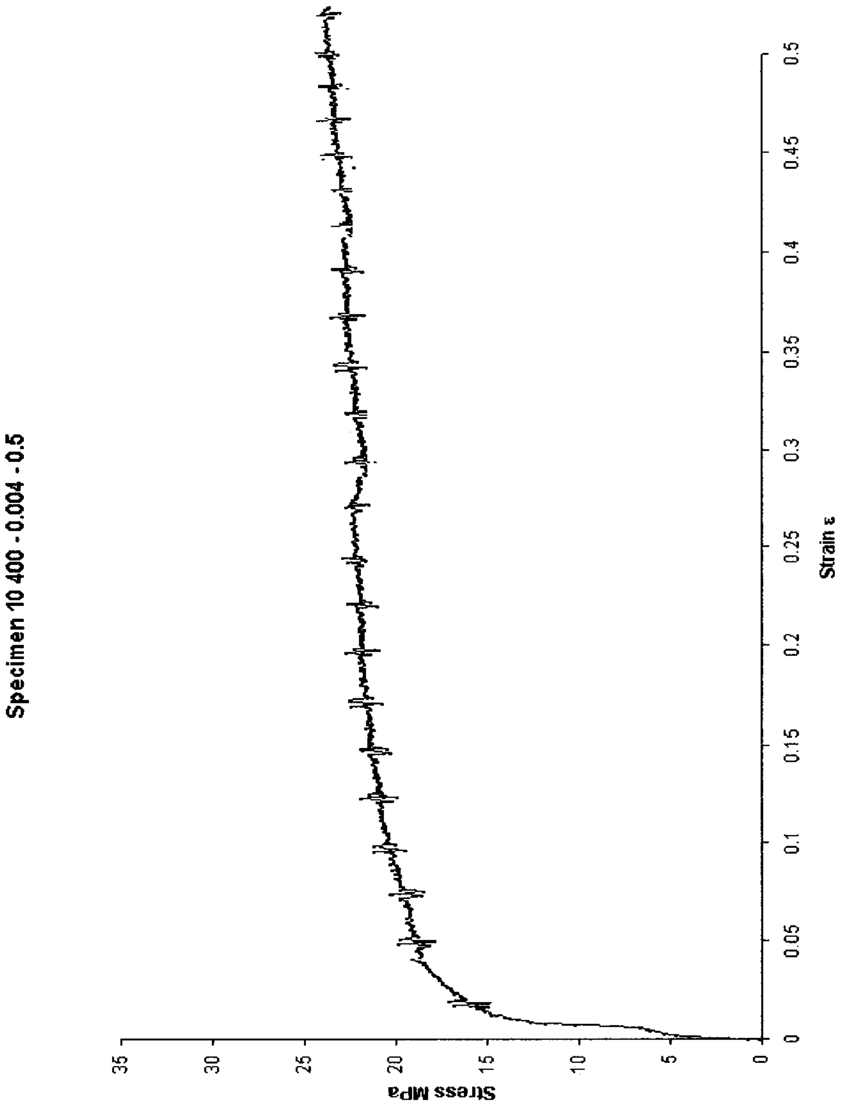

Figure 46: Flow curves of Al under 400 – 0.004 – 0.5.

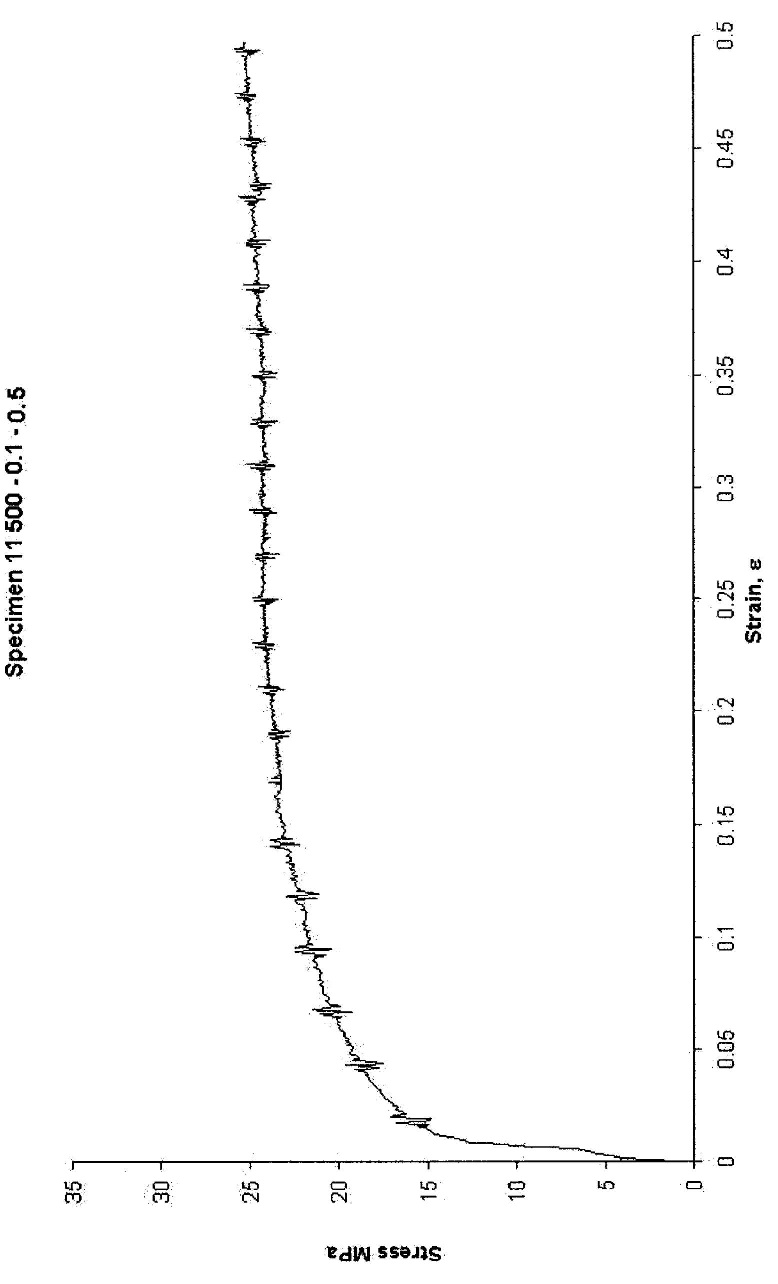

Figure 47: Flow curve of Al under 500 -0.1-0.5.

4-1.5. Group V

Specimens 12, 13 and 14 fall under this group (Table 2). In these two path tests, the first stage tests are performed at 400°C, $0.1s^{-1}$ to strain of 0.5. In the second stage specimen 12 is strained in forward path at 500°C, $0.1s^{-1}$ to 1 whereas specimens 13 and 14 are strained in the backward path to strains of 0.2 and 0 respectively (Fig 48, 49). In the first stage, all the flow curves strain harden and reach steady state at strains of 0.2. The flow stress observed at strain of 0.5 was 27.5MPa. In the second stage in the forward direction, there is significant difference in the flow stress value of specimen 12 from 27.5 to 25MPa. This drop is attributed to higher T. In the backward direction for both specimens 13 and 14, the flow stress value drops to 25MPa to strains of 0.2 and 0 respectively. These indicate occurrence of DRV at same level during the forward and backward secondary straining path. Hence it can concluded that the second stage flow stress values are lower because of higher T and that there is neglible Bauschinger effect. By comparing logZ values in the initial forward and secondary backward path, it can be inferred that during the secondary path subgrain sizes increase due to lower logZ value.

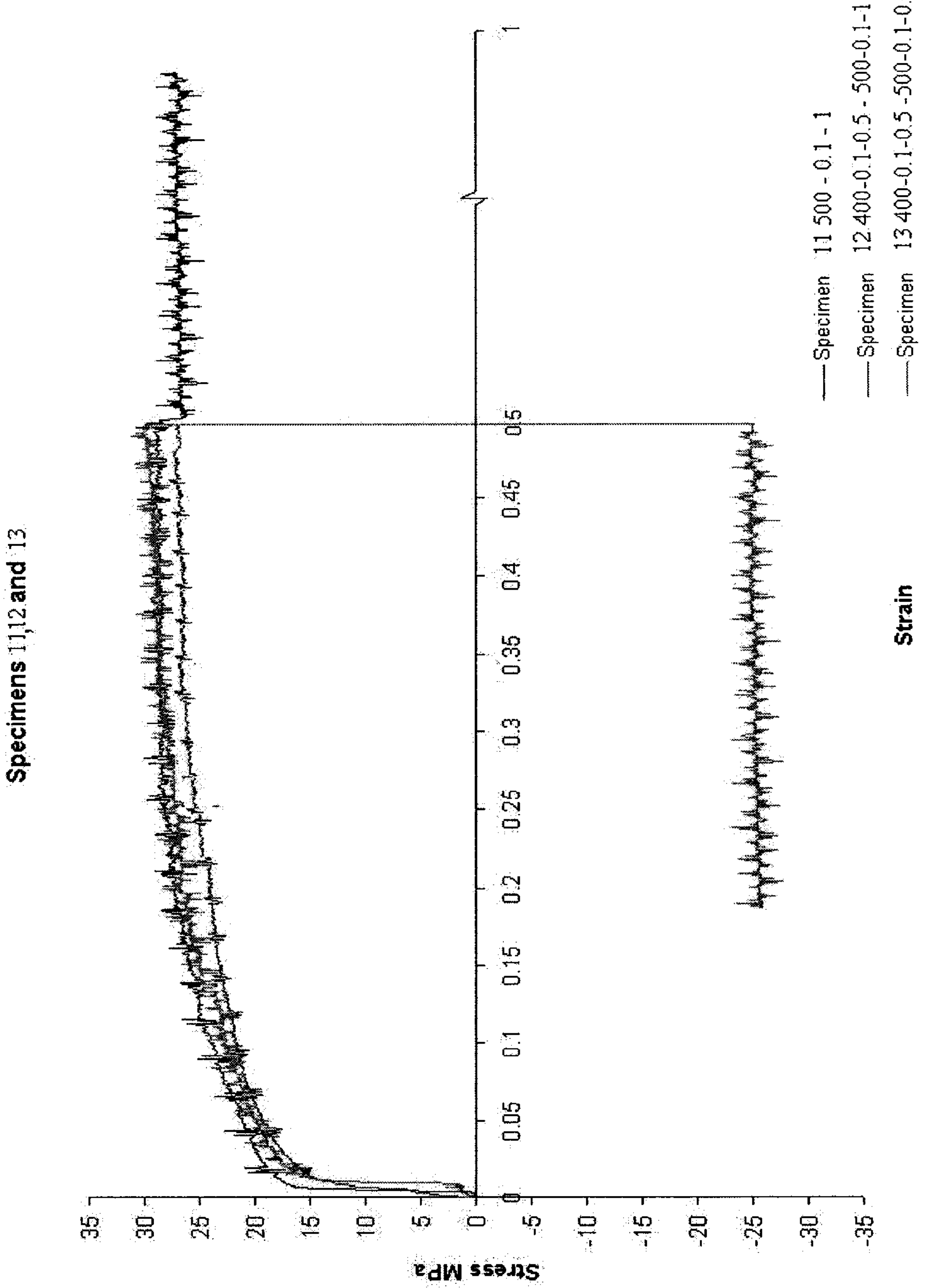

Figure 48: Flow curves of specimens 11, 12 and 13.

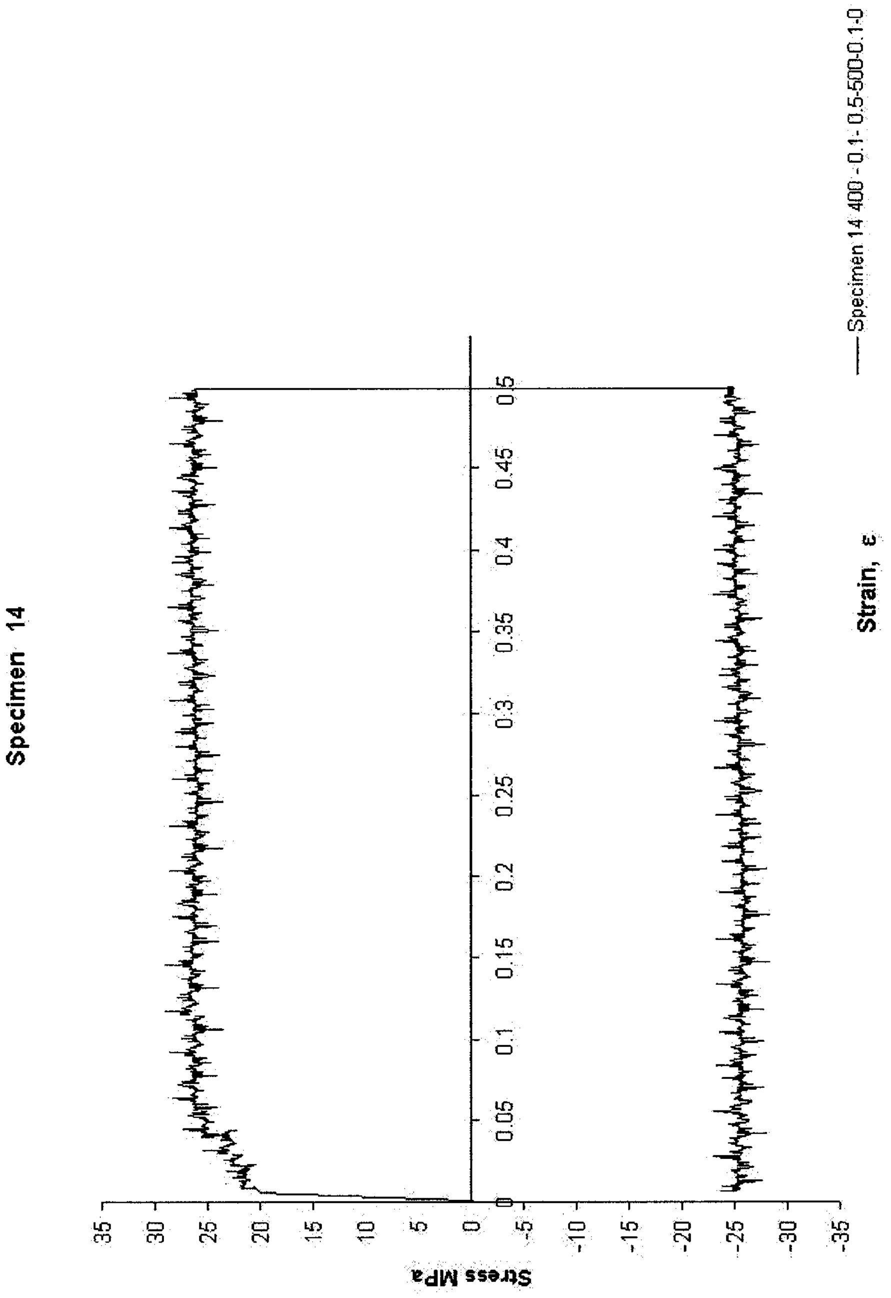

Figure 49: Flow curve of Al deformed at 400-0.1-0.5-500-0.1-0.

Now the specimens with similar test conditions either in the forward or backward direction are compared with each other along with their calculated flow stress values.

In initial tests at 400°C, $0.1s^{-1}$ to strains of 0.5 , all the specimens (specimens 2-9, 12-14) strain hardened to a plateau near 27.5MPa (except specimen 2). When the test was extended to higher strain (specimen 5,6) of 1 or 5, the flow stress remained the same; similarly when direction was reversed (specimens 3,4), the flow stress was also about 27.5MPa. When compared with calculated flow stress value, the average measured flow stress was 2.19MPa less (Table3, 4).

In cases when the second stage was changed to 400°C, $0.004s^{-1}$ (specimens 7,8,9), the flow stress values in forward or reverse direction were similar to those under that condition in the first stage (specimen 10) (Table 2). The average measured flow stresses were established at 22.5MPa at strain of 0.5 in all these specimens. When compared with the calculated flow stress (Table 4), the average measured flow stress for this condition fall short by 0.32MPa (Table3).

Under test conditions of 400°, $0.1s^{-1}$ or 500°C, $0.1s^{-1}$ (specimen 12,13,14), the flow stresses in the forward or reverse direction remained the same as those under that condition in the first stage (specimen 11). The average measured flow stresses for 500°C, $0.1s^{-1}$ was 25MPa; thus more than the calculated flow stress by 3.36MPa (Table 3).

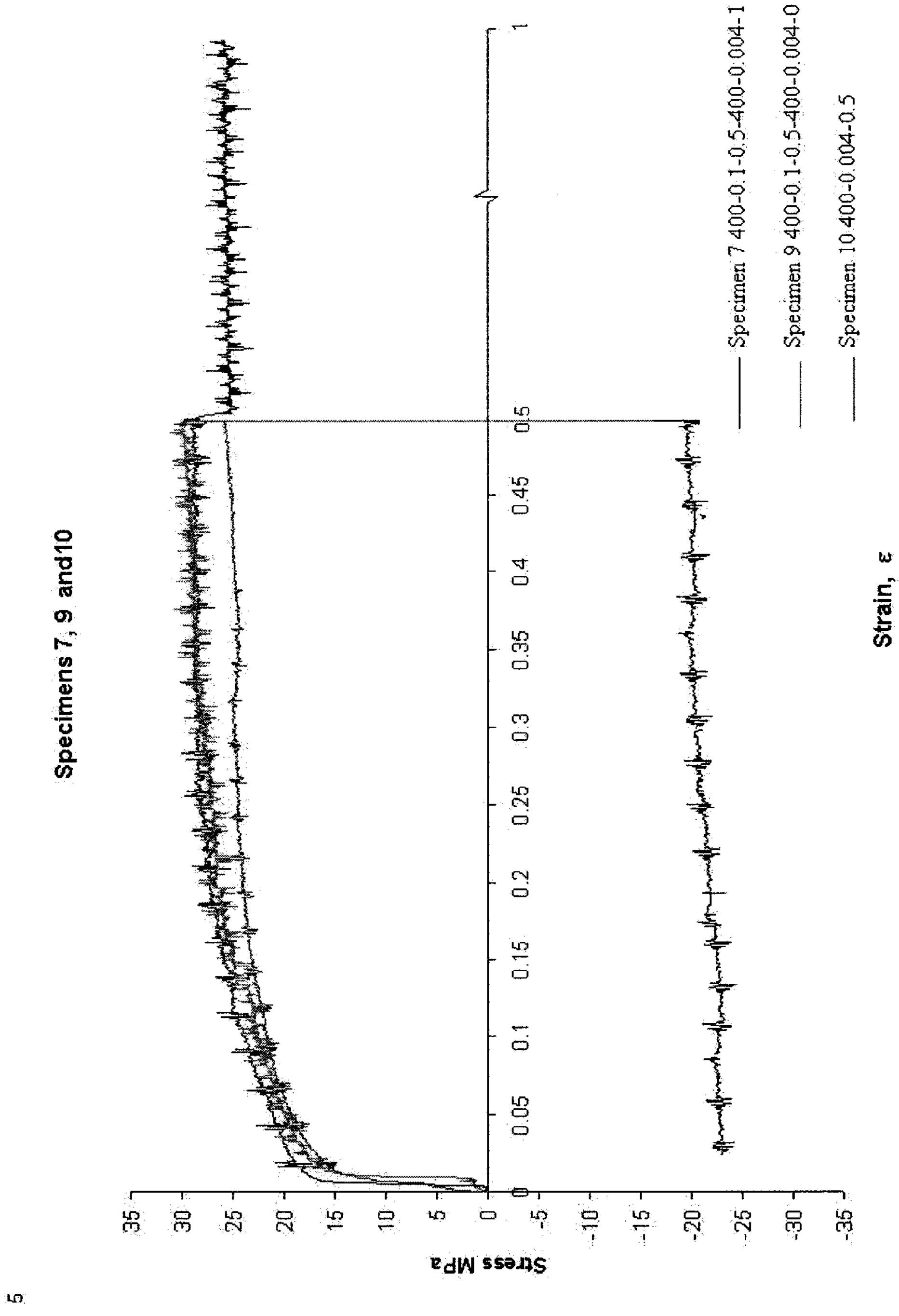

Figure 50: Flow curves of specimens 7, 9 and 10.

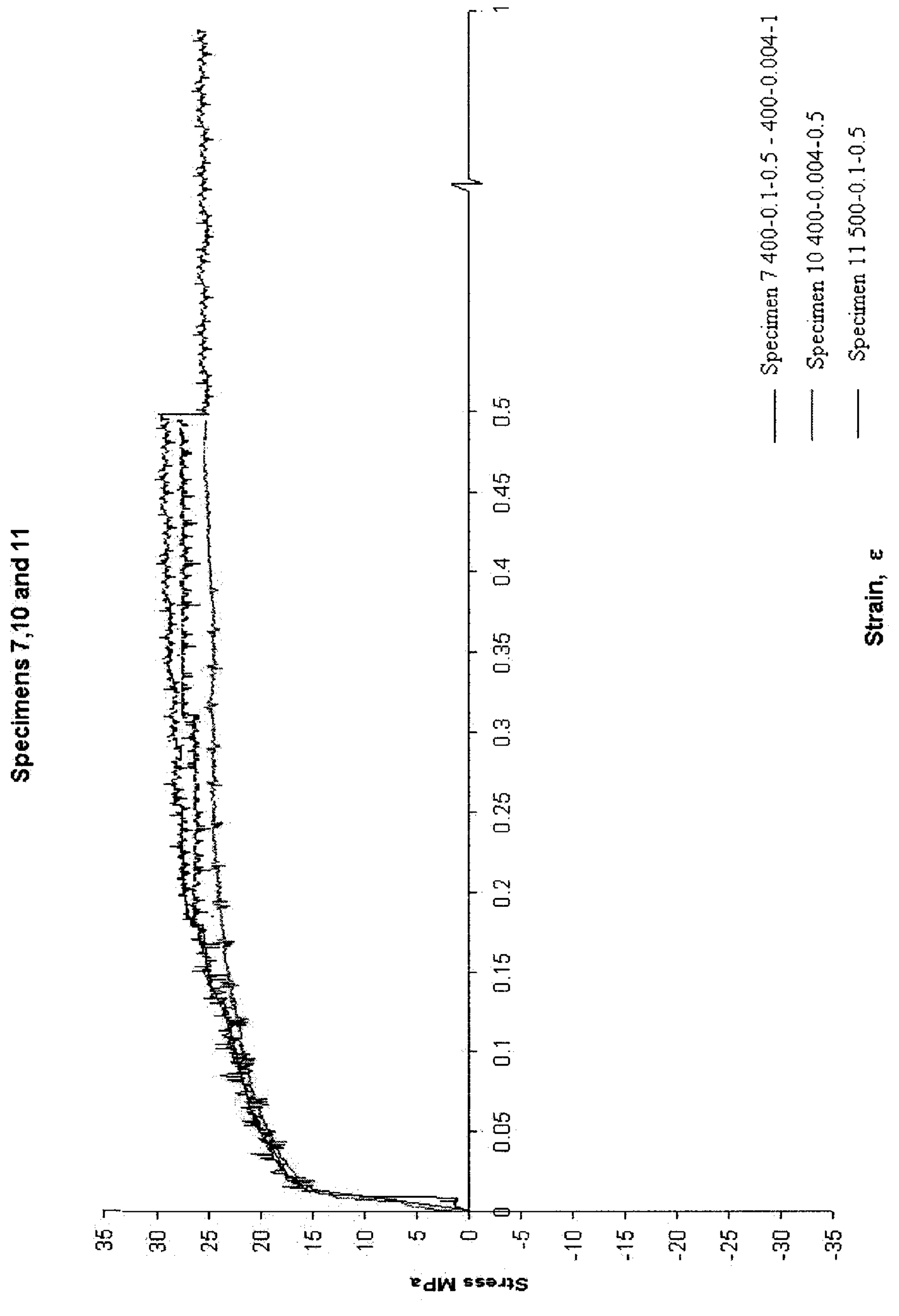

Figure 51: Flow curves of specimens 7, 10 and 11.

4-2. ORIENTATION IMAGING & POLARIZED OPTICAL MICROSOPY

Through collaboration with Dr G.A Cingara in Materials Science at University of Toronto some duplicate as-deformed specimens (indicated by D) were observed by polarized optical microscopy (POM) after anodizing and also by orientation imaging microscopy (OIM). The specimens are named as follows 1D (400-0.1-0.2), 2D (400-0.1-0.5), 3D (400-0.1-0.5-400-0.1-0.2), 4D (400-0.1-0.5-400-0.1-0), 5D (400-0.1-0.5-400-0.1-1) and 6D (400-0.1-0.5-400-0.1-5).

In the macrographs showing almost the whole gage section, grain alignments of specimens which were strained in the forward path are observed (Fig 52). In specimen 1D, very large grains are seen with deformation bands. Near the surface, a mixture of large and fine grains is observed which conforms with Fig 35. There is very little visible grain alignment due to low strain (Fig 52a). Specimen 2D shows alignment of grains inclined at about 30° to torsion axis. Evidence of elongation and presence of fine grains are seen near the surfaces. Fig 36 shows a mixture of equiaxed and elongated grains near the surfaces. In specimen 5D, increased alignment of fine grains is noticed due to high strain. Grain elongation is at 60° to the torsion axis (Fig 52c). In the right half side, there is presence of large grains. These features agree with optical results in Fig 37. Differences in the macrographs were seen due to different grain sizes.

Specimens 3D and 4D were strained backwards from 0.5 to strains of 0.2 and 0 (Fig 53). In specimen 3D, fine grains with alignment were observed. The alignment has decreased from about 30° to about 15° as the specimen underwent backward straining. In Fig 41, mixture of elongated and equiaxed grains with serrated GB were seen. Alignment of fine grains is seen in specimen 4D inclined at 5° to the torsion axis (Fig 53b). Some similarities like presence of fine grains near some grooves were observed in Fig 42 also.

At higher magnifications, specimen 1D reveals strong presence of deformation bands surrounded by large and fine grains (Fig 54a). Whereas in specimen 2D, elongated grains with less distinct deformation bands were observed (Fig 54b). Specimen 5D reveals elongated grains with serrated grain boundaries. There is increased alignment of grains at 60° to the torsion axis along with deformation bands (Fig 55).

Specimen 3D reveals fairly equiaxed and fine grains with no evidence of deformation bands (Fig 56a). It is impossible to compare 1D and 3D because of great differences in grain sizes. The observed features agree with Fig 41. In specimen 4D, a mixture of equiaxed and elongated grains with serrated GB is seen (Fig 56b). Subgrains with equiaxed appearance are also seen and there is very little presence of deformation bands. The above features are similar to Fig 42.

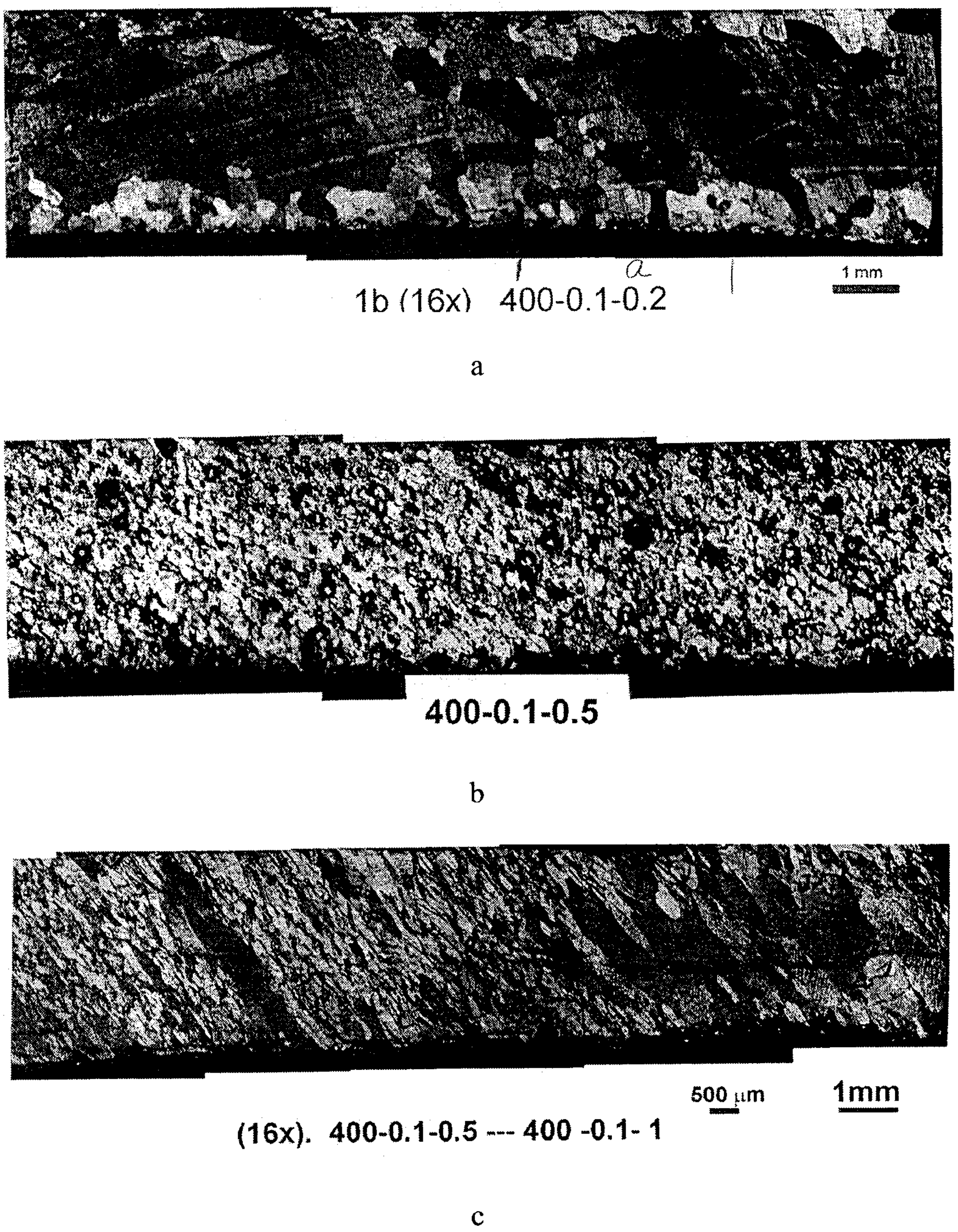

Figure 52: Polarized optical macrographs of as-worked specimens 1D,2D and 5D in forward path: a) 400-0.1-0.2, b) 400-0.1-0.5 and c)400-0.1-0.5 – 400-0.1-1, same magnification (courtesy of Dr G.A Cingara) (optical micrographs of specimens 1,2 and 5, Fig 35, 36 and 37) [62].

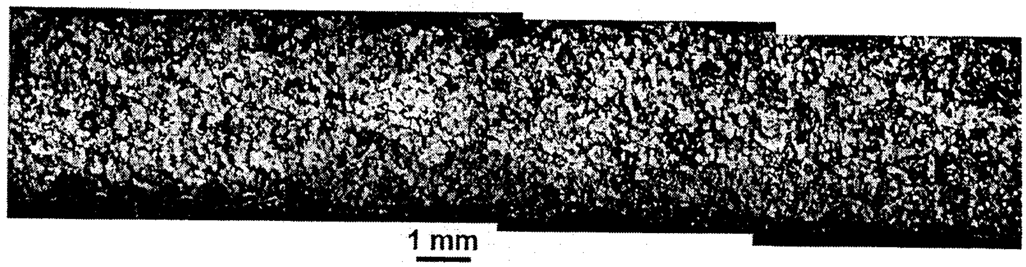

3b (16x). 400-0.1-0.5 ---- 400-0.1-0.2

a

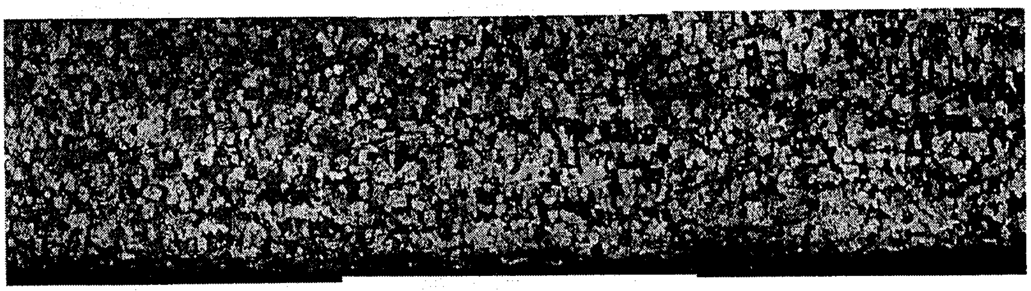

400-0.1-0.5 --- 400-0.1- 0

b

Figure 53: Polarized optical macrographs of as-worked specimens 3 and 4 in reverse path: a) 400-0.1-0.5 - 400-0.1-0.2 and b) 400-0.1-0.5 – 400-0.1-0, same magnification (optical micrographs specimens 3 and 4, Fig 41 and 42) (courtesy of Dr G.A Cingara)[62].

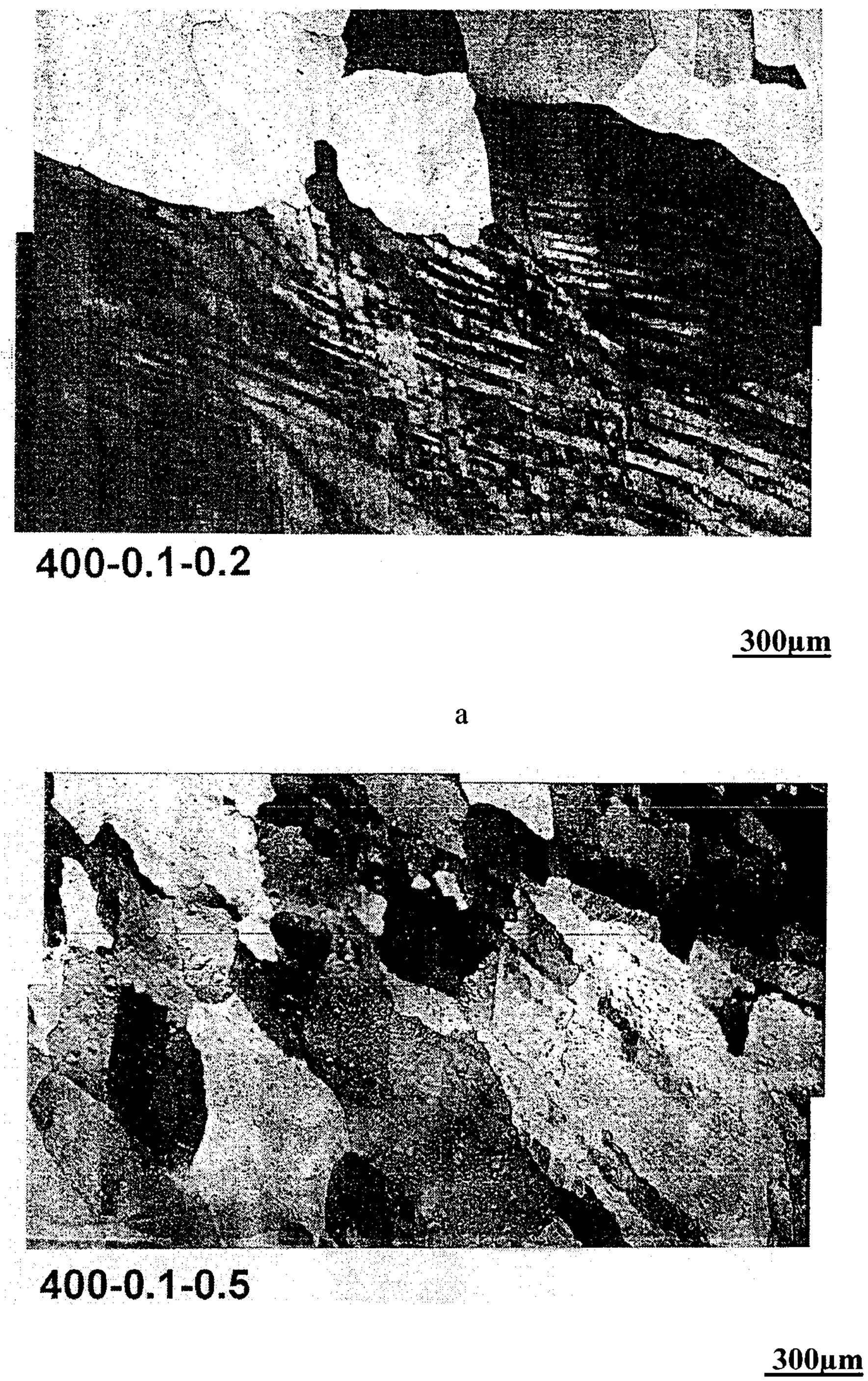

Figure 54: Polarized optical micrographs of specimens: a) 1D hot worked at 400-0.1-0.2 and b) 2D hot worked at 400-0.1-0.5 (macrographs given in Fig 52) (courtesy of Dr G.A Cingara) [62].

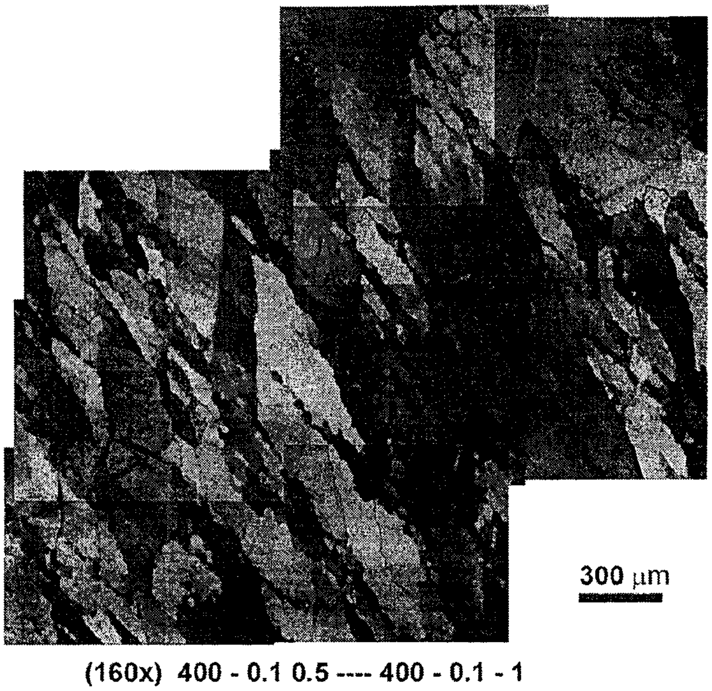

Figure 55: Polarized optical micrographs of specimen 5D hot worked at 400-0.1-0.5-400-0.1-1 (The microstructure of this specimen is more clearly presented in OIM micrograph Fig 58) (courtesy of Dr G.A Cingara) [62].

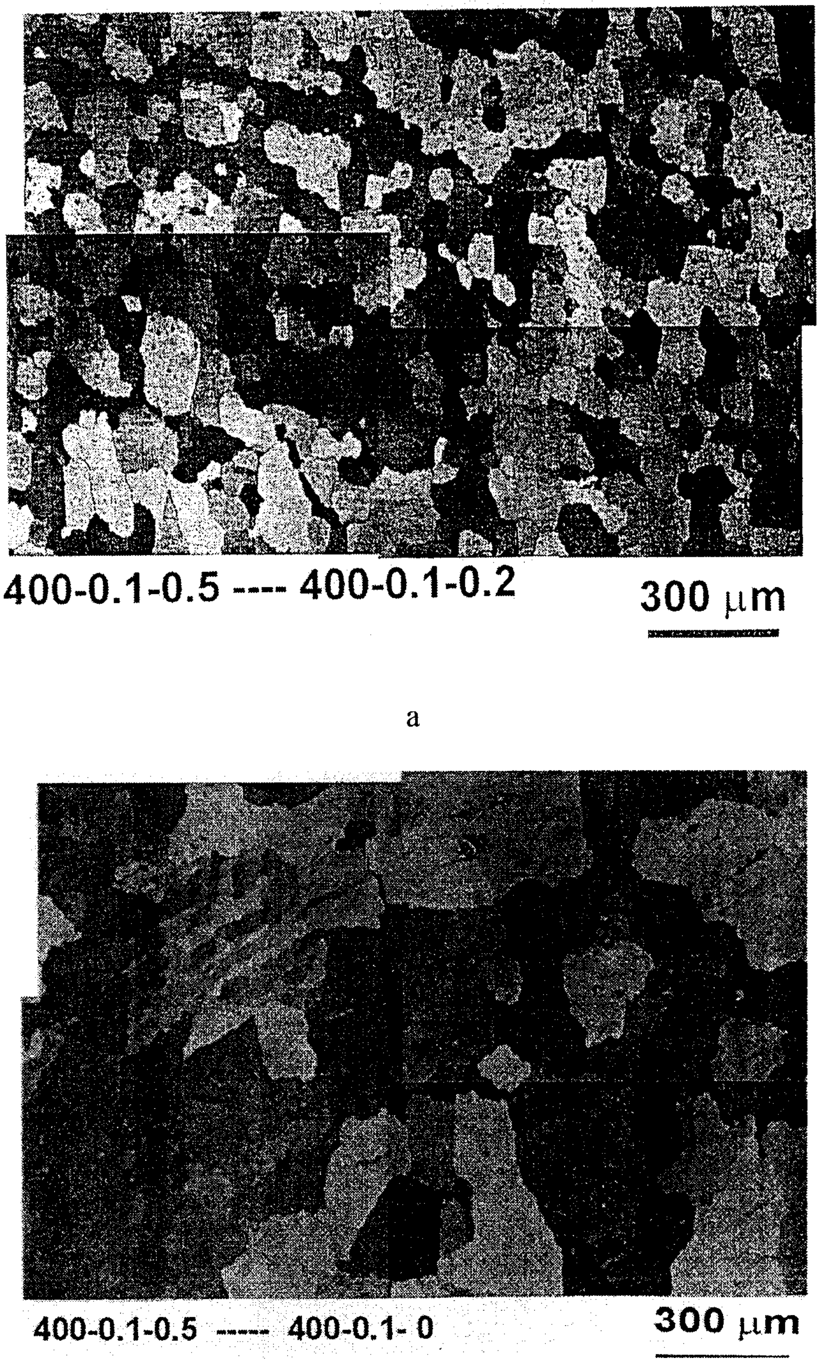

a

b

Figure 56: Polarized optical micrographs of specimens: a) 3D hot worked at 400-0.1-0.5-400-0.1-0.2 b) 4D hot worked at 400-0.1-0.5-400-0.1-0 (macrographs given in Fig 53) (courtesy of Dr G.A Cingara) [62].

Using OIM, the influence of strain and strain rate on misorientations (θ) is examined. In the OIM specimens, the torsion axis may be at any angle yet parallel to the surface. In as-worked specimen 2D, elongated grains were observed. Inside the elongated grains, subgrains of low angle (LAB) are formed (Fig 57). Deformation bands with medium angle boundaries (MAB) are formed at an angle to elongation direction they are less distinct. Since sub-boundaries less than 2° are frequently omitted only ~50% of sub-boundaries are exhibited. In specimen 5D with advancing strain from 0.5 to 1, grains are much more elongated compared to specimen 2D. With further deformation MAB start to align near at 45° inclined to the direction of elongation inside grains with high angle boundaries (HAB). Deformation bands of medium θ are emphasized and subgrains are slightly visible (Fig 58). At higher strains of 5 in specimen 6D grains are severely broken up because the deformation bands have rotated so much that the elongated grains are not clearly visible (Fig59). Many SGB are omitted due to low angles. The boundaries exhibited are a mixture of GB and deformation band boundaries. Hence it can be inferred that the fraction of HAB increases with increasing strain (Table 5).

During the forward path to 0.5 in Specimens 3D and 4D, equiaxed subgrains with LAB were seen inside elongated grains. Only some 50% of sub-boundaries were observed. When subgrains are entirely inside grains they are surrounded by low angle facets; OIM counts them as LAB. As more subgrain touch grain boundaries, they are counted as HAB. Therefore, number of HAB's increase relative to LAB's, whereas volume of grains stays constant.

Under reversing strain direction for specimens 3D and 4D, as less sub-boundaries of equiaxed character touch GB fraction of LAB increases. Subgrains remain equiaxed because of constant rearrangement and density of dislocations. The misorientation of subgrains is controlled on density and misorientation of dislocations inside the subgrains. Whereas TB and DB increase in misorientation with increase in strain. Hence grains change from elongated back to equiaxed (Fig 60,61). For all test conditions, the proportion of MAB decreases with forward strain and increases with backward strain. From these results, one comes to conclusion in DRV; subgrains of low angle is maintained in the forward and backwards paths. With increasing strain in the forward direction, the GB overtakes the SGB.

Table 5: Misorientation statistics for OIM boundaries in % after straining at 400°C, $0.1 s^{-1}$ (courtesy of Dr G.A Cingara) [62].

Specimen No	Strain	1^o-5^o LAB	5^o-10^o MAB	$>15^o$ HAB
1D	0.2	63.2	0.3	36.5
2D	0.5	51.6	4.5	43.9
5D	1	51.2	8.1	40.7
3D	0.5 to 0.2	60.7	4.6	31.5
4D	0.5 to 0	64.7	3.8	34.7

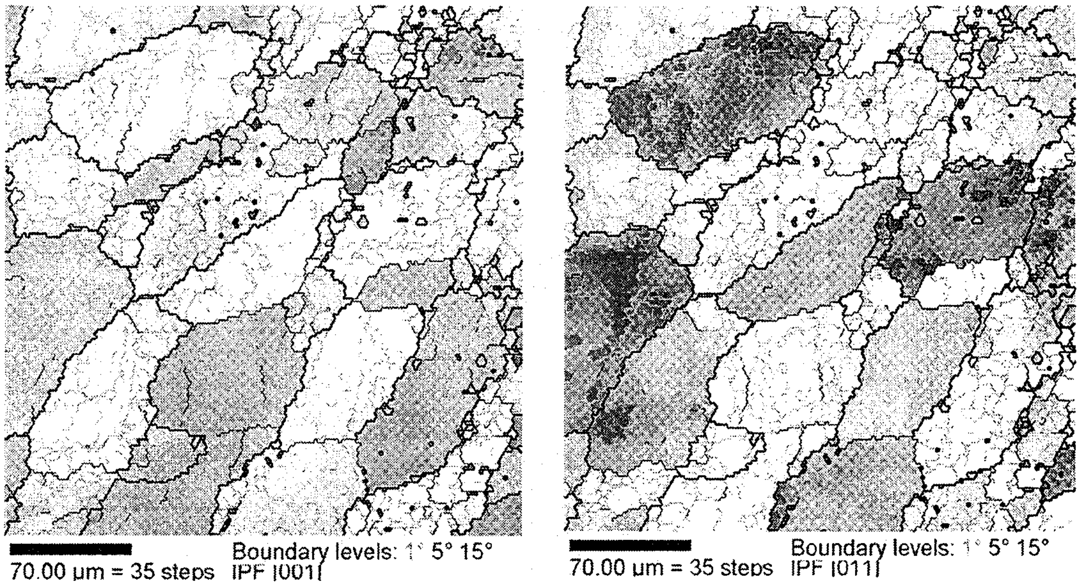

Figure 57: Orientation imaging microscopy of specimen 2D deformed at 400-0.1-0.5 (Fig 54) (courtesy of Dr G.A Cingara) [62].

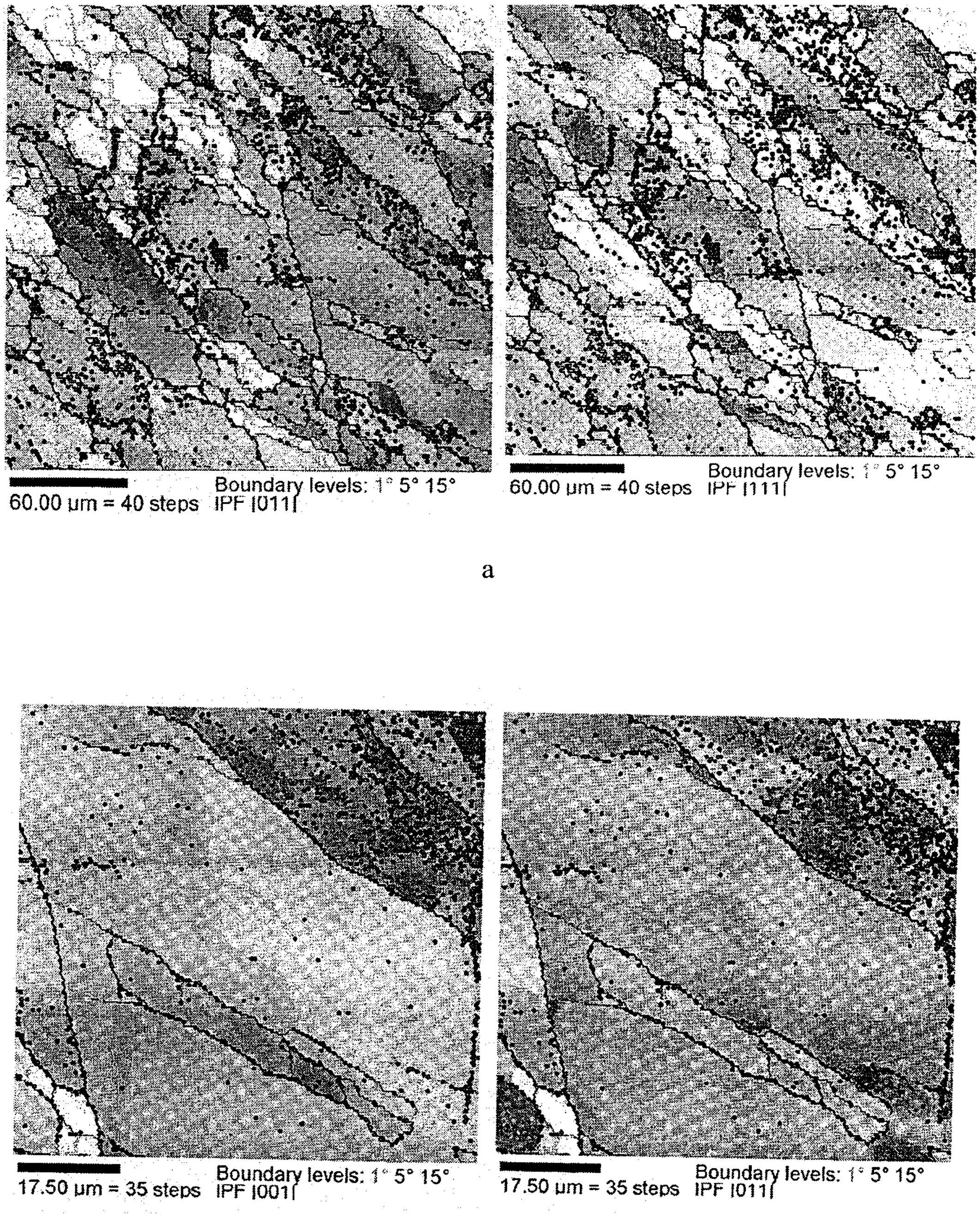

b

Figure 58: Orientation imaging microscopy of specimen 5D deformed at 400-0.1-0.5 – 400-0.1-1 a) lower magnification b) higher magnification (Fig 55) (courtesy of Dr G.A Cingara)[62].

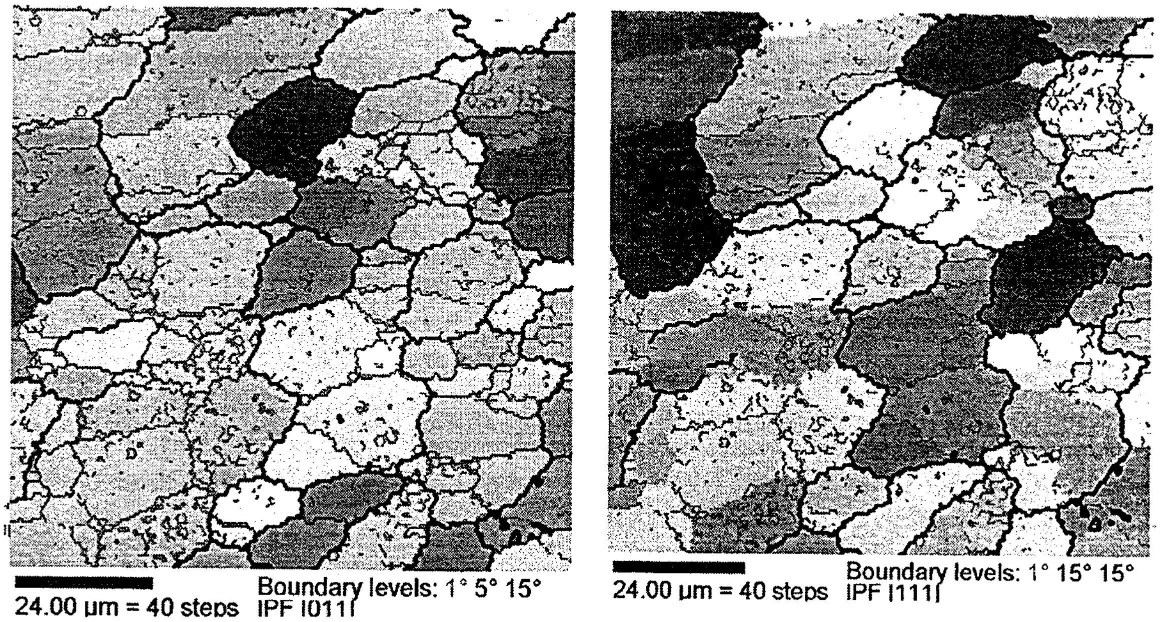

Figure 59: Orientation imaging microscopy of specimen 6D deformed at 400-0.1-0.5 – 400-0.1-5(courtesy of Dr G.A Cingara) [62].

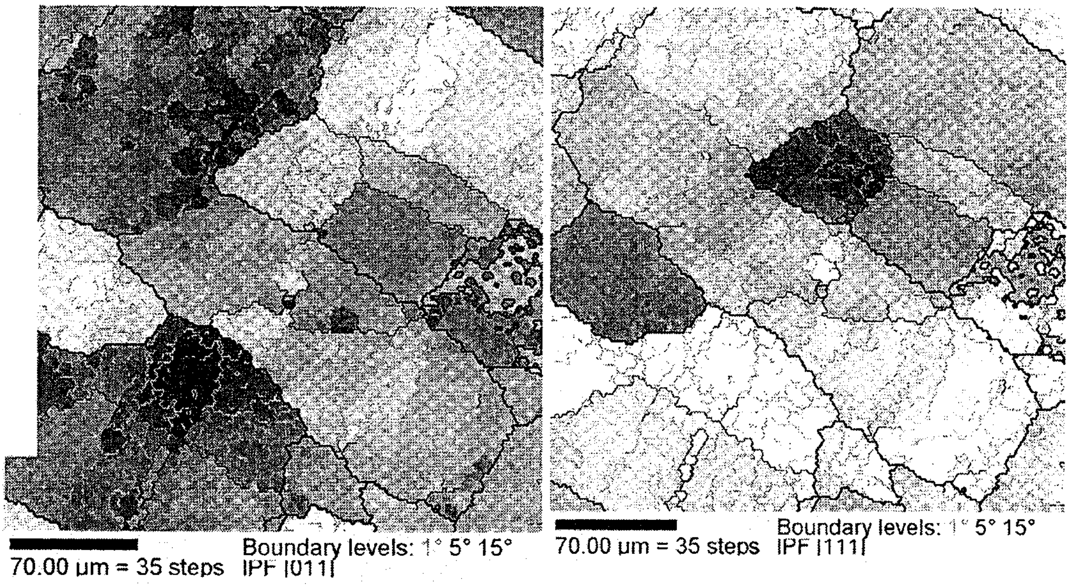

Figure 60: Orientation imaging microscopy of specimen 3D deformed at 400-0.1-0.5 – 400-0.1-0.2 (Fig 56) (courtesy of Dr G.A Cingara) [62].

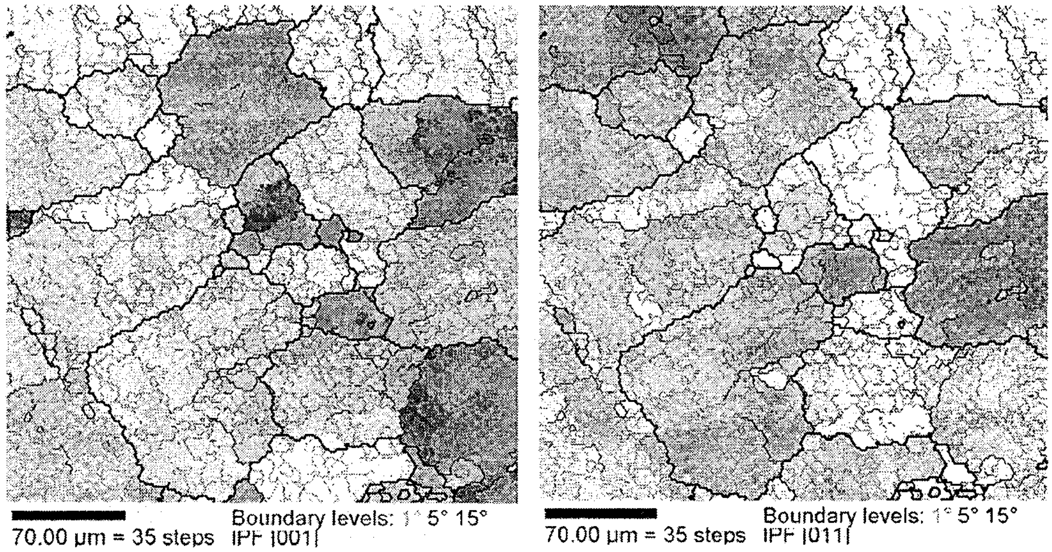

Figure 61: Orientation imaging microscopy of specimen 4D deformed at 400-0.1-0.5 – 400-0.1-0 (Fig 56) (courtesy of Dr G.A Cingara) [62].

4-3. EXAMINATION OF ANNEALED SPECIMENS

4-3.1. Optical Micrographs of Annealed specimens

Group I and II specimens were annealed in the furnace at equal logarithmic intervals to detect the first occurrence of SRX. The specimens were immediately quenched in water after annealing to retain the microstructure. It was not possible to trace the first occurrence of SRX.

When specimen 1 was annealed for 450s, near the surfaces there was no evidence of strain but in the middle there is large grain with boundaries curving into it; this indicates that surrounding grains are growing into the large grain (Fig 62). At 450s a small fraction of recrystallized grains was observed. When annealing time was increased to 600s, there are still some long axial grains in centre with evidence of strain markings; these did not have enough energy to cause SRX. In most of the specimens, there were grains of medium size that looked recrystallized (Fig 62, 63).

Specimen 2 was annealed for 300s, there were medium sized grains with more mixed sizes near the surfaces. There is evidence of deformation bands (Fig 64). Thus the specimen is not fully SRX. When annealed for 500s, it is seen that specimen looks completely SRX. However in the centre, there are few deformed grains. Near the surfaces there is evidence of fine grains (Fig 64, 65).

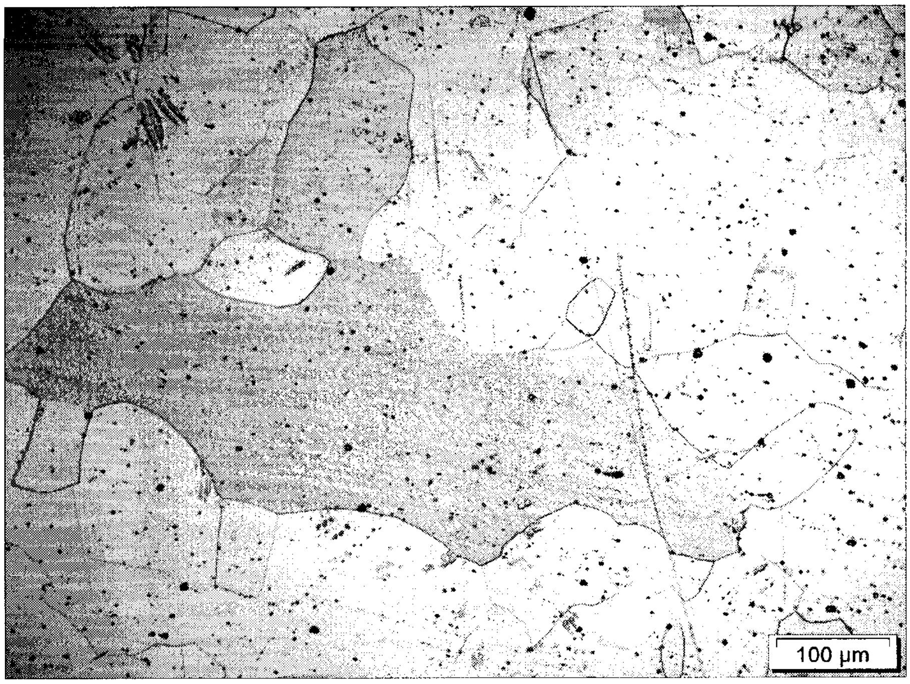

a

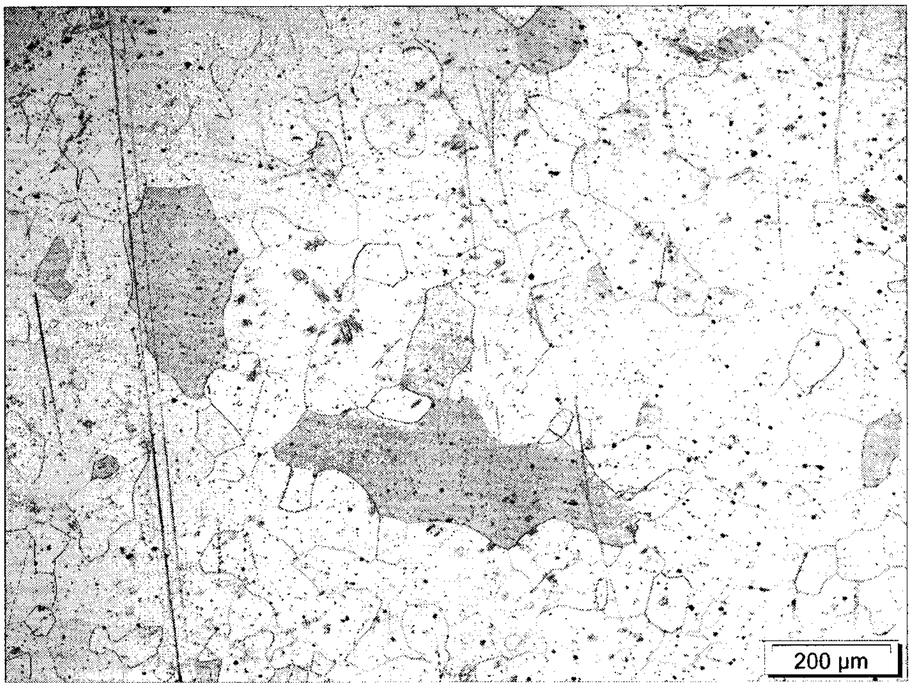

b

Figure 62: Optical micrographs of specimen 1 (400-0.1-0.2) annealed for 450s a) higher magnification b) lower magnification (as-worked, Fig 35).

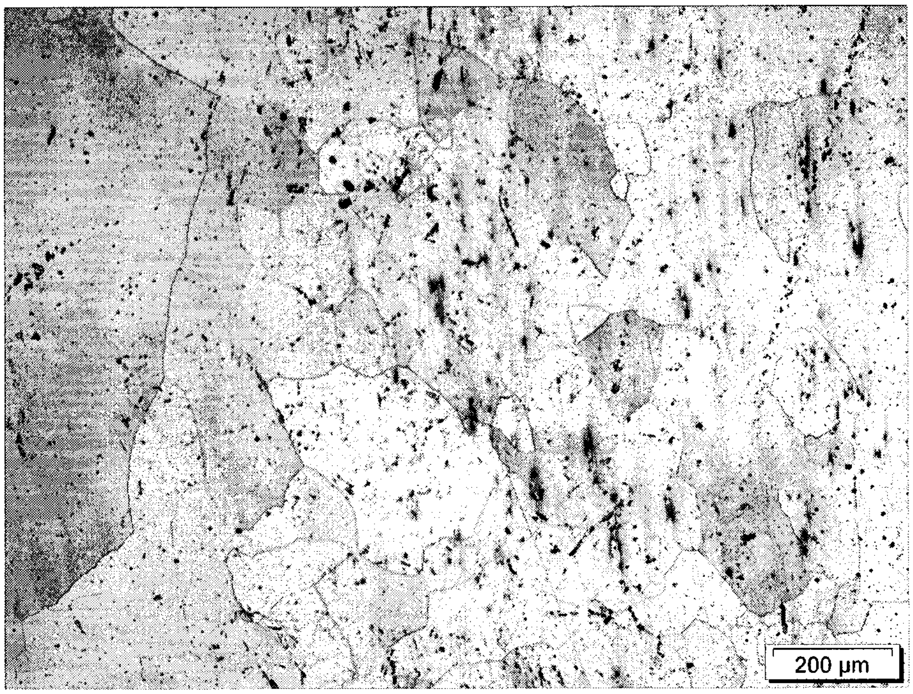

Figure 63: Optical micrographs of specimen 1 (400-0.1-0.2) annealed for 600s (as-worked, Fig 35).

a

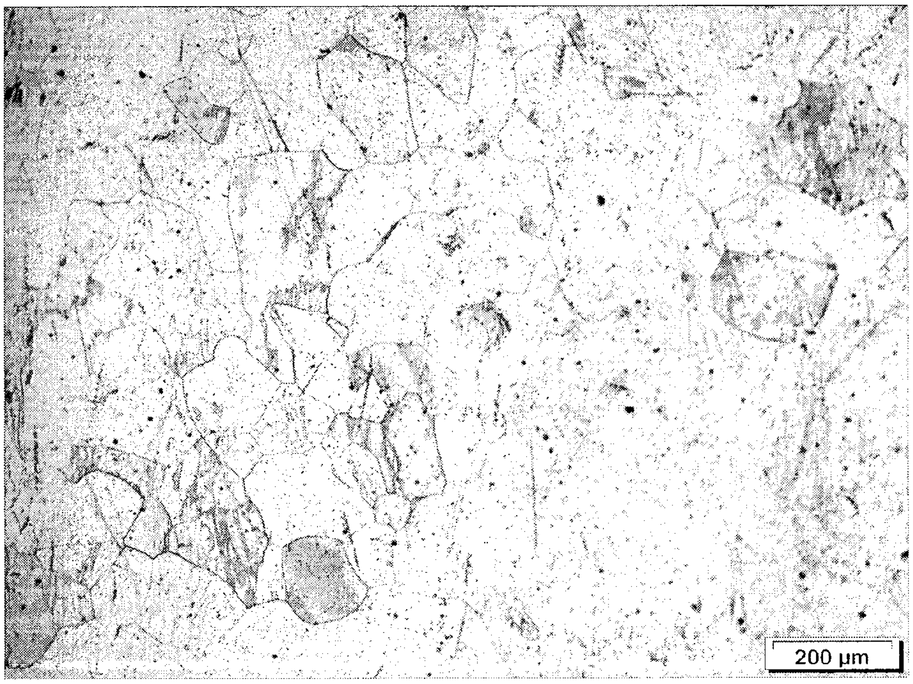

b

Figure 64: Optical micrographs of specimen 2 (400-0.1-0.5) annealed for 300s a) lower magnification b) higher magnification (as-worked, Fig 36).

Figure 65: Optical micrographs of specimen 2 (400-0.1-0.5) annealed for 500s (as-worked, Fig 36).

When specimen 5 and 6 were annealed for 125s (Fig 66, 68). Specimen 5 reveals grains of medium size, some of them are elongated with serrated boundaries. Near some surface grooves caused by increased local strain, there are fairly fine recrystallized grains. In specimen 6, evidence of strong GB serrations which could indicate early stages of nucleation. Evidence of elongated grains with deformation bands and equiaxed grains is seen near the edges. Hence at 125s, partial SRX is detected for specimens 5 and 6. Further annealing of specimens 5 and 6 to 450s exhibits completely recrystallized grains near the surfaces (Fig 67,69). In specimen 5, there was no presence of deformation bands which indicated that specimen had fully recrystallized. In specimen 6, there was evidence of recrystallized grains near the surfaces. At the centre, new grains were seen. Full SRX was seen in both specimens.

Specimens 3 and 4 which underwent backward path strain tests are annealed for 250s (Fig 70, 72). Microscopic observations revealed the presence of strain markings with fine medium sized grains. In the surfaces, some large grains were surrounded by fine grains (Fig 70, 72). It was estimated that there was only partial SRX at 250s. Further annealed to 450s, specimen 3 reveals full SRX near the surface; there several large grains being consumed by other grains growing into them (Fig 71). At the surface, there were large grains which may be due to initial larger grain size. At the centre, strong evidence of fine grains were seen. In specimen 4, there are some large grains in centre (Fig 73). There are very elongated grains into which other grains are growing surrounded by fine recrystallized grains. In the centre there is evidence of complete SRX.

A plot shows stages of SRX with the corresponding annealing times for forward strained specimens 1,2,5 and 6 and backward strained specimens 3 and 4 (Fig 74). Various stages of SRX are indicated by symbols. The times for SRX observed and SRX complete are noted down.

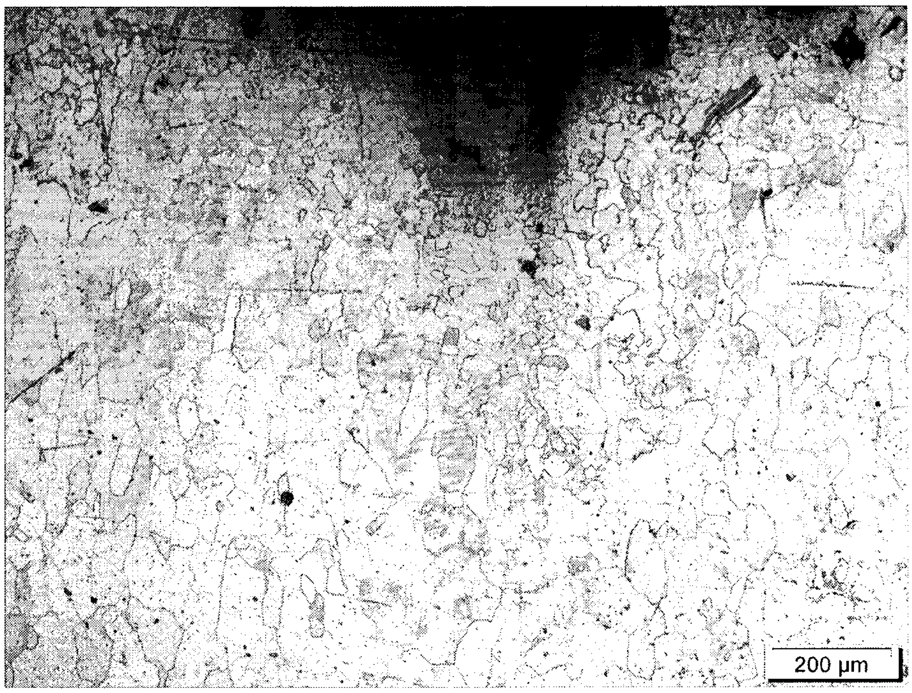

Figure 66: Optical micrograph of specimen 5 (400-0.1-0.5-400-0.1-1) annealed for 125s (as-worked, Fig 37).

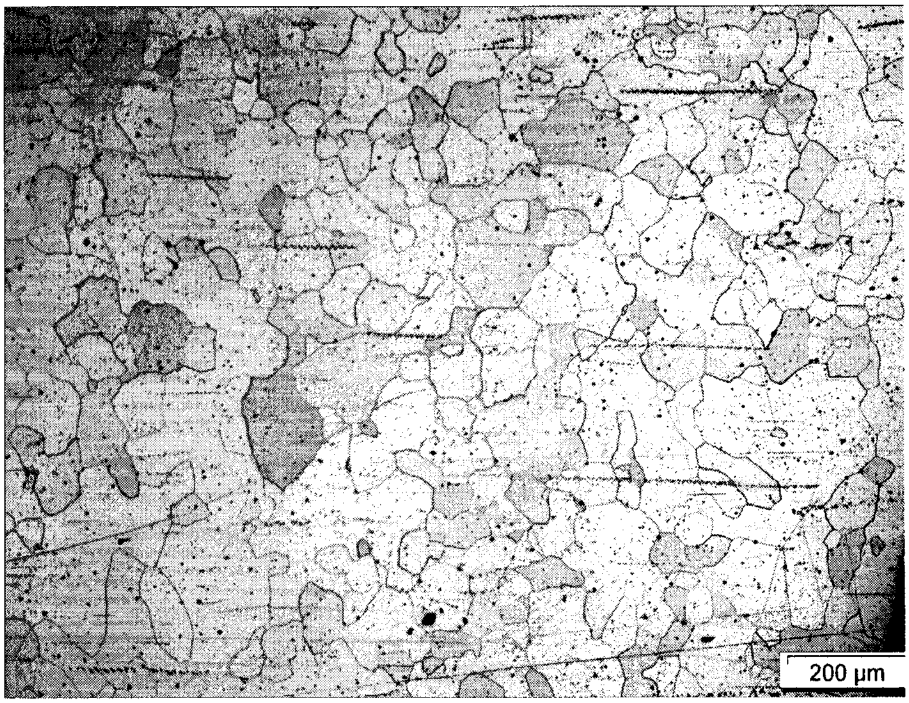

Figure 67:Optical micrograph of specimen 5 (400-0.1-0.5-400-0.1-1) annealed for 450s (as-worked, Fig 37).

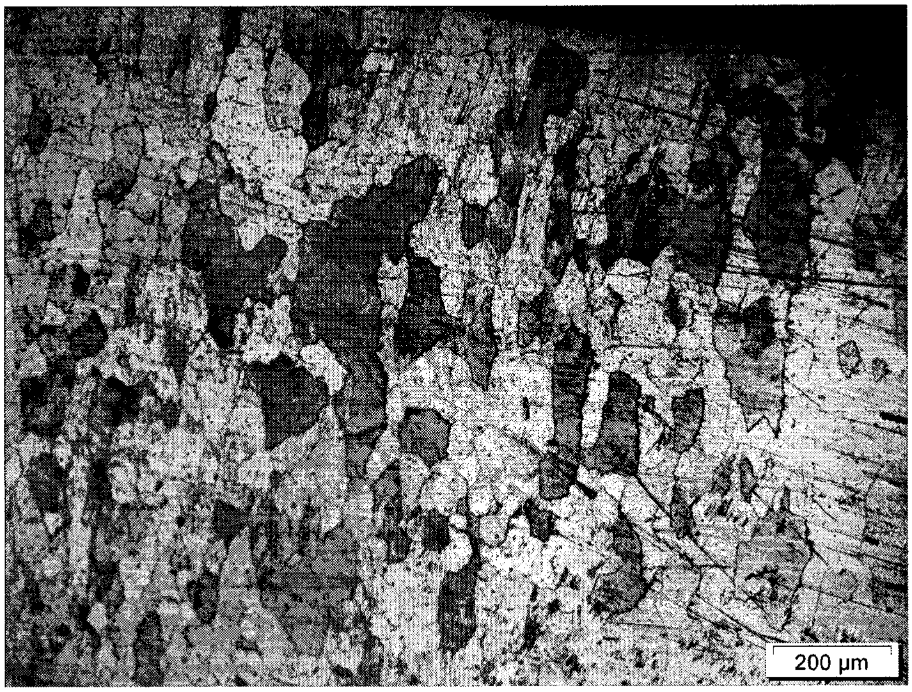

Figure 68: Optical micrograph of specimen 6 (400-0.1-0.5-400-0.1-5) annealed for 125s (as-worked, Fig 38).

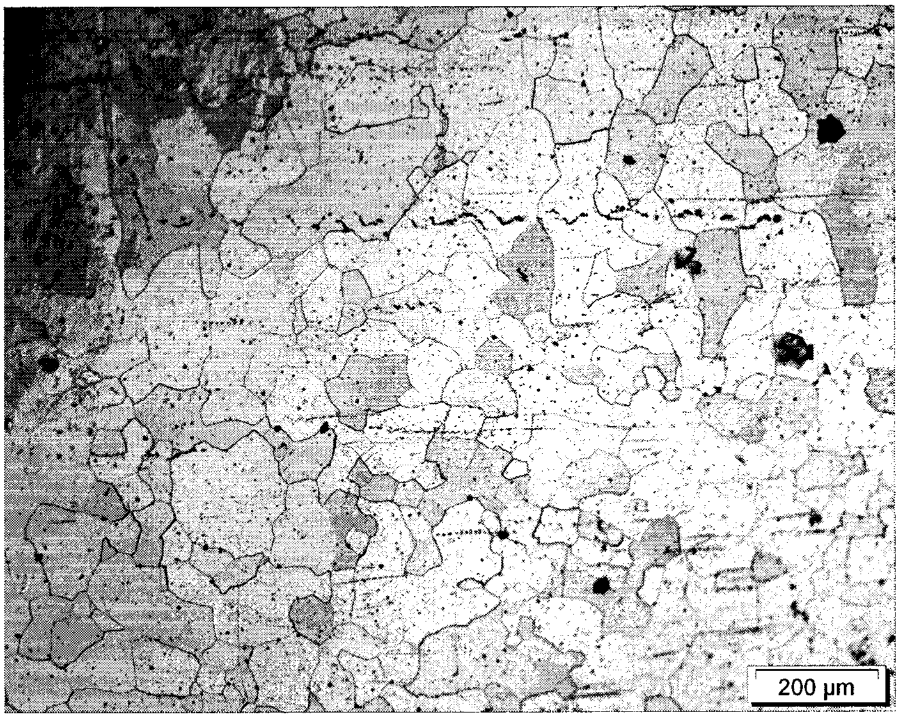

Figure 69: Optical micrograph of specimen 6 (400-0.1-0.5-400-0.1-5) annealed for 450s (as-worked, Fig 38)

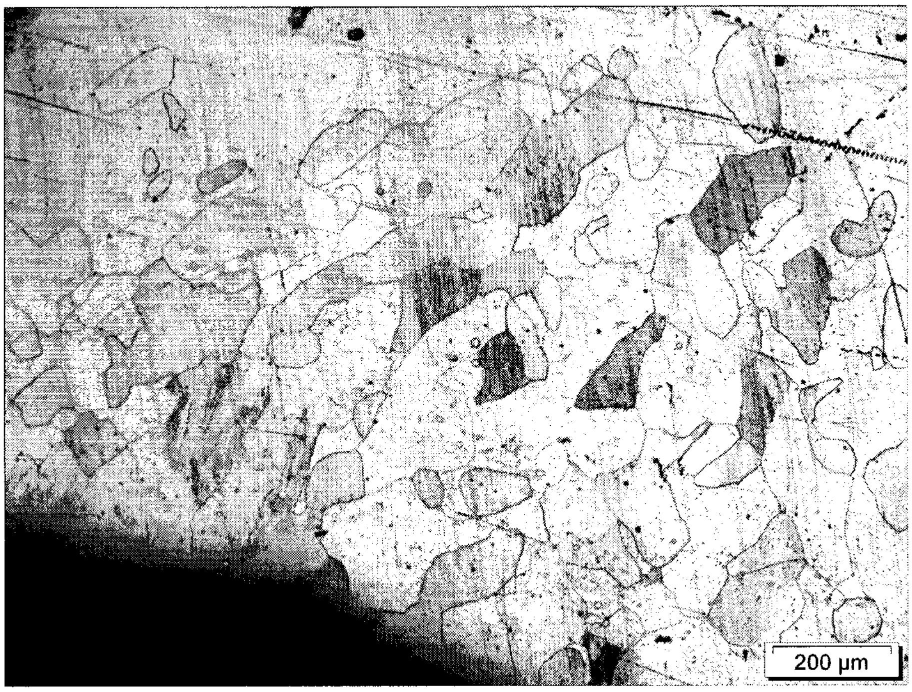

Figure 70: Optical micrograph of specimen 3 (400-0.1-0.5-400-0.1-0.2) annealed for 250s (as-worked, Fig 41).

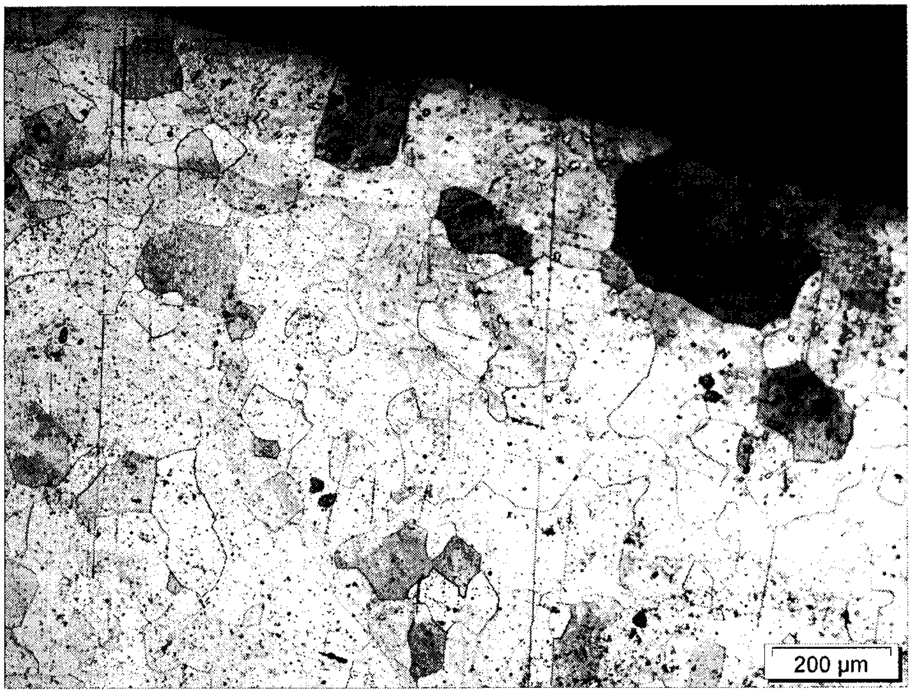

Figure 71: Optical micrograph of specimen 3 (400-0.1-0.5-400-0.1-0.2) annealed for 450s (as-worked, Fig 41).

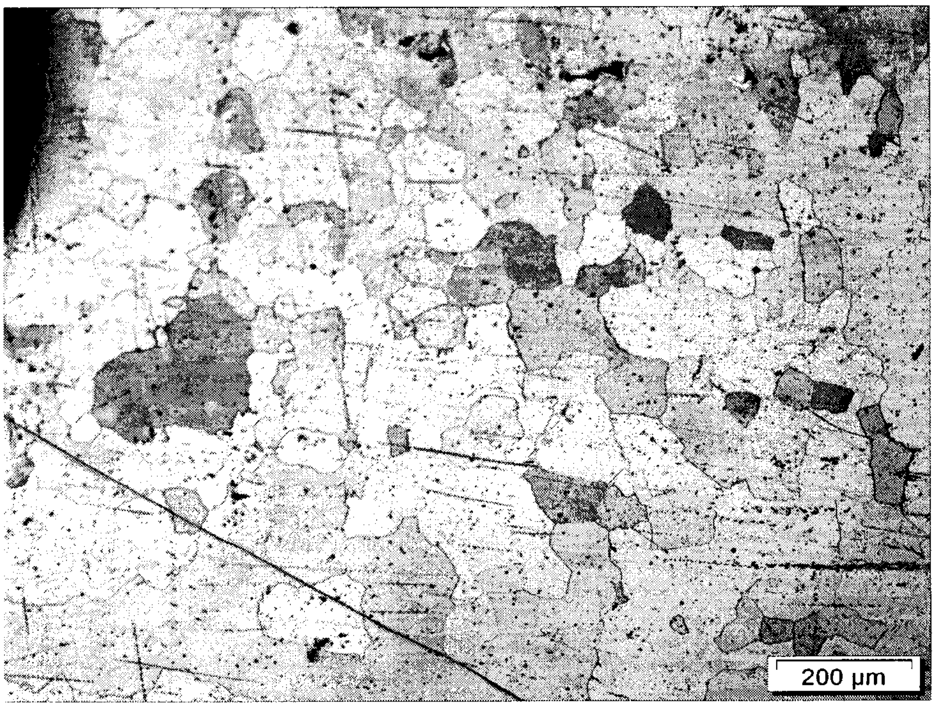

Figure 72: Optical micrograph of specimen 4 (400-0.1-0.5-400-0.1-0) annealed for 250s (as-worked, Fig 42).

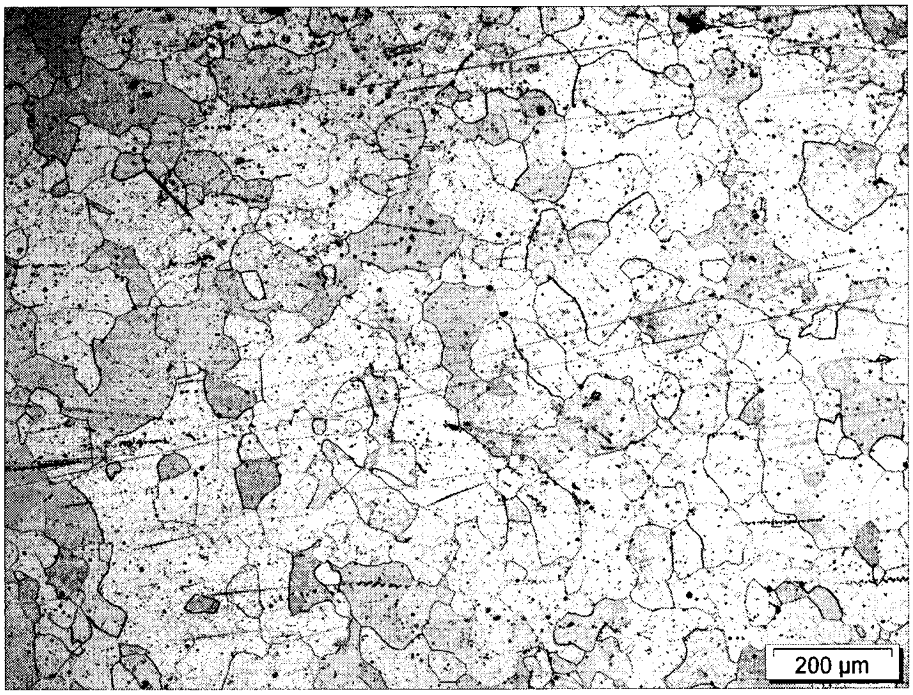

Figure 73: Optical micrographs of specimen 4 (400-0.1-0.5-400-0.1-0) annealed for 450s (as-worked, Fig 42).

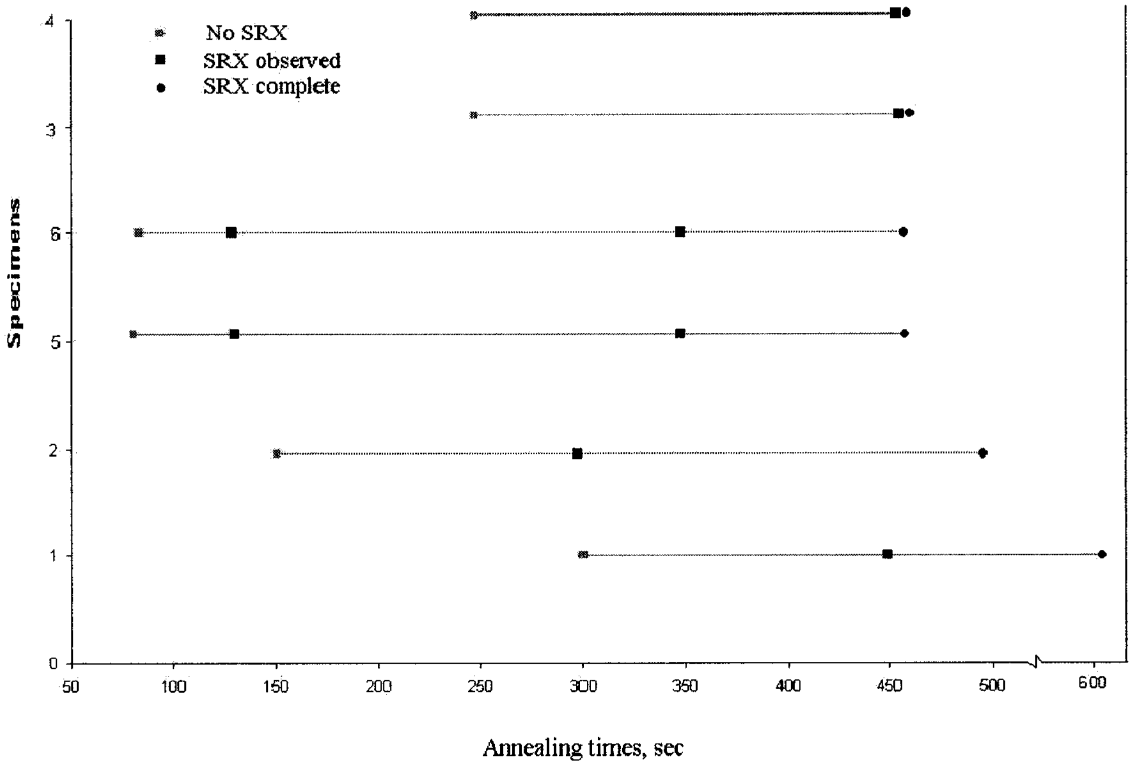

Figure 74: Plot showing annealing times with indication of degree of SRX (Specimens 1, 2, 5 and 6 were strained in forward direction to 0.2, 0.5,1 and 5 respectively. Specimens 3 and 4 were strained backwards from 0.5 to 0.2 and 0).

CHAPTER FIVE

DISCUSSION

The average measured flow stresses under a given test condition are in unison for all parts of the strain paths. These values are reasonably close to calculated flow stress values also (Tables 3,4). By observing common ground between these flow curves, one can conclude that DRV is the principal mechanism operating and it varies in relation to Z values. In decreasing order of logZ values, the flow stress reduces due to larger subgrain size and lower dislocation density. There is little or no Bauschinger effect at these high T conditions. Slight differences in flow stress values are noticed which may be due to different grain sizes.

When change in forward path included a decrease in $\dot{\varepsilon}$, there is no noticeable transient in change of the flow stress. However upon stress reversal with reduction in $\dot{\varepsilon}$, the initial flow stress is below the steady state by 2MPa (Table 2). In multistage processing, the lower flow stresses can facilitate easier processing and lower power usage in successive steps. The occurrence of DRV was confirmed in all as-worked specimens by optical microscopy, POM and OIM results.

In specimens deformed to 0.2 and 0.5, presence of large grains made it easier to see the deformation bands and established that some specimens had a variety of grain sizes (Fig 35, 36 and Fig 54). In specimens hot worked to strains of 1 and 5, features such as presence of deformation bands and elongated grains were confirmed in optical microscopy and POM (Fig 37, 38 and Fig 55). In reverse path specimens, grains returned towards being equiaxed and appeared somewhat finer possibly due to deformation bands (Fig 41, 42 and Fig 56).

POM macrographs revealed little visible grain alignment in the specimen hot worked to 0.2 (Fig 52). With further strain to 0.5 and 1, there was increased alignment of fine grains at 30° and 60° to the torsion axis (Fig 52). In specimens strained backwards from 0.5 to 0.2 and 0, the alignment of fine grains decreased from about 30° to 15° and 5° (Fig 53). There were some differences in grain sizes. This alignment of the grains is good evidence that there is no dynamic recrystallization in conjunction with the absence of peaks in the flow curves.

Under OIM in forward path specimen 2D deformed to 0.2, equiaxed subgrains of LAB are established along with some deformation bands (Fig 57). In specimens 5D and 6D, deformation bands of MAB are clearly emphasized as subgrains of LAB are maintained, as elongated grains start to break up due to intense rotation of deformation bands (Fig 58, 59). In specimens 3D and 4D, in the forward direction equiaxed subgrains with LAB are observed inside elongating grains. In the reverse direction, subgrains remain equiaxed and constant in size whereas the grains change from elongated back to equiaxed (Fig 60, 61). As many subgrains touch GB, parts of their boundaries are counted as HAB by OIM. Hence fraction of HAB rises with strain with respect to LAB.

OIM determines orientation of each cell region. It defines a small segment of boundary between each cell and creates a network of cellular boundaries and outlines them as LAB (1-5°), MAB (5-15°) and HAB (>15°) (Table 5). During the forward path, the grains and deformation bands are elongating so that MAB and HAB are increasing in length. During steady state straining either forward or backward path, the subgrains remain equiaxed and constant in size. More subgrains come in contact with the lengthened MAB and HAB so the fraction of LAB decreases as ε rises and increases as ε decreases. In comparison, the fraction of MAB and HAB rise in forward straining and decrease in reverse straining. The MAB are not eliminated by strain in the backward straining so the grains appear somewhat finer (Table 5).

The study of SRX developed several problems; the first occurrence of SRX could not be detected because the etchant did not clearly expose subgrains in the hot deformed grains. The etchant was selected to avoid perchloric acid as it is dangerously explosive and contaminates the hood system. Polarized light microscopy was not used because the microscope system with the digital recording camera did not have polarized equipment. Traditional photography on the optical microscope in EV 13.144 and use of digital camera system without polarizer lens in H0074 has many drawbacks for reproduction. As 400°C, $0.1s^{-1}$ was selected to give large subgrains to improve measurement in OIM, the strain energy is rather low. When annealed at 400°C, there is not high driving force so SRX is very sluggish and SRX grains are not fine.

Specimens 5, 6, 3 and 4 which underwent two stage testing either in the forward or backward path indicated same strain energy as the final stresses were almost the same (Table 2). In specimens 5 and 6 which were strained to higher strains of 1 and 5, shorter times for SRX was expected since grains were more elongated with larger GB area for nucleation. In reverse path specimens 3 and 4 (to 0.2 and 0), less nucleation was expected as grains were more equiaxed and less elongated than in the higher forward strain.

However much increased times for SRX in reverse path have been reported in the literature [64, 65]. Under similar conditions of T and $\dot{\varepsilon}$ in reverse path, Al-5Mg [65] showed reduced nucleation because of reduced local strain energy at SGB. In Al-2Mg [64], there was fall in misorientation and dislocation density during the backward path when compared to forward path. As high local density of dislocations is partly responsible for enhanced nucleation and hence shorter times for SRX. It can be inferred that for those specimens which underwent two stage testing under reverse straining had longer times for SRX. Researchers [64] have concluded that during reverse loading micro-bands are disturbed resulting in establishment of larger cells with lower misorientation. As micro-bands have high misorientation, they play a key role in SRX.

Moreover, they concluded that SRX was also slowed because the equiaxed grains have lower GB area, as nucleation occurs when there is local high misorientation ($>15^{o}$) [65]. There was faster SRX in forward path specimens as local misorientations increased in the forward straining. In the case of reverse path specimens local misorientation dropped whereas the mean misorientation remained the same. In reverse path specimens there was little difference in strain energies because the flow stresses are same in forward and backward path. So it was expected that SRX times would be longer. There was difficulty in establishing clear times for SRX; there was no conclusive evidence to indicate SRX was slower in specimens 3 and 4. In the as-worked specimens 3 and 4 some grains with serrated grain boundaries were observed; these could have acted as recrystallization sites in promoting SRX. The determinations of SRX progress were not clear; this can be partly attributed to variations in initial grain sizes.

CHAPTER SIX

CONCLUSION

- The flow curves of the initial tests at 400°C, 0.1s^{-1} to strains of 0.5, almost all the specimens strain hardened to a plateau near 27.5MPa. At higher strains of 1 or 5, the average measured flow stresses remained the same; similarly under reverse path, the flow stress was also about 27.5MPa. When compared with flow stresses calculated from the literature, the difference is quite small. There was neglible Bauschinger effect.
- At 400°C, 0.001s^{-1} in forward or reverse direction, the average measured plateau flow stresses were established at 22.5MPa at strain of 0.5 in all these specimens. When compared with the calculated flow stress, the average measured flow stress for this condition falls short by 0.32MPa. A slight Bauschinger effect is indicated by a flow stress decrease on reversal before it rises to the steady state value.
- Under test conditions of 500°C, 0.1s^{-1} in forward or reverse direction, the average measured flow stress was 25MPa; thus more than the calculated flow stress by 3.36MPa. No noticeable transient change in flow stress in the reverse path.
- The flow curves characteristics and following metallographic results confirm the occurrence of DRV as follows
- In the forward path with increasing forward strain
    - grains elongate and align at higher angle to axis (ruling out DRX)
    - deformation bands form inside grains at low ε and then rotate and elongate

  - grain boundaries become serrated
  - from OIM, the subgrains remain equiaxed and constant in size
  - as more subgrains come in contact with elongating grain boundaries the fraction of LAB decreases as HAB increases
- During the reverse path with backward strain
  - grains return towards being equiaxed and alignment to lower angles
  - deformation bands are retained, becoming hard to distinguish from GB
  - grain boundaries remain serrated
  - from OIM, subgrains remain equiaxed and constant in size. The fraction of LAB increases
- From OIM, it was inferred
  - In the forward path, as number of subgrains touching elongating GB increases, the fraction of LAB decreases with respect to HAB
  - During reverse path, number of subgrains touching GB decreases, the fraction of LAB increases with respect to HAB
- Observation of SRX was difficult due to low strain energy and the unsuitable etchant
  - In forward path specimens, due to increased strain energy and lengthened GB, specimens had slightly faster SRX times
  - As strain energy did not decrease in reverse path, SRX became slightly slower as grains return to being equiaxed

REFERENCES

[1] H.J.McQueen, Mett. Trans. A, 1977, Vol 8A, pp. 807-824

[2] K.Conrod, The Hot working characteristics of Al-0.65%Fe and Al-0.5%Fe-0.5%Co conductor alloys. Thesis in the Dept of Mechanical Eng, Concordia University, Montreal, Aug 2000

[3] R.W.Evans and G.R.Dunstan, J. Inst. Metals, 1971, vol 99, pp. 4-14 (cited in [1])

[4] H.J.McQueen and J.J.Jonas, ed R.J.Arsenault, Academic Press, vol 6, NY, 1975, pp.393-493 (Cited in [2])

[5] H.J.McQueen and K. Conrod, In Microstructural control in Al alloys. E.D.Chia and H.J.McQueen, TMS –AIME, Warangal, Pa; 1986, pp.197-219 (Cited in [2])

[6] H.J.McQueen and J.E.Hockett: Met.Trans.A,1970, vol.1,pp 2997-3004 (Cited in [1])

[7] George E. Dieter, Mechanical Metallurgy, 1985, vol 3 ,pp.220 – 232

[8] R.J.McElroy and Z.C.Szkopiak: Int.Met.Rev., 1972, vol 17, pp. 175-202 (Cited in [1]

[9] A.K.Mukherjee: Ibid, 1971, pp.164-225 (Cited in [1])

[10] H.J. McQueen, W.A. Wong and J.J. Jonas: Can J Phys., 1967, vol 45, pp. 1225-35 (Cited in [1])

[11] O.Kosik, D.J.Abson and J.J.Jonas: J.Iron Steel Inst, 1971, vol 209, pp.624-671 (Cited in [1])

[12] D.J Abson and J.J. Jonas: Metal Sci. J., 1970, vol 4, pp.24-18 (cited in [1])

[13] J.E.Hockett and H.J.McQueen: Proc. 2nd Int Conf Strength of Metals and Alloys, ASM, Metals Park, Ohio, 1970 (Cited in [1])

[14] C.J.Ball:Phil.Mag. 1957, vol 2, pp.1011-1017 (cited in [1])

[15] J.E.Pratt:J.Mater., 1966, vol1, pp.77-88 (cited in [1])

[16] H.J.McQueen, Metalurgia I Odlewnicto (Metallurgy and Foundry) Tom5 Zeszyt 3,1979 , pp 421-450 (Cited in [2])

[17] D.J.Lloyd and D.Kenny, Acta Met., 1980, vol 28,, pp 639-649

[18] H.J.McQueen and H.Mecking, in " Creep Fracture of engineering materials and structures", ed B. Wilshire and D.R.J Owen, Pineridge press, Swansea, U K , 1984, pp 169-184 (Cited in [2])

[19] W.D.Nix and B.Illscher, in "Strength of Metals and Alloys (ICSMA 5)", ed P.Haasen et al, Pergamon Press, oxford, Vol 3, 1979, pp. 1503-1530 (Cited in [2])

[20] M.E.Kassner, N.Q.Nguyen, G.A.Henshall and H.J.McQueen, Materials science and Eng.Vol A 132,1991, pp.107-105

[21] J.R.Cotner and W.J.McG.Tegart:J.Inst.Met, 1969, pp.73 (Cited in [20])

[22] A.C.F.Cocks and M.F.Ashby, Prog.Mater.Sci, 1982,pp. 189 (Cited in [20])

[23] H.J.McQueen and W.Blum, Part II: Hot Ductility and Extrusion Aluminum, 80 2004, pp.1150+

[24] H.J.McQueen and M.E.Kassner, Superplasticity in Aerospace II, T R McNelley ed (Met Soc AIME, Warrandale PA 1990 (in press) (Cited in [23])

[25] V.A.Likachev.M.M.Myshlyaev and O.N.Senkov, Institute if solid state physics. Chernogolovok, (1981); English trans. Lawrence Livermore National laboratory. UCIR-1681, (1987) (Cited in [23])

[26] G.A.Henshall, M.E.Kassner and H.J.McQueen, Mettalurgical Transactions A, Volume 23A, March 1992, pp.881-889 (Cited in [23])

[27] M.S.Mostafa and F.A.Mohammed: Metall Trans A. (1986), pp.365-366 (Cited in [23])

[28] Ivanchev.L and Chadarova .D; Proc.Intl.Symp. Plasticity and Resistance to Metal Deformation, S.Blecic et al., eds., Fac.Metalurgy, Titograd (1986), pp.348-361 (Cited in [23])

[29] F.A.Mohammed: Scripta Metall, 12: (1978), pp.99-102 (Cited in [23])

[30] H.J.McQueen, J.Sankar and S.Fulop, ICM3. Vol 2, England, Aug 1979, pp.675-683

[31] Van Vlack, Elements of Materials Science and Engineering. Fourth edition.Addison Wesley Publishing Company, USA, 1985, pp.206-216

[32] William J.Smith, Principles of Material Science and Engineering. , Third Edition, McGraw-Hill Inc, New York, 2004, pp.227-246

[33] H.J. McQueen and E.Evangelista, Czechslovak Journal of Physics, Volume B 38, 1988, pp.359-372

[34] H.Chandra Holm, J.D.Embury and U.F.Kocks, Strength of Metals and Alloys. ICSMA 5, P.Haasen et al eds (Pergamon Press Oxford), 1987, pp. 141 (Cited in [33])

[35] W.Pfeiler, M.Zehetbauer and J.Schrank, Scripta Met. 19 (1985), pp.505 (Cited in [33])

[36] H.Hero and C.J.Simenson, Scand J Metal 1 (1972), pp.115 (Cited in [33])

[37] A.Korbel, M.Richert and J.Richert, Deformation of Polycrystals: Mechanisms and Microstructures, N Hansen et al eds. (Riso Natl lab Roskilde), 1981, pp. 45 (Cited in [33])

[38] Gil-Seviano J, Van Houte P,Aeronoudt E: Prog.Mater.Sci.25 (1980), pp. 69 (Cited in [33])

[39] Gil-Seviano J, Aeronoudt E: Prog.Mater.Sci.86 (1987),pp. 35 (Cited in [33])

[40] Richard W Hertzberg, Deformation and Fracture Mechanics of Engineering Materials. John Wiley and Sons Inc, May 1996, , pp.124-125

[41] R.D.Doherty, D.A.Hughes, F.J.Humphreys, J J Jonas, D Juul Jensen, M E Kassner (editor), W E King, T R McNelley, H J McQueen, A D Rollett, Mat Sci Eng, 238 (1998),pp. 219-274 (Cited in [33])

[42] Z.D.Jastrzebski, "The Nature and Properties of Engineering Materials", Wiley 1976, pp. 2286 (Cited in [32])

[43] Aluminum., Vol 1 . American Soceity for Metals, 1967, pp. 98 (Cited in [31])

[44] H.J.McQueen, Metal Forming: Industrial, Mechanical, computational and Microstructural, 1987, pp. 2-23

[45] C.M.Sellars, A.M.Irisarri and E.S.Puchi in: E.H.Chia and H.J.McQueen (eds).Microstructural control of Al alloys, Met Soc. AIME, Warrandale, PA, 1990,pp.179-196 (Cited in [44])

[46] R.A.Petkovic, M.J.Lution and J.J.Jonas, Can Metall.Q., 14 1975,pp. 137-145 (Cited in [44])

[47] K.Conrod and H.J.McQueen in E.A.Starke and T.H.Sanders, eds Aluminum alloys physical and mechanical properties, Eng Mat Advisory, Warley UK, vol 1, 1978,pp. 435-437 (Cited in [44])

[48] J.Sankar, D.Hawkins and H.J.McQueen, Mettall Tech., 6 1979,pp. 325-331 (Cited in [44])

[49] N.D.Ryan and H.J.McQueen. Materials Forum, 14 1990,pp. 283-295 (Cited in [44])

[50] N.D.Ryan and H.J.McQueen. Mat Sci Tech, 7 1991,pp. 818-826 (Cited in [44])

[51] H.J McQueen and N.Ryum, Scandinavian Journal of Metallurgy 14 (1985), pp. 183-194

[52] H.J McQueen., Can.Met.Q.21 1982,pp 445-460 (Cited in [51])

[53] J.R Cotner and W.J.Tegart, W J McGr., Trans AIMe 191 1951, pp.643-652 (Cited in [51])

[54] V.A Vandermer and P.Gordon, Recrystallisation in Aluminum. In Recovery and Recrystallisation of Metals (ed. L Himmel) pp. 211-240, Inter Science Pubishers John Wilet, New York 1963 (Cited in [51])

[55] H. J.McQueen, Hot deformation of Aluminum Alloys, T.G Langdon, H.D Merchant (eds), TMS-AIME, Warrandale PA 1990, pp.655-660 (Cited in [51])

[56] F. J.Humphreys, M. Hatherley, Recrystallization and Annealing Phenomenon. Pergamon Press, Oxford, 1995 (Cited in [51])

[57] H. J.McQueen, Mat.Sci.Eng. A 101, 1987, pp.149-160 (Cited in [51])

[58] F. R.Castro Fernandez, C M Sellars, Mat.Sci.tech, 4 1988,pp. 621-627 (Cited in [44])

[58] E. C. W Perryman, Trans.AIME 203 1955,pp. 369-378 (Cited in [44])

[59] P. H.Thorton, R W Cahn, J.Inst.Met. 89 (1960) , pp.455 (Cited in [44])

[60] J. H.Auld, R.I.Garrod, T.R.Thomson, Acta Met/5 1957, pp. 741 (Cited in [44])

[61] S. Fulop, K.C. Cadien, M.J.Luton and H. J.McQueen. Journal of Testing and Evaluation , Vol 5, No 6, 1977, pp.419-426

[62] G.Avramovic-Cingara and H.J.McQueen, Materials Science Forum, in press

[63] G.Cingara and H.J.McQueen, Materials Science Forum (Cited in [62])

[64] C.M.Sellars, University of Sheffield, pp.21-23, 2006

[65] H.J.McQueen, E.Evangelista and H.Farah, Hot deformation of aluminum alloys III, 2003, pp. 71-86